NOAA Technical Memorandum ERL NSSL-95
(Second Printing)

SINGLE DOPPLER VELOCITY SIGNATURES: AN ATLAS OF PATTERNS IN CLEAR AIR/WIDESPREAD PRECIPITATION AND CONVECTIVE STORMS

Vincent T. Wood
Rodger A. Brown

National Severe Storms Laboratory
Norman, Oklahoma
November 1983

UNITED STATES
DEPARTMENT OF COMMERCE

Malcolm Baldrige,
Secretary

NATIONAL OCEANIC AND
ATMOSPHERIC ADMINISTRATION

John V. Byrne,
Administrator

Environmental Research
Laboratories

Vernon E. Derr
Director

TABLE OF CONTENTS

SINGLE DOPPLER VELOCITY SIGNATURES: AN ATLAS OF PATTERNS IN CLEAR AIR/WIDESPREAD PRECIPITATION AND CONVECTIVE STORMS

Vincent T. Wood and Rodger A. Brown

Abstract

A variety of single Doppler velocity patterns that simulate those observed in the atmosphere are presented. Measurements in optically clear air/widespread precipitation are simulated using horizontally uniform wind fields that change with height. Measurements of horizontal flow fields within thunderstorms are simulated using a combination of simple rotation, divergence/convergence and uniform flow models. Simulations are compared with actual Doppler velocity measurements to test the veracity of the simulations.

1. Introduction

Measurements in optically clear air and widespread precipitation show that environmental wind profiles and areas of low-level mesoscale convergence can be determined using a single Doppler radar (e.g., Lhermitte and Atlas, 1961; Rabin and Doviak, 1982). Data collected on the individual thunderstorm scale since the late 1960's indicate the severe storm warning potential of Doppler radar (e.g., Donaldson, 1967; Burgess, 1976; Lemon et al., 1977).

During the mid-1970's, government agencies with severe storm warning concerns--National Weather Service (NWS), Air Force's Air Weather Service, Federal Aviation Administration--became interested in the capabilities of Doppler radar (e.g., Johannessen and Kessler, 1976). So a Joint Doppler Operational Project (JDOP) was established during 1977-1979 to test Doppler radar in an operational setting. The results (Staff, 1979) were so encouraging that the agencies decided to replace their aging weather radars with the jointly procured Next Generation Weather Radar--NEXRAD--that includes Doppler capability (e.g., Bonewitz, 1981; Ray and Colbert, 1982).

As Doppler radars become operational,[1] there will be increased interest in the interpretation of single Doppler velocity patterns. Patterns that convey knowl-

[1] Since April 1982, the Montgomery, AL, NWS office has had the loan of a Doppler processor to use with its 5-cm wavelength WSR-74C weather radar. During the summer of 1983, a Doppler processor--purchased by concerned citizens in the Chicago area--became operational on NWS's 10-cm WSR-74S radar in Marseilles, IL. The first NEXRAD 10-cm radars are expected to go into operation in 1988.

edge are typically called "signatures." This atlas will help people recognize and interpret single Doppler velocity signatures that are encountered in a variety of meteorological situations.

In addition to measuring the reflectivity returned from radar echoes[2] as a conventional weather radar, Doppler radar also measured the component of motion in the radar viewing direction. The radar completely senses flow directly toward (defined as negative Doppler velocities) or away from the radar (positive Doppler velocities). However, if flow is perpendicular to the viewing direction, there is no component of motion relative to the radar; the measured Doppler velocity value is zero.

Single Doppler velocity patterns (signatures) found in this atlas are portrayed with contour lines of equal Doppler velocity values. On a color display, the contour lines would represent the boundaries between adjacent colors (velocity intervals).

---

[2] Within optically clear air, radar echoes are due to insects and refractivity variations (caused by temperature and moisture variations). Within clouds, echoes are due to precipitation particles (drizzle, rain, ice particles, hail).

2. IDEALIZED ENVIRONMENTAL WIND FIELDS

2.1 Explanation of mapping the Doppler wind field

Although a Doppler radar observes only the component of the wind in a radial direction from the radar, a wide variety of weather features of great importance to weather forecasters can be easily identified. This section describes techniques of single Doppler pattern recognition for winds that are horizontally uniform but vary with height. The displays will give the meteorologists self-confidence in their real-time interpretation of Doppler velocity data.

We consider a Cartesian coordinate system in which x and y are horizontal distances from a Doppler radar site (Fig. 2.1). As an antenna is rotated about a vertical axis z at a constant elevation angle ϕ, detailed displays are obtained of the Doppler component of the target velocity V_d as a function of azimuth and slant range r_s (or height h). Procedures for computing vertical profiles of horizontally homogeneous wind direction and speed follow.

A Doppler radar detects only the component of wind velocity along the radar beam. From geometry in Fig. 2.1a it is seen that, since $h=r_s \sin\phi$ and $H=R_s \sin\phi$,

$$\frac{r_s}{R_s} = \frac{h}{H} \quad , \tag{1}$$

where r_s is the slant range from the radar site, R_s the maximum slant range at the edge of the radar display, h the height above the radar's horizontal plane, and H the maximum height at the edge of the display. The wind components in the idealized environmental flow fields are used to compute Doppler components toward and away from the radar. At each grid point, the velocity component u is directed eastward and component v is directed northward so that the component of wind toward or away from the radar, denoted by V_d, is computed from the simple expression (e.g., Armijo, 1969)

$$V_d = u\left(\frac{x}{r_s}\right) + v\left(\frac{y}{r_s}\right) + w\left(\frac{z}{r_s}\right) \quad . \tag{2}$$

In the absence of convection, vertical air motions (w) are negligible relative to horizontal air flows, so Eq. (2) becomes

$$V_d = u\left(\frac{x}{r_s}\right) + v\left(\frac{y}{r_s}\right) \quad . \tag{3}$$

The general form of the wind components used to profile tropospheric wind flows is given by

$$\begin{aligned} u &= \text{spd}(h)\ \cos(270°-\text{dir}(h)) \\ v &= \text{spd}(h)\ \sin(270°-\text{dir}(h)) \end{aligned} \quad , \tag{4}$$

where spd(h) is the wind speed, dir(h) the wind direction, both functions of height, h.

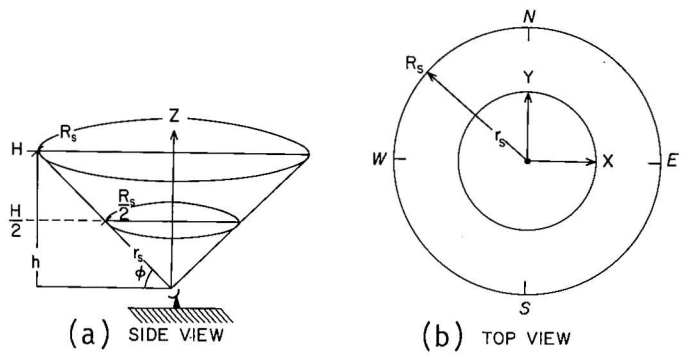

Fig. 2.1 Doppler radar viewing configuration.

2.2 Uniform flow at all heights

In this subsection, we consider three uniform flow fields (wind direction and speed remain constant with height) whose vertical profiles are described by

$$\begin{array}{lll} \text{(a)} & \text{spd}(h) = S & \text{(b)} \quad \text{spd}(h) = S \\ & \text{dir}(h) = 225^\circ & \quad\;\; \text{dir}(h) = 270^\circ \\ \text{(c)} & \text{spd}(h) = S & 0 \leq h \leq H \\ & \text{dir}(h) = 315^\circ & \end{array} \qquad (5)$$

where S is the unspecified constant wind speed. These data are illustrated in the left part of Figs. 2.2a,b,c. Vertical profiles of hypothetical wind direction and speed computed from Eqs. (4)-(5) are shown, respectively, in the upper and lower boxes in the middle part of these figures. Thus, we know, for instance, that the wind is blowing at a constant speed S from southwest (225°) at all altitude levels, as shown in Fig. 2.2a.

The right part of Fig. 2.2a represents the corresponding Doppler radar display where contours diverging from the radar (center dot) are isolines of V_d--called isodops. By the convention employed, negative radial velocity components (flow toward the radar) are indicated by thin short-dashed contours, while positive velocities (flow away from the radar) are shown by thin solid contours. Maximum and minimum speeds are indicated by thick solid and short-dashed contours, respectively. The thick long-dashed contour represents zero velocity where the radar beam is oriented perpendicular to the wind direction. The radar measures zero velocity component when it is pointed toward 135° and 315° azimuth. At these azimuths, the radar beam is oriented perpendicular to the wind direction at all altitudes and therefore at all slant ranges. As the radar rotates away from 135° and 315° the Doppler velocity increases (decreases) until it reaches a maximum value of the wind speed, S at 45° (minimum of -S at 225°). At these azimuths, the radar beam is oriented parallel to the wind direction and, therefore, measures a radial component equal in magnitude to the wind speed.

Analogous to Fig. 2.2a, Figs. 2.2b,c are constant wind direction and speed situations where the wind direction changes from 225° (Fig. 2.2a) to 270° (Fig. 2.2b) to 315° (Fig. 2.2c). Interpretation of the Doppler displays in Figs. 2.2b,c is similar to that of Fig. 2.2a, except that in each figure the pattern rotates clockwise by 45° for each step.

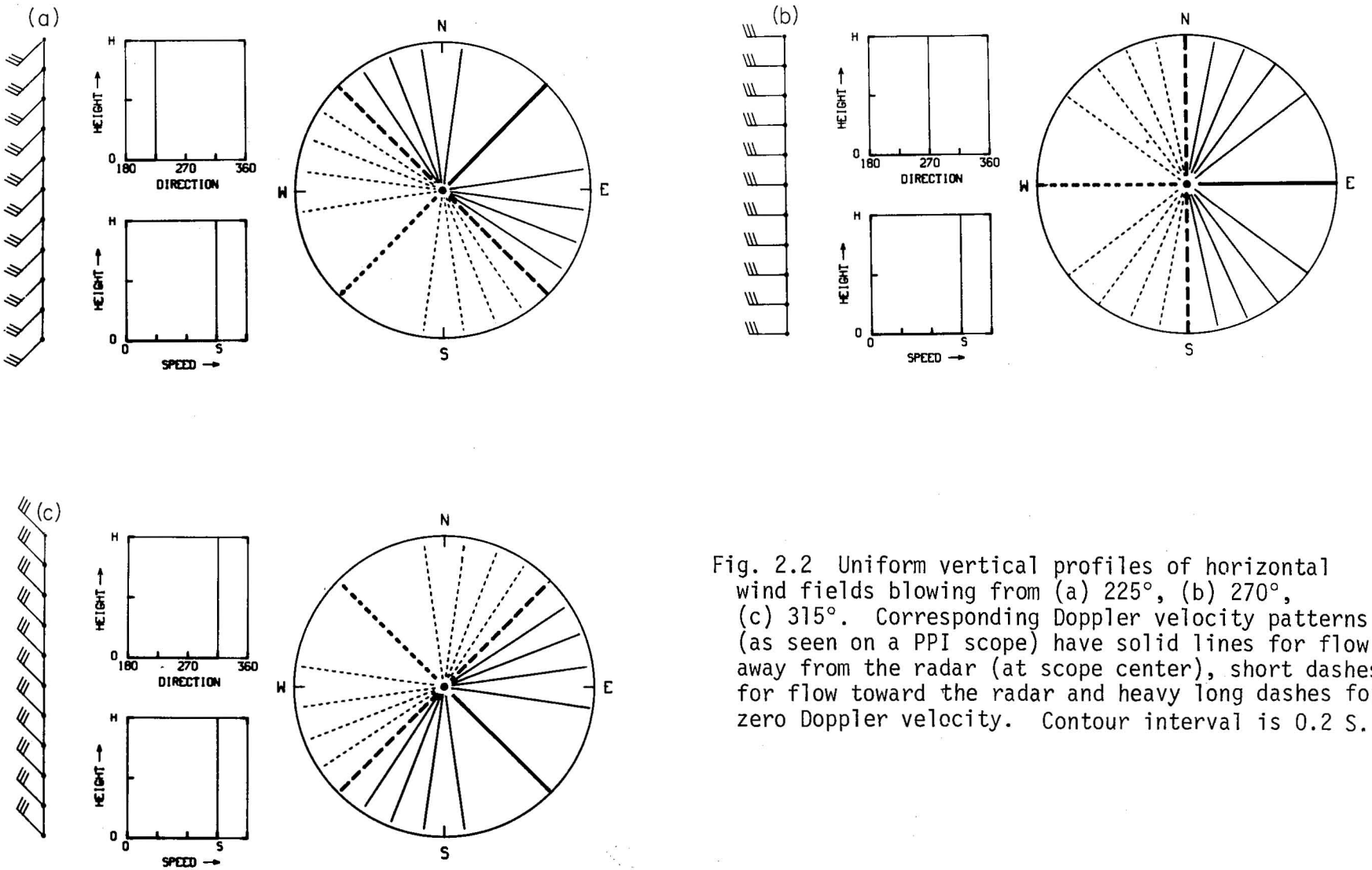

Fig. 2.2 Uniform vertical profiles of horizontal wind fields blowing from (a) 225°, (b) 270°, (c) 315°. Corresponding Doppler velocity patterns (as seen on a PPI scope) have solid lines for flow away from the radar (at scope center), short dashes for flow toward the radar and heavy long dashes for zero Doppler velocity. Contour interval is 0.2 S.

2.3 Uniform directional shear with constant wind speed

A uniform directional shear with constant wind speed (S) characterizes a wind structure in which the wind direction changes with height and the wind speed remains invariant. Four arbitrary vertical profiles for backing (cold air advection), uniform and veering (warm air advection) winds are given by

a) $spd(h) = S$
$dir(h) = 180°[1-0.25(\frac{h}{H})]$

b) $spd(h) = S$
$dir(h) = 180°$

$0 \leq h \leq H$ (6)

c) $spd(h) = S$
$dir(h) = 180°[1+0.25(\frac{h}{H})]$

d) $spd(h) = S$
$dir(h) = 180°[1+0.5(\frac{h}{H})]$

These profiles are correspondingly illustrated in the left partsof Figs. 2.3a-d. Figure 2.3a exhibits backing of the wind with height up to the maximum height H. Note that the zero velocity contour (thick long-dashed) bisects the radar display in the shape of a "backward S". The explanation for this behavior of wind direction is straightforward. The zero velocity contour represents the locus of points where the radar beam points normal to the wind direction. Since the direction of the backing wind changes with height (range), the zero velocity contour correspondingly changes with height. The wind speed remains constant with range (height) so the contour lines extend from the radar (center) to the maximum range. Therefore, the radar measurements reveal a southerly wind at the surface, backing with height until it becomes southeasterly at the edge of the radar display.

Figure 2.3b exhibits a constant wind direction and speed situation, which is similar to the situation in Fig. 2.2a when the pattern rotates clockwise by 45°. As already discussed in Sec. 2.2, radial straight lines indicate that winds neither back nor veer with height.

The presence of veering winds with height is illustrated in Fig. 2.3c. The radar display is analogous to that of Fig. 2.3a, except that the pattern is reversed so that the display is bisected by a letter "S" at all altitude levels. The zero velocity contour shows winds veering from south near the surface to southwest aloft.

The difference between the radial velocity component (V_d) distributions in Fig. 2.3c and Fig. 2.3d is that the radial velocity components exhibit greater curvature because of the more rapid changing of wind direction with height. It is obvious that greater curvature of the Doppler velocity contours implies an increased veering of the winds. We note that winds veer from the south near the ground to the west aloft by following the zero velocity contour that has the shape of an "S".

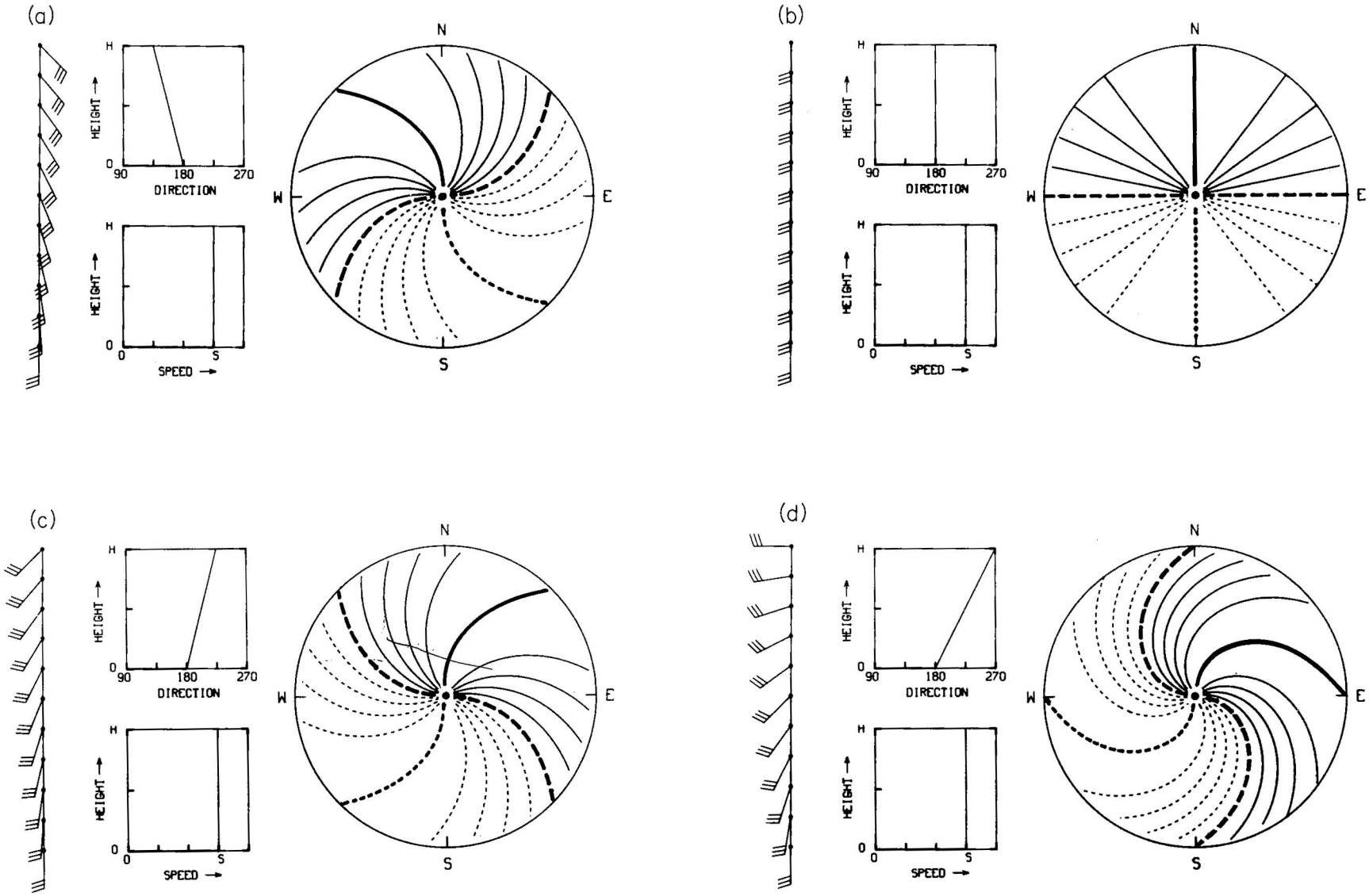

Fig. 2.3 Uniform direction shear with constant wind speed: (a) backing wind, (b) uniform wind, (c) veering wind, (d) stronger veering of wind. Doppler velocity contours (as seen on circular radar display) have solid lines for flow away from radar, short dashes for flow toward radar and heavy long dashes for zero Doppler velocity. Heavier solid and short dashed lines indicate locations of extreme Doppler velocity values within the display.

2.4 Uniform wind speed shear with constant wind direction

Figures 2.4 a-d illustrate wind regimes, where wind speed changes linearly with height while wind direction does not change. Note that a circle located at the bottom of vertical wind sounding in Fig. 2.4a denotes calm winds at the surface. Four arbitrary vertical profiles describing the degree to which the wind speed changes linearly with height are given, in these corresponding figures, by

a) $spd(h) = S(\frac{h}{H})$
$dir(h) = 270°$

b) $spd(h) = S(0.33 + 0.67\frac{h}{H})$
$dir(h) = 270°$

$$0 \leq h \leq H \qquad (7)$$

c) $spd(h) = S(0.67 + 0.33\frac{h}{H})$
$dir(h) = 270°$

d) $spd(h) = S$
$dir(h) = 270°$.

It is of interest to note that Fig. 2.4a shows westerly winds increasing linearly with height whereby solid and short dashed thin contours are oriented parallel with the zero velocity contour. The extreme horizontal wind speeds are indicated by the two crossmarks on the edge of the radar display, one upwind and one downwind; these extrema occur at one height rather than at all heights as has been the case in the previous figures.

Figure 2.4b exhibits a westerly wind shear which is less than that in Fig. 2.4a; wind speed at the ground is one third of the maximum value S (instead of being zero). The thin solid and short-dashed contours tend to converge at the center of the radar display and are no longer parallel to the zero velocity contour. The zero velocity contour remains unchanged with height (range) because wind direction is constant.

Figure 2.4c is analogous to Fig. 2.4b except that the surface wind speed now is two-thirds of the maximum value. The contours converge more rapidly here, than in Fig. 2.4b. The maximum in the vertical profile of horizontal wind speed remains unchanged and is indicated by the two crossmarks. Figure 2.4c exhibits a pattern representing weak wind shear oriented in the west-east direction. It is apparent that, while horizontal wind speed at the edge of the radar display remains unchanged, the stronger the surface winds, the more rapidly the contours converge until they become straight lines (Fig. 2.4d)--when both wind speed and direction are constant with height (same as Fig. 2.2b).

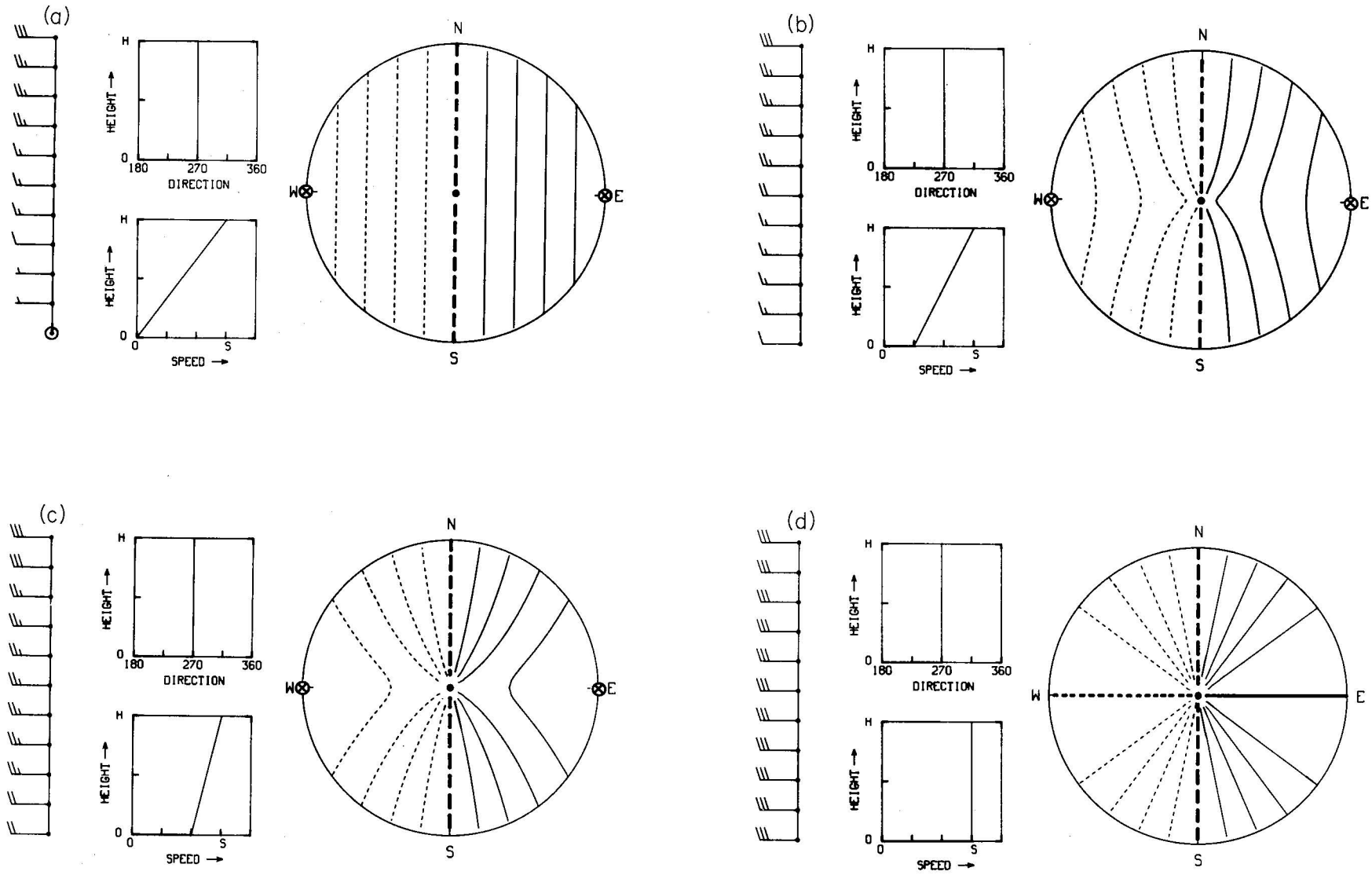

Fig. 2.4 Uniform wind speed shear with constant wind direction. Doppler velocity contours (as seen on circular radar display) have solid lines for flow away from radar, short dashes for flow toward radar and heavy long dashes for zero Doppler velocity. Circled x's or heavier solid and short dashed lines indicate locations of extreme Doppler velocity values within the display.

2.5 Nonuniform directional shear with constant wind speed

A nonlinear variation of wind direction with height (range) can be related to some nonuniformity of the environmental wind field. Four vertical profiles are described by

a) $spd(h) = S$
$dir(h) = 180°[1-(\frac{h}{H}) + (\frac{h}{H})^2]$

b) $spd(h) = S$
$dir(h) = 180°$

$$0 \leq h \leq H \qquad (8)$$

c) $spd(h) = S$
$dir(h) = 180°[1 + (\frac{h}{H}) - (\frac{h}{H})^2]$

d) $spd(h) = S$
$dir(h) = 180°[1 + 2(\frac{h}{H}) - 2(\frac{h}{H})^2]$.

These profiles are represented in corresponding Figs. 2.5a-d. As discussed in an earlier subsection, the zero velocity contour traces a letter "S" (backward "S") when winds veer (back) with height. A striking example (representing cold advection below and warm advection aloft) is observed in Fig. 2.5a. In this figure, the display is bisected by a backward "S" between the surface and midlevels, while above the midlevels the pattern is reversed by veering winds.

When the wind direction changes from its nonlinear variation to 180° at all altitude levels, Fig. 2.5b results. This figure is analogous to Fig. 2.3b which exhibits a constant wind direction and speed situation.

Warm advection in the lower layer topped by cold advection aloft is observed in Fig. 2.5c. This figure resembles Fig. 2.5a, except that the pattern is reversed; veering winds in the lower level are accompanied by backing winds aloft.

The strengths of veering and backing winds are indicated by change in the orientation of the zero velocity contour with height (range). By comparing Fig. 2.5c with Fig. 2.5d, we note greater curvature in the distribution of Doppler velocity components. This is due to an increased veering of winds up to midlevels, accompanied by an increased backing of winds aloft.

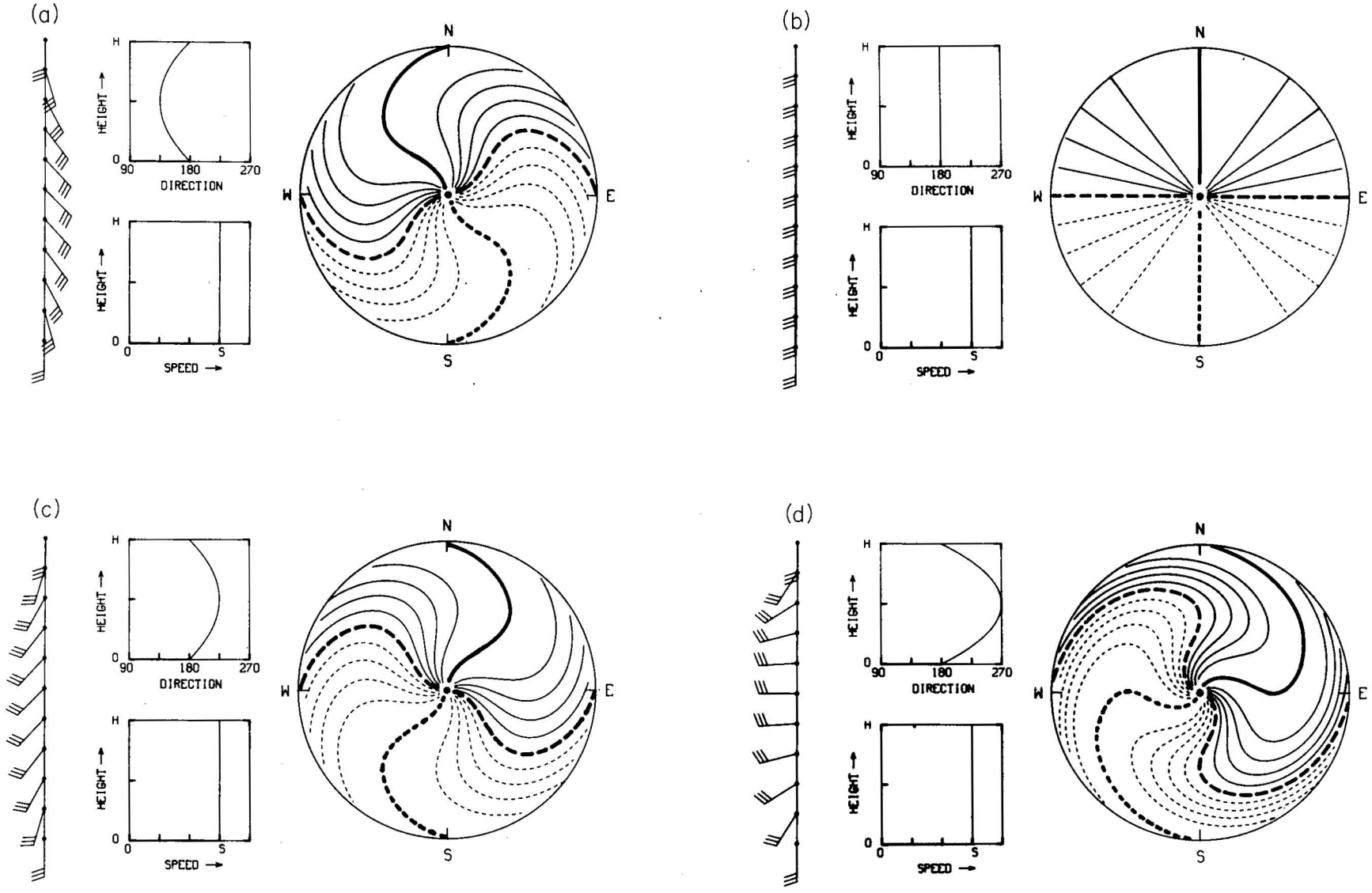

Fig. 2.5 Nonuniform direction shear with constant wind speed. Doppler velocity contours (as seen on circular radar display) have solid lines for flow away from radar, short dashes for flow toward radar and heavy long dashes for zero Doppler velocity. Heavier solid and short dashed lines indicate locations of extreme Doppler velocity values within the display.

2.6 Nonuniform wind speed shear with constant wind direction

In Sec. 2.5 we saw the influence of nonuniformity in the environmental wind direction. The following is a discussion of wind speed that varies parabolically with height, as in a jet stream. We present four vertical profiles describing the degree to which the speed changes nonlinearly with height (range) given by

a) $spd(h) = 4S\frac{h}{H}(1 - \frac{h}{H})$
$dir(h) = 270°$

b) $spd(h) = S[0.33 + 2.67\frac{h}{H}(1 - \frac{h}{H})]$
$dir(h) = 270°$

$0 \leq h \leq H \quad (9)$

c) $spd(h) = S[0.67 + 1.33\frac{h}{H}(1 - \frac{h}{H})]$
$dir(h) = 270°$

d) $spd(h) = S$
$dir(h) = 270°$

A maximum in the vertical profile of horizontal wind produces a pair of concentric ovals, one upwind and one downwind (Figs. 2.6a-c). This is due to the variation of the wind speed from zero at the ground, to a maximum at midlevels and to zero again at the top. Illustrated in Figs. 2.6b-c are the thin solid and short-dashed contours that tend to converge at the center of the radar display and that, now curved, are no longer parallel to the zero velocity contour. The degree to which the wind speed varies nonlinearly with height (range) can be determined qualitatively by noting the radial gradients in the distribution of radial velocity component when the radar is pointing in the direction of the maximum and minimum values. Figure 2.6a, for instance, indicates stronger west-east wind shear than Fig. 2.6b does. Even less wind shear is indicated in Fig. 2.6c. The weaker the wind shear, the more rapidly the contours converge until they become straight lines (Fig. 2.6d), as both wind direction and speed become uniform with height.

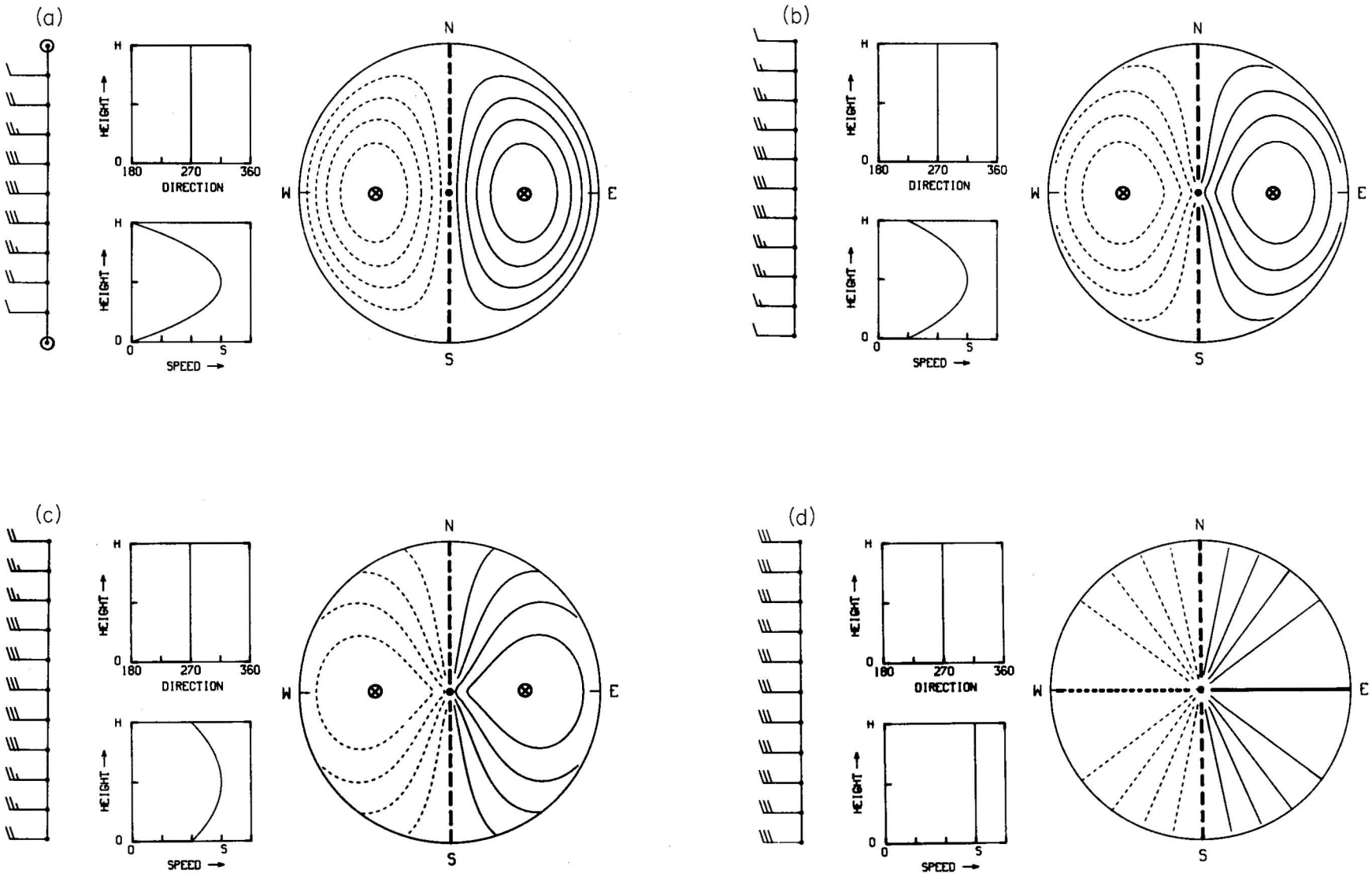

Fig. 2.6 Nonuniform wind speed shear with constant wind direction. Doppler velocity contours (as seen on circular radar display) have solid lines for flow away from radar, short dashes for flow toward radar and heavy long dashes for zero Doppler velocity. Circled x's or heavier solid and short dashed lines indicate locations of extreme Doppler velocity values within the display.

2.7 Uniform wind speed shear with uniform directional shear

This subsection deals with our consideration of uniformity of both wind direction and speed shears in the environmental wind field. We present four vertical profiles reflecting linear variations of wind direction and speed with height such that

a) $spd(h) = S(\frac{h}{H})$

$dir(h) = 180°[1 + 0.5(\frac{h}{H})]$

b) $spd(h) = 0.33S[1 + 2(\frac{h}{H})]$

$dir(h) = 180°[1 + 0.5(\frac{h}{H})]$

$$0 \leq h \leq H \qquad (10)$$

c) $spd(h) = 0.33S[2 + (\frac{h}{H})]$

$dir(h) = 180°[1 + 0.5(\frac{h}{H})]$

d) $spd(h) = S$

$dir(h) = 180°[1 + 0.5(\frac{h}{H})]$

Figures 2.7a-d illustrate an S-shaped warm advection pattern in which winds veer with height, as indicated by the zero velocity contour. The circled x's in Figs. 2.7a-c indicate wind maxima at azimuths 90° and 270° at the edge of the radar display, one upwind and one downwind.

Figure 2.7b, which is similar to Fig. 2.7a, exhibits the veering wind direction, except that we change the surface wind from zero to one-third of the maximum value of S at the ground. The zero velocity contour remains invariant with height. The curved contours appear to converge so that they produce a few S-shaped contours passing through the center. As seen inside the outermost slant range circle in Fig. 2.7b, the contours of Doppler velocity component change slightly.

In Fig. 2.7c, this S-shaped pattern has the appearance of the pattern of Fig. 2.7b, except that the curved contours converge even more. This is because the surface wind is now two-thirds of the maximum value of S. It is concluded that as the surface winds increase (vertical shear decreases), the curved contours tend to converge rapidly until all the contours become S-shaped lines when wind speed is constant with height, as evident in Fig. 2.7d. (This figure is identical to Fig. 2.3d.)

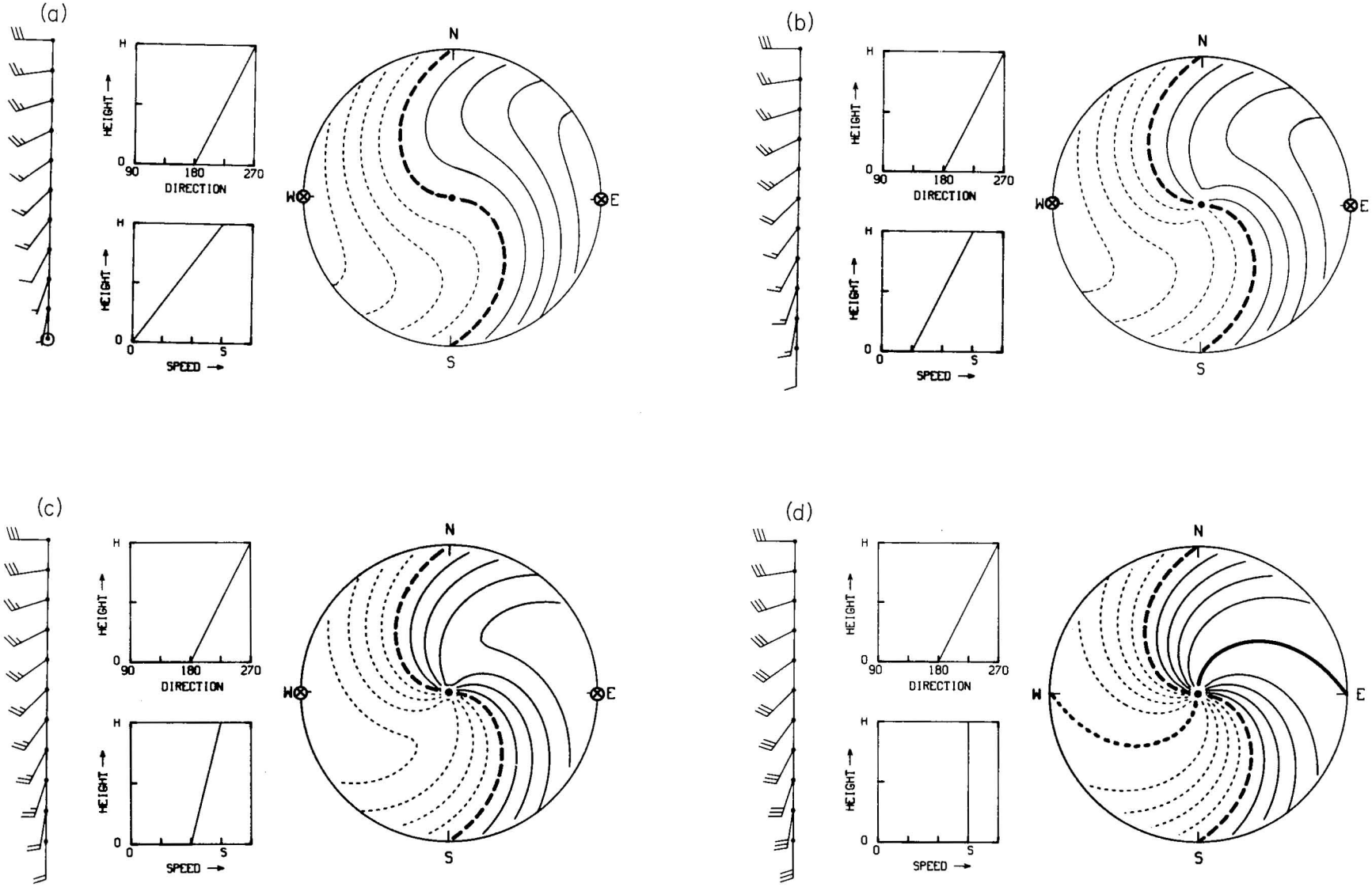

Fig. 2.7 Uniform wind speed shear with uniform directional shear. Doppler velocity contours (as seen on circular radar display) have solid lines for flow away from radar, short dashes for flow toward radar and heavy long dashes for zero Doppler velocity. Circled x's or heavier solid and short dashed lines indicate locations of extreme Doppler velocity values within the display.

2.8 Nonuniform directional shear with uniform speed shear

In this subsection, we consider wind direction varying parabolically with height, while the wind speed varies linearly. The wind direction and speed profiles shown in Figs. 2.8a-d are represented by

a) $spd(h) = S(\frac{h}{H})$

$dir(h) = 60°[3 + 4\frac{h}{H}(1 - \frac{h}{H})]$

b) $spd(h) = 0.33S[1 + 2(\frac{h}{H})]$

$dir(h) = 60°[3 + 4\frac{h}{H}(1 - \frac{h}{H})]$

$$0 \leq h \leq H \qquad (11)$$

c) $spd(h) = 0.33S[2 + (\frac{h}{H})]$

$dir(h) = 60°[3 + 4\frac{h}{H}(1 - \frac{h}{H})]$

d) $spd(h) = S$

$dir(h) = 60°[3 + 4\frac{h}{H}(1 - \frac{h}{H})]$.

In Figs. 2.8a-d, the vertical profiles indicate veering winds and warm air advection up to midlevels. At and above midlevels, winds back with height and cold air advection extends to the top. Further, changes in the linear wind speed profile produce additional changes in Doppler velocity contours. Note that the extreme horizontal wind speeds are represented by circled x's at azimuths 180° and 360° at the edge of the radar display. Exception is Fig. 2.8d which illustrates a constant wind speed where all contour lines pass through the origin of the display.

As already seen from our consideration of the variation of surface wind speeds, the stronger the surface winds, the more rapidly the contours converge at the center of the radar display. They become S-shaped contours up to midlevels and backward S-shaped from midlevels to the top when wind speed is constant at all altitudes.

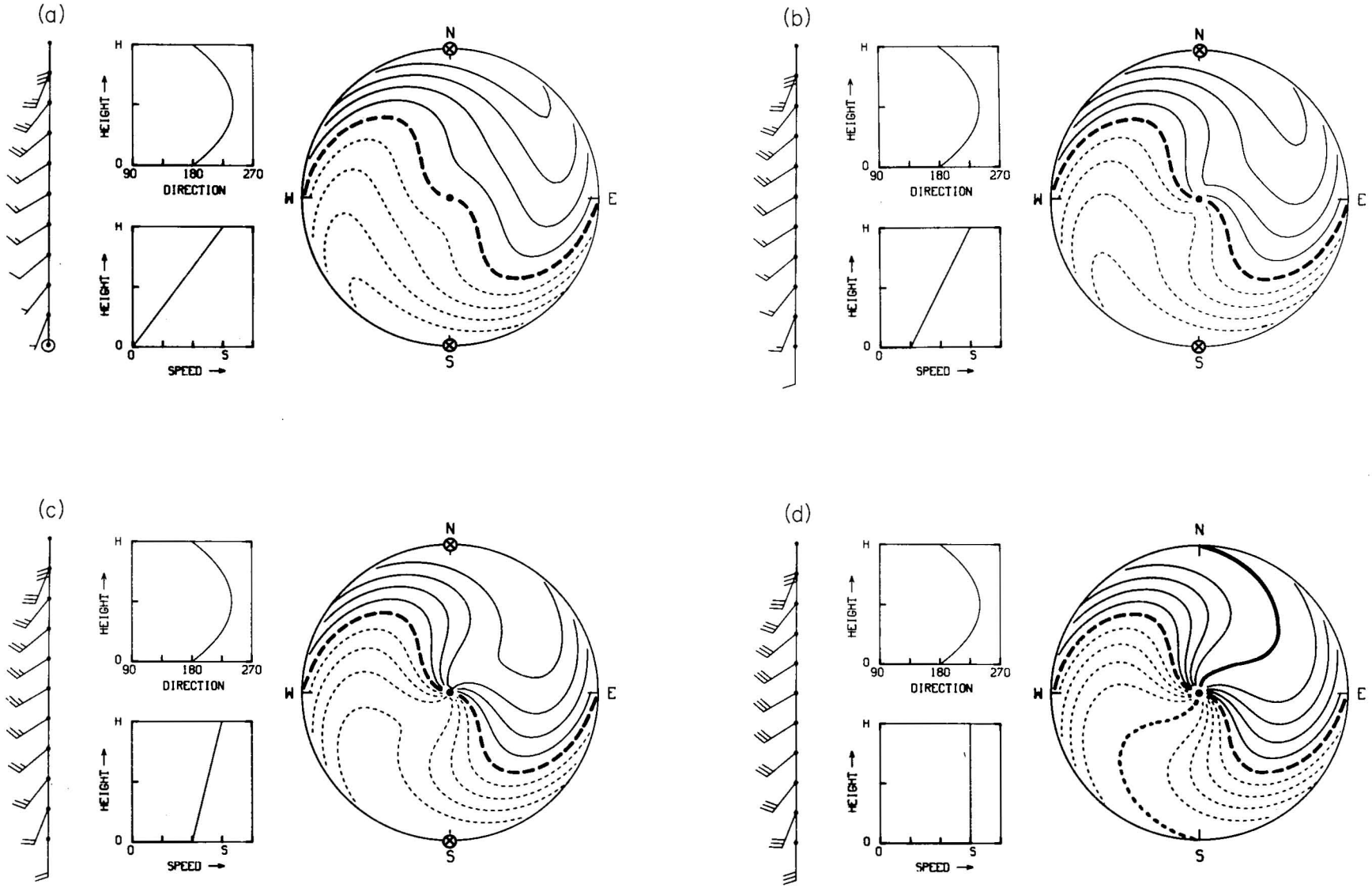

Fig. 2.8 Nonuniform directional shear with uniform speed shear. Doppler velocity contours (as seen on circular radar display) have solid lines for flow away from radar, short dashes for flow toward radar and heavy long dashes for zero Doppler velocity. Circled x's or heavier solid and short dashed lines indicate locations of extreme Doppler velocity values within the display.

2.9 Nonuniform wind speed shear with uniform directional shear

Recalling that Section 2.6 deals with parabolic variation of wind speed and constant wind direction with height, we wish to consider the same speed profile and uniformly varying wind direction with height. We describe four vertical profiles of wind direction and speed as

a) $spd(h) = 4S\frac{h}{H}\left[1 - \frac{h}{H}\right]$
$dir(h) = 90°\left[2 + \left(\frac{h}{H}\right)\right]$

b) $spd(h) = 0.33S\left[1 + 8\frac{h}{H}\left(1 - \frac{h}{H}\right)\right]$
$dir(h) = 90°\left[2 + \left(\frac{h}{H}\right)\right]$

$$0 \leq h \leq H \qquad (12)$$

c) $spd(h) = 0.67S\left[1 + 2\frac{h}{H}\left(1 - \frac{h}{H}\right)\right]$
$dir(h) = 90°\left[2 + \left(\frac{h}{H}\right)\right]$

d) $spd(h) = S$
$dir(h) = 90°\left[2 + \left(\frac{h}{H}\right)\right]$.

The vertical profiles of wind direction produce S-shaped zero velocity contours (thick, long-dashed) that bisect the radar displays (Figs. 2.9a-d). Except for Fig. 2.9d, each set of bean-shaped contours is centered around the point of maximum (minimum) wind speed (indicated by circled x's) at midlevels and azimuths 45° and 225°--representing a wind direction of 225° at that height. With winds increasing at the surface and the top height from Fig. 2.9a through 2.9d, the curved contours approach the center and the edge of the display, until they all become S-shaped when the wind speed S is constant with height (Fig. 2.9d).

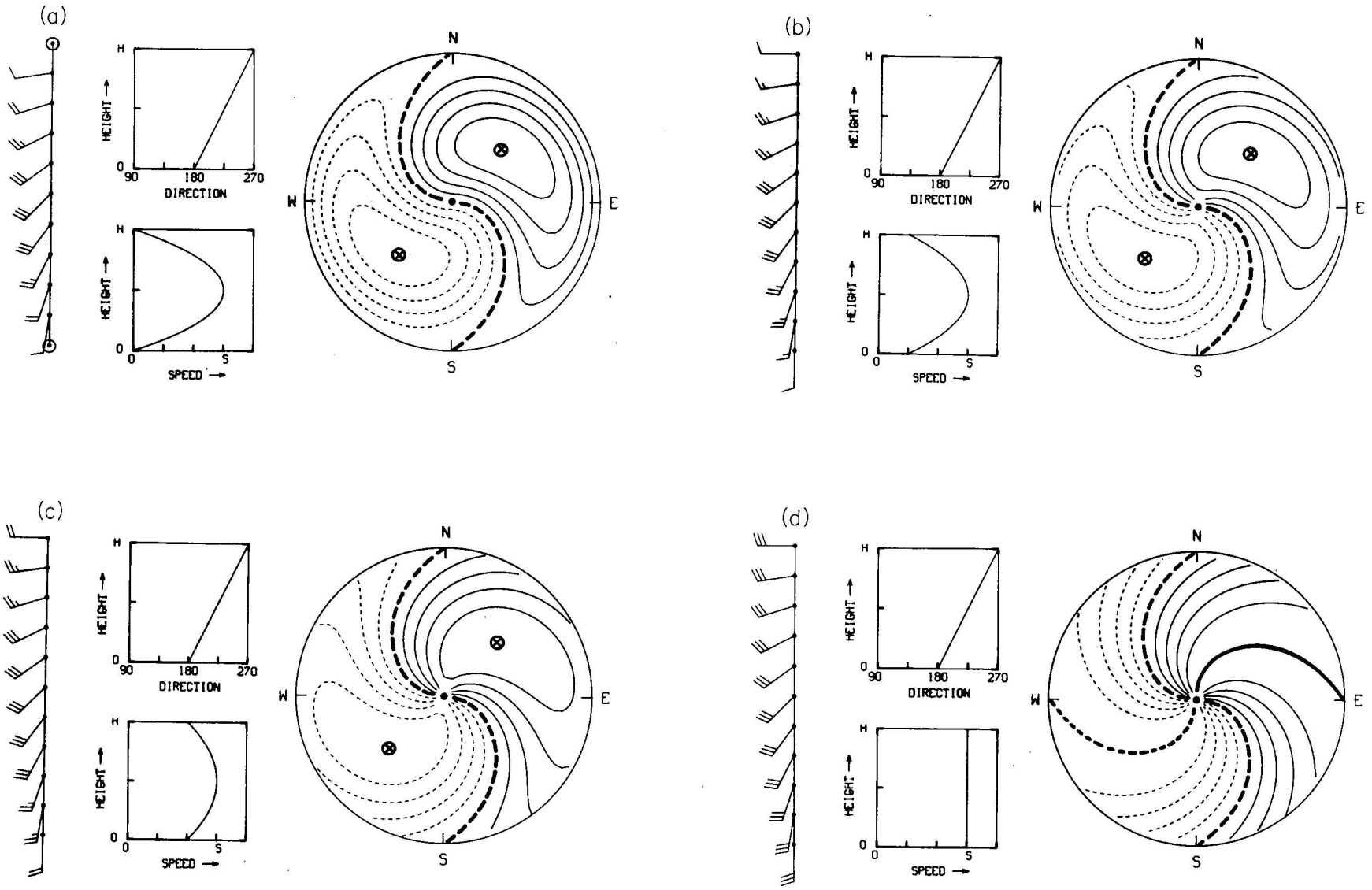

Fig. 2.9 Nonuniform wind speed shear with uniform directional shear. Doppler velocity contours (as seen on circular radar display) have solid lines for flow away from radar, short dashes for flow toward radar and heavy long dashes for zero Doppler velocity. Circled x's or heavier solid and short dashed lines indicate locations of extreme Doppler velocity values within the display.

2.10 Nonuniform wind speed shear with nonuniform directional shear

Four vertical profiles given in Figs. 2.10a-d and illustrating the degree to which veering and backing winds varying parabolically with height are represented by

a) $spd(h) = 4S\frac{h}{H}(1 - \frac{h}{H})$

$dir(h) = 60°[3 + 4\frac{h}{H}(1 - \frac{h}{H})]$

b) $spd(h) = S[0.33 + 2.67\frac{h}{H}(1 - \frac{h}{H})]$

$dir(h) = 60°[3 + 4\frac{h}{H}(1 - \frac{h}{H})]$

$0 \leq h \leq H$ (13)

c) $spd(h) = S[0.67 + 1.33\frac{h}{H}(1 - \frac{h}{H})]$

$dir(h) = 60°[3 + 4\frac{h}{H}(1 - \frac{h}{H})]$

d) $spd(h) = S$

$dir(h) = 60°[3 + 4\frac{h}{H}(1 - \frac{h}{H})]$.

A striking example of warm advection below and cold advection aloft is observed in the Doppler velocity fields. The displays are bisected by an S-shaped zero line between the surface and the midlevels (between the center of the radar display and the midranges); above the midlevels, the patterns are reversed because of backing winds.

Other interesting features of the radar display are a pair of closed contours that represent Doppler velocity maximum and minimum. At these azimuths and heights (midlevel), the radar beam is oriented parallel with the wind direction and, therefore, measures a component equal in magnitude to the maximum wind speed S.

The wind speed shear is another important feature of the display. Changes in wind speed at the ground may be obtained by noting that the contours converge at the origin of the radar display, except the zero velocity contour which remains invariant with range (height). Also, the pair of closed contours expand until they become curved lines when the wind speed is constant at all heights (Fig. 2.10d).

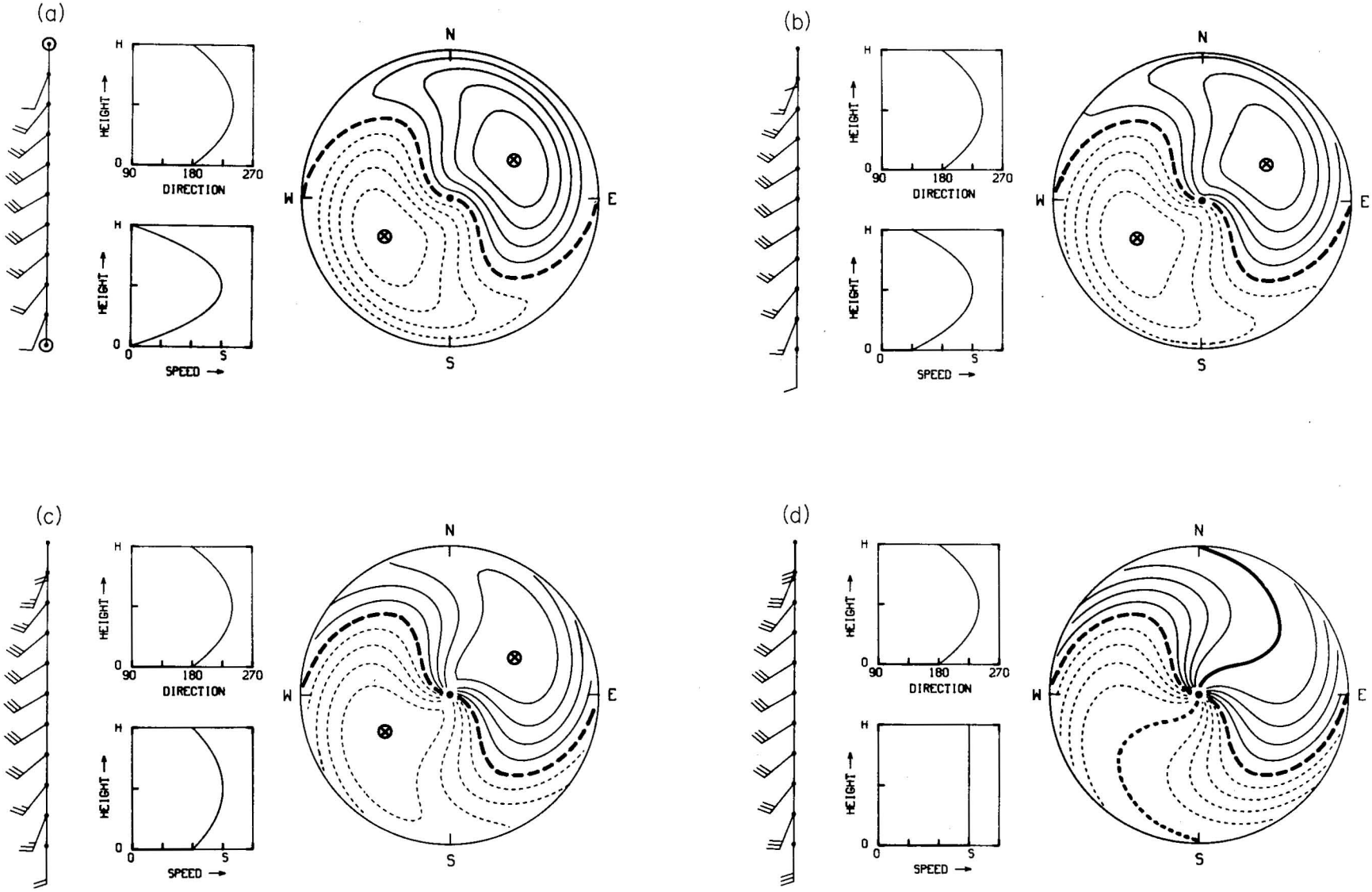

Fig. 2.10 Nonuniform wind speed shear with nonuniform directional shear. Doppler velocity contours (as seen on circular radar display) have solid lines for flow away from radar, short dashes for flow toward radar and heavy long dashes for zero Doppler velocity. Circled x's or heavier solid and short dashed lines indicate locations of extreme Doppler velocity values within the display.

2.11 Summary

Representative samples of single Doppler velocity patterns that can be found in optically clear air and in widespread precipitation are displayed in Fig. 2.11. The signatures are divided into three wind speed and three direction categories: (1) constant value with height, (2) linear change with height and (3) parabolic change with height.

When wind speed is constant (nonzero) with height (left column) all Doppler velocity contours pass through the radar location at the center of the display. Also, maximum and minimum Doppler velocities occur all along the heavier (nonzero) contour lines rather than just at one point (circled x) as with other speed profiles.

When wind speed is not zero at the ground, contour lines representing wind speed magnitudes less than or equal to the surface value pass through the radar location at display center (e.g., Fig. 2.4 and left column of Fig. 2.11). When the surface speed is zero, only the zero Doppler velocity contour (long, thick dashes) passes through the center of the radar display (middle and right column).

If the wind speed profile has a peak within the height interval on the display, there will be a pair of closed contours 180° from each other; the azimuth of the minimum is the direction from which the velocity jet is blowing and the height of the peak value can be computed from the radar antenna's elevation angle and the slant range (r_s) to that point.

Whereas the wind speed profile controls the overall pattern including the spacing between contours, the vertical profile of wind direction controls contour curvature. The most informative contour for wind direction is the zero velocity contour (thick long dashes). Note that the zero contours are identical in each row (reflection of wind direction profile) even though the overall patterns in each row differ significantly (reflection of wind speed profile).

Since wind direction is perpendicular to a radial line (from display center) at the point where it intersects the zero contour, wind direction variation with height (range on the radar scope) can be determined by inspection. Wind blows from the negative toward the positive side. Looking at the center radar display, we see that there are southerly winds at the ground--the zero line is oriented east-west and air is approaching from the south and flowing away toward the north. Halfway between the center and edge of the display, southwesterly winds are perpendicular to the radial line. At the edge of the display, wind is from the west because the radial line intersecting the zero contour is oriented north-south.

Kraus and Donaldson (1976) also present some single Doppler velocity fields like those simulated in this section. Their interpretations of the fields are the same as ours.

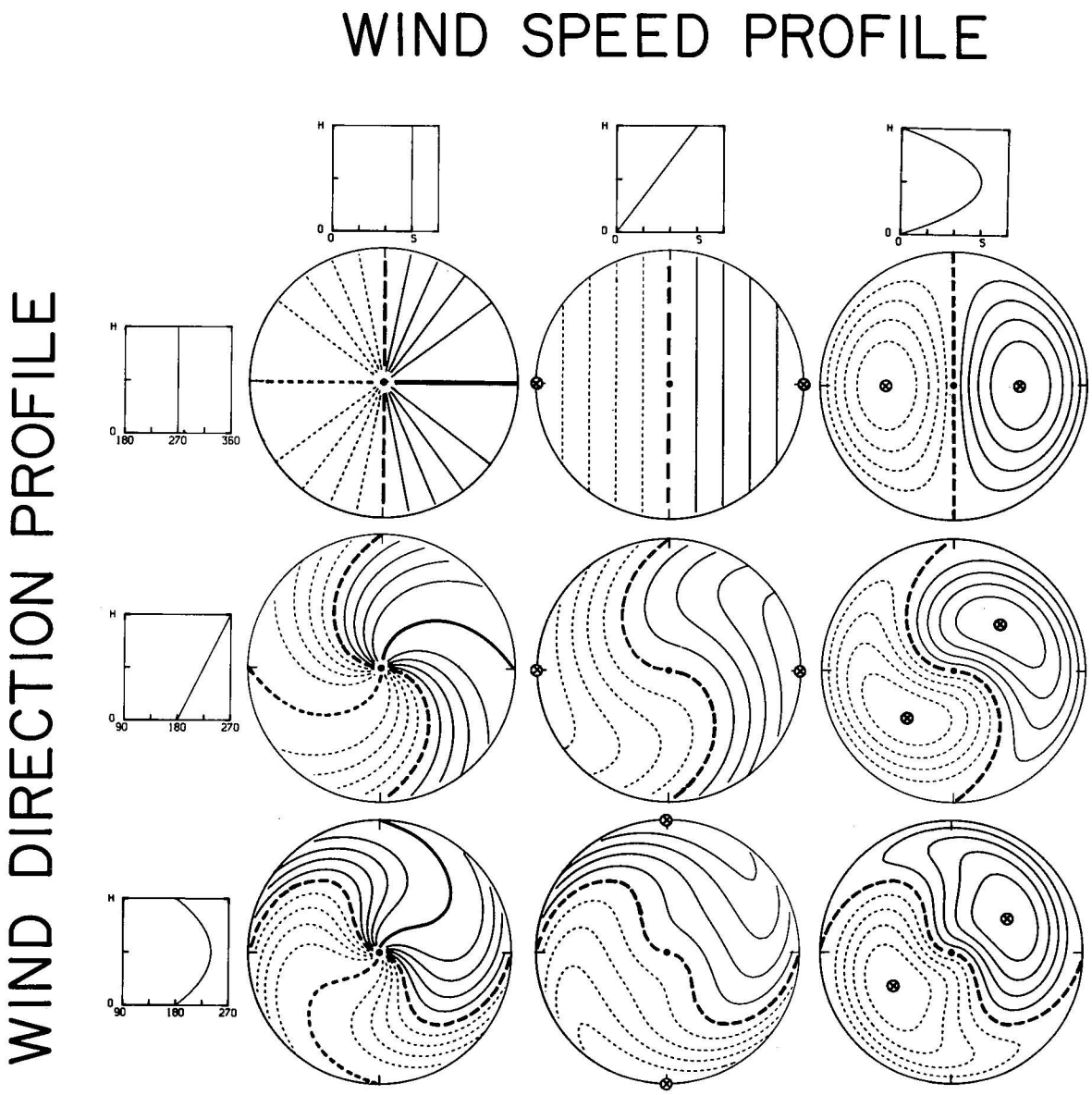

Fig. 2.11 Doppler velocity patterns (constant elevation PPI scans) for various vertical profiles of wind speed and direction.

3. IDEALIZED STORM WIND FIELDS

3.1 Single Doppler velocity signatures of mesocyclones and divergence areas

Single Doppler velocity signatures of rotation and divergence help to identify severe storms. Axisymmetric mesocyclone and divergence/convergence areas can be modeled using a Rankine combined velocity profile (Fig. 3.1a). The profile consists of two distinct velocity distributions. The inner portion of the profile increases linearly with distance from the center:

$$v = C_1 r \quad . \tag{14}$$

In the outer portion, velocity change is inversely proportional to distance from the center:

$$v = C_2/r \quad . \tag{15}$$

The inner part of the profile will be referred to as the core region, R_c being the core radius. The maximum velocity, V_x, in the profile occurs at the core radius. Once R_c and V_x are specified, the entire profile can be determined using the constants

$$C_1 = V_x/R_c \tag{16}$$

$$C_2 = V_x R_c \quad . \tag{17}$$

From (14) through (17), it follows that

$$v = V_x \phi(r) \quad , \tag{18}$$

where $\phi(r)$ represents the combined velocity profile and is given by

$$\phi(r) = \begin{cases} r/R_c \text{ when } r \leq R_c \\ R_c/r \text{ when } r \geq R_c \end{cases} \quad . \tag{19}$$

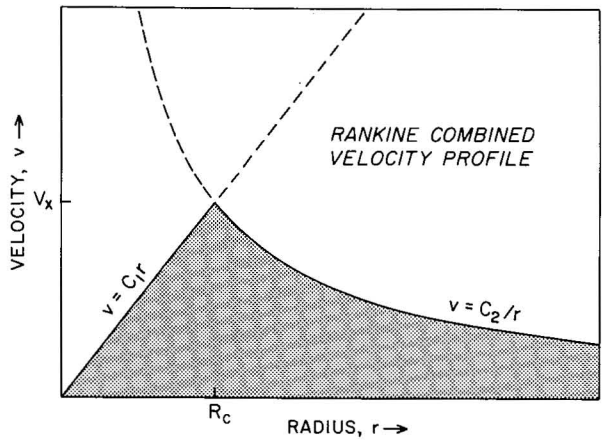

Fig. 3.1a A Rankine combined velocity profile. Maximum velocity (V_x) occurs at core radius (R_c).

3.1a Mesocyclone signature

The combined velocity profile originally was developed to describe axisymmetric vortices (e.g., Rankine, 1901). For a vortex, v_t represents tangential (rotational) velocity and V_t represents peak tangential velocity which occurs at the core radius, R_t. Since tangential velocity increases linearly with radius within the core region ($r \leq R_t$) the core rotates like a vertical solid cylinder (having a circular horizontal cross-section). The cylinder thus represents the driving force that keeps the surrounding fluid (water or air) rotating; fluid tangential velocity changes inversely with distance from the rotation center ($r_t > R_t$). The solidly rotating core has the velocity distribution given by

$$v_t = V_t \phi_t(r) > 0 \quad \text{for cyclonic} \quad \text{when } V_t > 0$$

$$v_t = V_t \phi_t(r) < 0 \quad \text{for anticyclonic} \quad \text{when } V_t < 0, \tag{20}$$

where $\phi_t(r)$ represents the radial profile of V_t given by

$$\phi_t(r) = \begin{cases} \dfrac{r}{R_t} & \text{when } r \leq R_t \\ \dfrac{R_t}{r} & \text{when } r \geq R_t \end{cases} .$$

By analogy, a fluid vortex can be thought of as having a core that rotates as if it were a solid. This model is a good first approximation for describing atmospheric vortices ranging in size from dust devils to hurricanes. The key parameters needed to specify a vortex in nature are the core radius and the maximum tangential velocity. These two parameters form the basis for the single Doppler velocity signature of a mesocyclone.

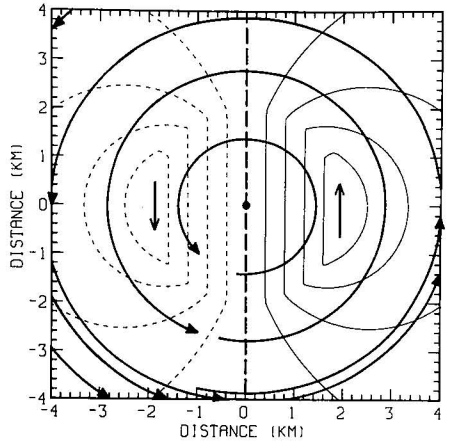

Fig. 3.1b Vortex flow (heavy streamlines) and corresponding single Doppler velocity signature (thin lines); radar is south of flow field.

Figure 3.1b shows a horizontal scan through a vortex (thick circular lines) rotating around a vertical axis and the associated single Doppler velocity pattern (thinner lines--lines having constant Doppler velocity values). A Doppler radar is assumed to be located a considerable distance due south of the vortex center. Since a Doppler radar senses only the component of flow in the radar viewing direction, the heavy dashed line represents zero Doppler velocity because flow everywhere along the line is perpendicular to the viewing direction. To the right of the line, flow is away from the radar (thin solid contours) and flow on the left is toward the radar (thin dashed contours). Whereas a Doppler radar senses none of the flow when viewing a vortex through the circulation center, it senses the complete flow on both sides of the center where flow is directly toward or away from the radar. The arrows either side of center represent the core radius (R_t) where the full value of the peak tangential velocity (V_t) is measured.

Therefore the single Doppler velocity signature of a mesocyclone (or any vortex) has a pattern that is symmetric about the radar viewing direction and has peak values (V_t) of opposite sign at the core radius (R_t) either side of the circulation center. According to a study of mesocyclone signatures within Oklahoma severe storms (Burgess, 1976), typical core radii are 2.5 to 3 km and typical peak tangential velocity values are 20 to 25 m s^{-1}.

If the vortex is moving and/or is embedded in a uniform horizontal flow field, the circulation no longer will be circular, but the vortex signature pattern will remain unchanged; the only difference will be that the contour lines will have different values and the center contour no longer will have a Doppler velocity value of zero.

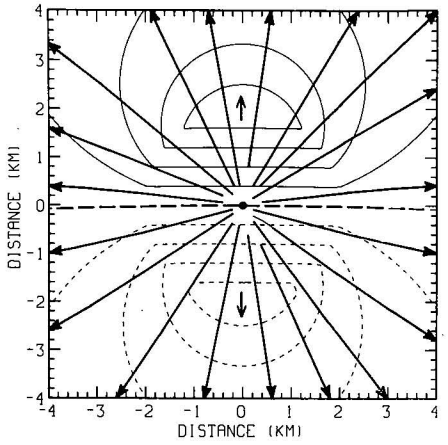

Fig. 3.1c Divergent flow (heavy streamlines) and corresponding single Doppler velocity signature (thin lines); radar is south of flow field.

3.1b Divergence signature

The Rankine combined profile also can be used to model axisymmetric divergence (convergence) areas. Mathematically, the velocity distribution is given by

$$v_r = V_r \phi_r(r) > 0 \quad \text{for divergence when} \quad V_r > 0$$
$$v_r = V_r \phi_r(r) < 0 \quad \text{for convergence when} \quad V_r < 0 \qquad (21)$$

where $\phi_r(r)$ represents the combined velocity profile of V_r

$$\phi_r(r) = \frac{r}{R_r} \quad \text{when} \quad r \le R_r$$
$$\frac{R_r}{r} \quad \text{when} \quad r \ge R_r \ .$$

In this case, v_r represents radial velocities flowing directly inward toward or outward from the center of the model; V_r is the peak radial velocity at the core radius R_r. Since radial velocity changes at a constant rate with increasing radius in the core region ($r \le R_r$), horizontal divergence is constant within the core.

A model radial flow field and the corresponding single Doppler velocity pattern is shown in Fig. 3.1c. Note that the divergence signature is the same as a mesocyclone signature that has been rotated counterclockwise by 90°. Here the zero line is perpendicular to the radar viewing direction because the radar does not sense motion toward the east or west of the divergence center. Maximum flow toward and away from the radar (short arrows) is V_r measured along the viewing direction that passes through the divergence center; these peak velocities occur at the core radius (R_r).

3.1c Simulation procedure

Simulated Doppler velocity fields are generated by using combinations of mesocyclone, divergence and environmental flow models. Horizontal wind components are computed at Cartesian (x,y) grid points in a horizontal analysis plane. This plane is assumed to coincide with a flat earth's surface. Here, we use a right-hand orthogonal coordinate system in which x and y refer to the horizontal coordinates relative to the origin at the center of the grid. The coordinate system conventions are illustrated in Fig. 3.1d. If the radar is assumed to be located south of the grid, then R_o is the horizontal distance from the radar to the grid origin (x,y=0,0). The vertical component of velocity is neglected because we assume that the elevation angle is small and the sum of air velocity and terminal fall speed is small relative to the horizontal wind.

For an arbitrary point (x,y) on the flat plane of the analysis grid, we define U* (x,y) and V* (x,y) to be the components of the horizontal wind velocity in the directions of the x and y axes, respectively. They may be expressed by

$$U^*(x,y) = U_{env} + \sum_{i=1}^{n} U_i(x,y)$$
$$V^*(x,y) = V_{env} + \sum_{i=1}^{n} V_i(x,y) \quad , \tag{22}$$

where the environmental wind components are given by

$$U_{env} = spd \cos(270° - dir)$$
$$V_{env} = spd \sin(270° - dir) \quad , \tag{23}$$

and where spd represents environmental wind speed, and dir the direction from which the wind blows. The velocity components for the i^{th} flow feature are

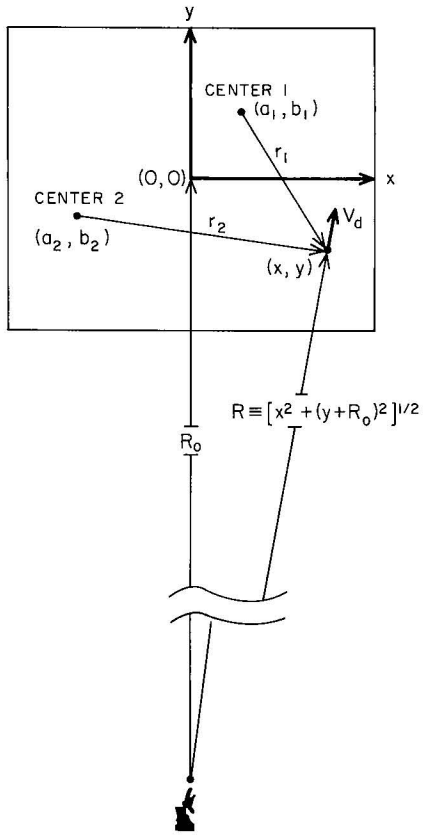

Fig. 3.1d Geometry for computing single Doppler velocity values within the analysis grid relative to the radar position.

$$U_i(x,y) = V_{ri} \frac{x_i}{r_i} - V_{ti} \frac{y_i}{r_i}$$

$$V_i(x,y) = V_{ri} \frac{y_i}{r_i} + V_{ti} \frac{x_i}{r_i} \quad , \qquad (24)$$

where V_{ri}, V_{ti} are the radial and tangential velocity components of the i^{th} flow feature at a distance r_i from the feature center (a_i,b_i). Distance components x_i and y_i are measured from the feature center, that is,

$$x_i = x - a_i$$

$$y_i = y - b_i$$

and

$$r_i = (x_i^2 + y_i^2)^{1/2}$$

As illustrated in Fig. 3.1d, the radar measures the simulated Doppler velocity

$$V_d(x,y) = \frac{1}{R(x,y,R_o)} [xU^*(x,y) + (y+R_o)\, V^*(x,y)] \qquad (25)$$

where

$$R(x,y,R_o) = [x^2 + (y+R_o)^2]^{1/2} \quad .$$

In this equation, the sum of the air vertical velocity and the terminal fall speed is assumed to be negligible, as already discussed. Eq. (25) is similar to that used by Peace et al. (1969).

For the simulated single Doppler velocity patterns shown in Sections 3 and 4, a simplifying assumption has been made. The radar is assumed to be so far away from the analysis grid that all simulated Doppler velocity components are parallel to the y axis. In this case, Eq. (25) simplifies to

$$V_d(x,y) = \frac{y + R_o}{R(x,y,R_o)} V^*(x,y) \quad .$$

3.2 Circulation and divergence/convergence centers having identical size and strength

Interpretation of storm severity depends upon ability to recognize single Doppler velocity patterns of circulation and divergence/convergence areas. The simplest patterns occur when the core radii and peak velocities for circulation and divergence are the same. Input parameters for the four combinations of cyclonic rotation ($V_t>0$), anticyclonic rotation ($V_t<0$), divergence ($V_r>0$) and convergence ($V_r<0$) are presented schematically in Figs. 3.2a-d.

The corresponding single Doppler velocity patterns (assuming the radar to be to the south) appear in Figs. 3.2e-h; the associated horizontal flow fields are in Figs. 3.2i-l. The patterns turn out to be the same as for pure rotation (Fig. 3.1b) and pure divergence (Fig. 3.1c); the orientation of the pattern--in particular, the zero contour--is the contrasting feature. For example, note that the divergent cyclonic circulation pattern (Fig. 3.2g) is midway between pure cyclonic circulation (Fig. 3.1b) and pure divergence (Fig. 3.1c).

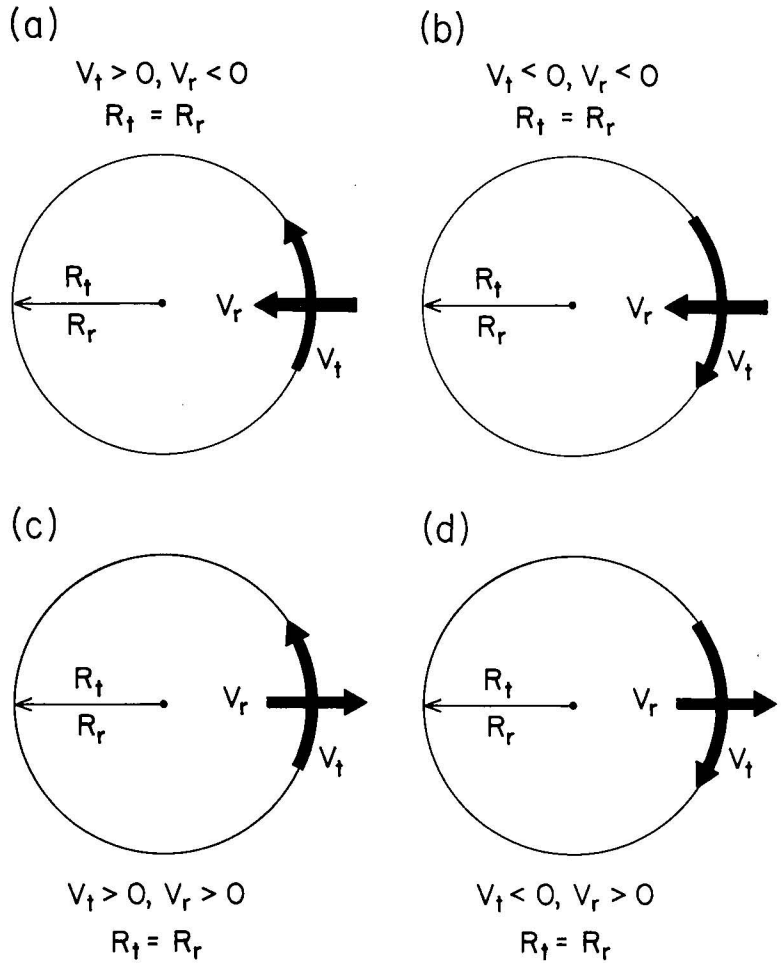

Fig. 3.2a-d Rotation (V_t,R_t) and divergence (V_r,R_r) parameters used to produce the corresponding single Doppler velocity patterns (Figs. 3.2e-h) and horizontal streamlines (Figs. 3.2 i-l).

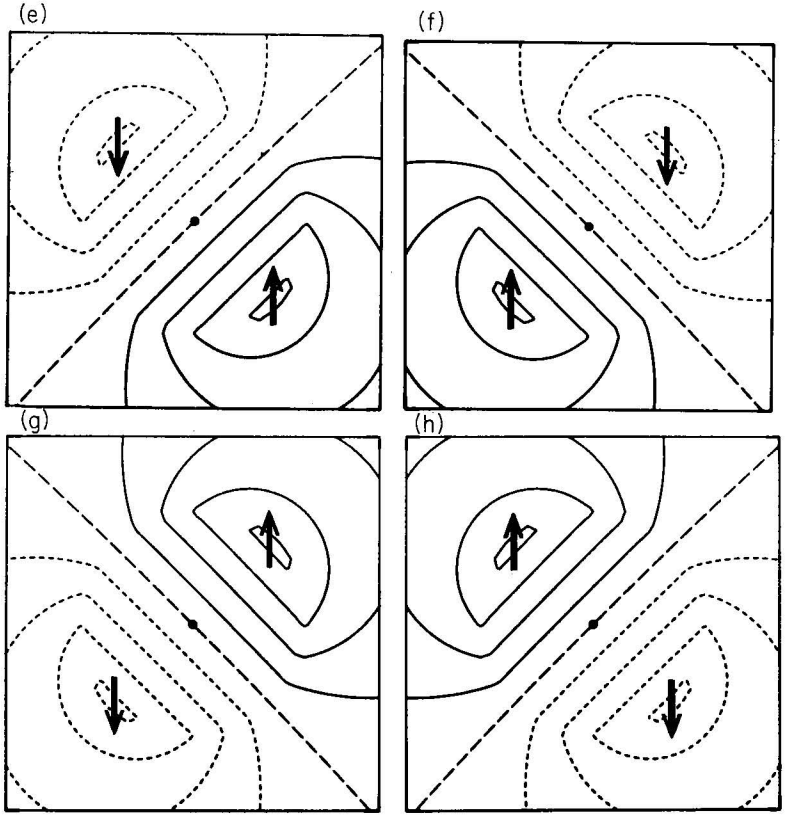

Fig. 3.2e-h Single Doppler velocity patterns corresponding to the flow model parameters in Figs. 3.2a-d; (e) convergent cyclonic flow, (f) convergent anticyclonic flow, (g) divergent cyclonic flow, (h) divergent anticyclonic flow. Radar is south of flow field.

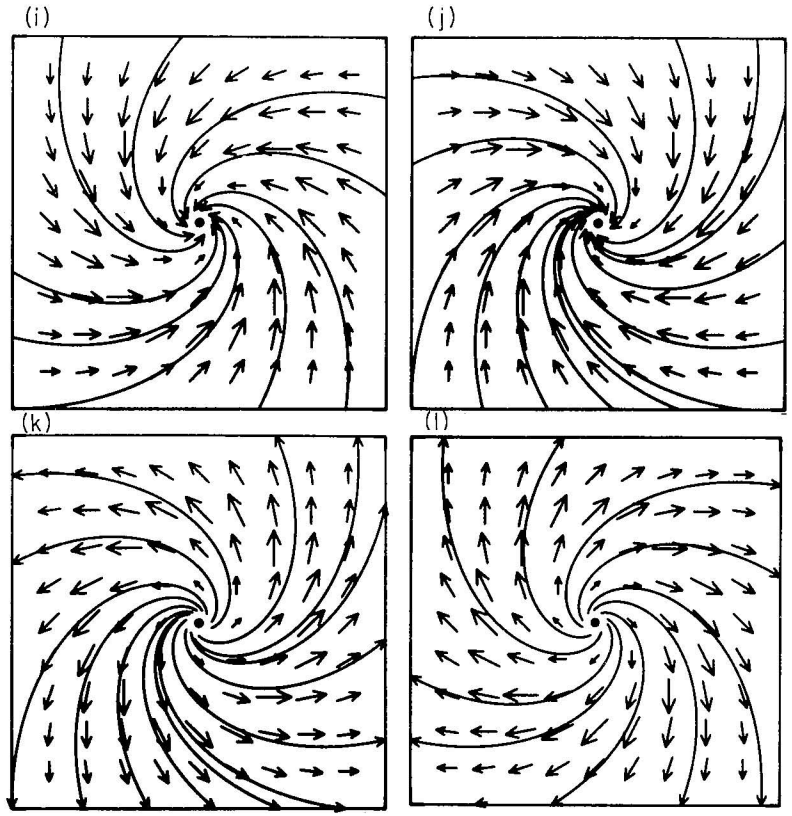

Fig. 3.2i-l Horizontal wind vectors and streamlines corresponding to the flow model parameters in Figs. 3.2a-d.

3.3 Circulation and divergence/convergence centers having varying size and strength

Having gained some confidence in interpretating and recognizing the significant features of Figs. 3.2e-h, we extend our analysis by investigating combinations of pure cyclonic circulation and pure convergence with varying core radii and radial and tangential velocity maxima. The key parameters used to describe the strength and size of circulation in comparison with those of convergence are the ratios of $-V_r$ to $+V_t$, and the ratio of R_r to R_t. Examples of the variations of R_r relative to R_t are given in Figs. 3.3a-c.

To begin the interpretation, consider Figs. 3.3e,h,k. By keeping core radii constant (R_r=R_t) and varying the values of $-V_r/V_t$ from 1/4 to 1 to 4, the velocity pattern changes in a clockwise direction. Consequently, a primarily cyclonic circulation (Fig. 3.3k) changes to a convergent mesocyclone (Fig. 3.3h) then to nearly a convergent flow field with little evidence of cyclonic circulation (Fig. 3.3e). Note that Fig. 3.3h and Fig. 3.2e are identical. Streamlines superimposed on the wind vector fields are illustrated in Figs. 3.3n,q,t. Differences in the streamline patterns are indicative of different strength in the ratio of $-V_r$ to V_t.

If a strong convergent flow field with a small core radius is embedded in a larger but weaker circulation, Fig. 3.3d results. In this case, the peak radial velocity V_r is four times the peak tangential velocity; the convergence's core radius is one fourth the circulation's core radius. At the other extreme, a strong, small circulation embedded in a larger weakly convergent flow field results in the pattern shown in Fig. 3.3 l. This occurs when $V_r = -1/4\ V_t$ and $R_r = 4R_t$. The corresponding horizontal flow fields show a stronger spiral in the converging flow in Fig. 3.3u than in Fig. 3.3m.

Looking more carefully at Figs. 3.3f,j, we note that the convergence signature contains some cyclonic circulation at the center and the mesocyclone signature is partly convergent at the center, respectively. In these examples, the ratio of $-V_r$ to V_t is 4 and the ratio of R_r to R_t is 4 in Fig. 3.3f; $-V_r/V_t = 1/4$ and R_r/R_t=1/4 in Fig. 3.3j. The corresponding flow fields are found in Figs. 3.3o,s.

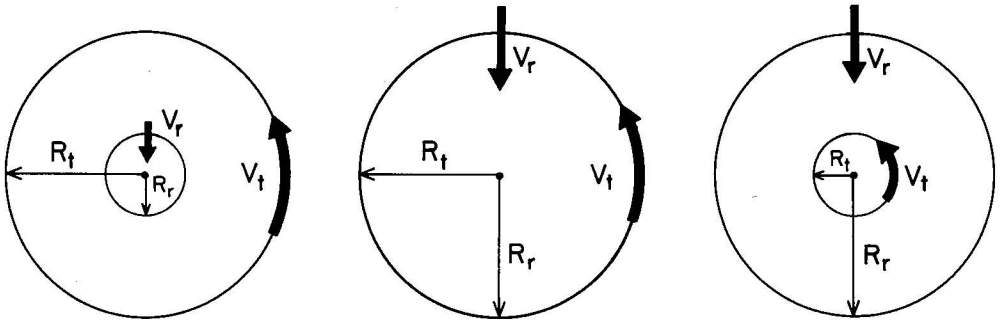

Fig. 3.3a-c Relationship of rotation (R_t) and convergence (R_r) core radii used in the accompanying single Doppler velocity patterns (Figs. 3.3d-l) and streamline flow patterns (Figs. 3.3m-u).

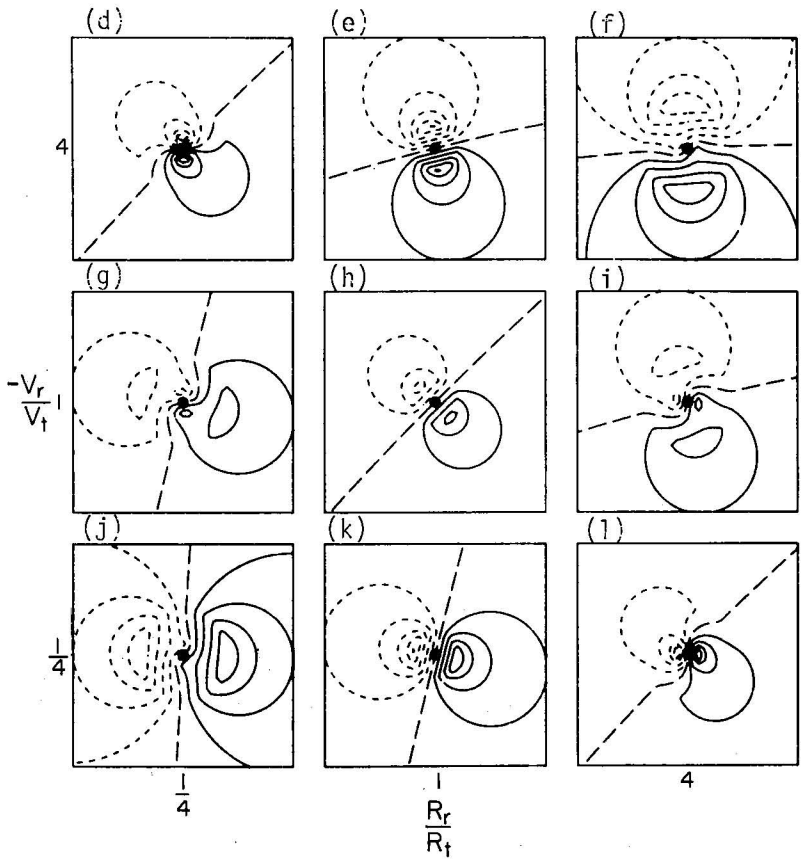

Fig. 3.3d-l Single Doppler velocity patterns for varying ratios of peak core velocities and core radii. Convergence is represented by $-V_r, R_r$ and rotation is represented by V_t, R_t. Radar is south of flow field.

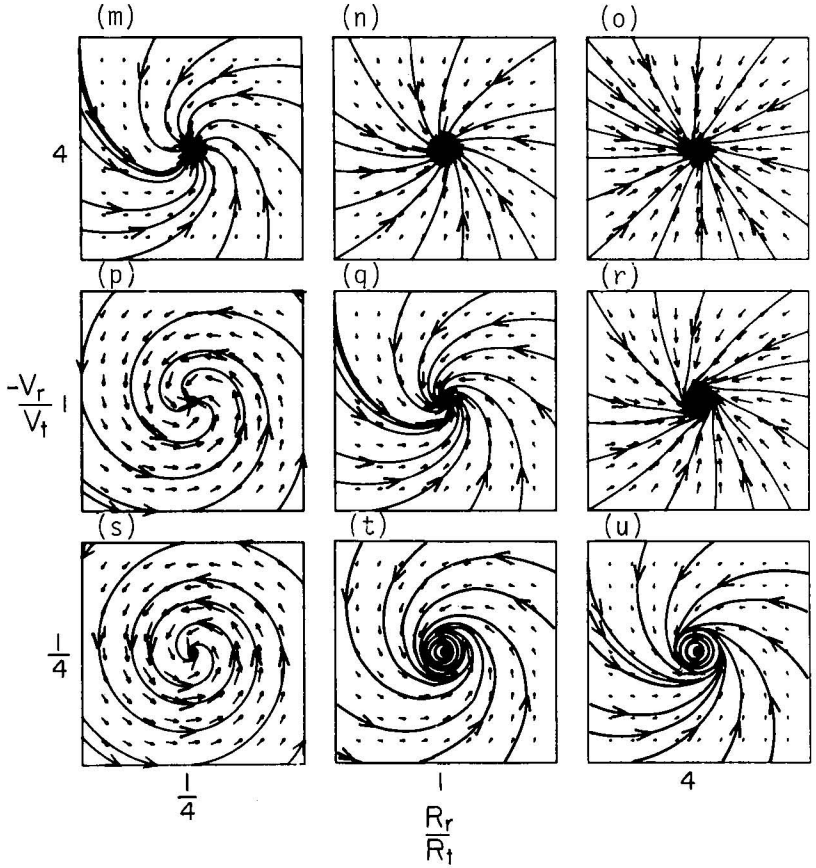

Fig. 3.3m-u Horizontal flow fields corresponding to the single Doppler velocity patterns in Figs. 3.3d-l.

3.4 Two circulation centers of identical size and strength

Doppler velocity measurements in severe storms indicate that mesocyclones go through a regeneration process; one core dies out as a new one forms near it within the same overall circulation (Burgess et al., 1982). These effects are investigated using double-core mesocyclones having equal core radii and peak tangential velocities. The mesocyclone cores are rotated at various angles from the perpendicular position relative to the radar viewing direction. Also, their separation distance is varied.

Figures 3.4a-i show the results of simulations of single Doppler velocity patterns as the axis through the center of two cores is rotated counterclockwise through 90° (0° to 45° to 90°) and the separation distance increases. The patterns would be reversed (mirror image) if the cores were rotated clockwise. The separation distince (D) between core centers is normalized by the core radius (R). For example, the distance between the cores is equal to twice the core radius, i.e., D/R=2, in Figs. 3.4a-c. Note that the open dot is the center of mass of the two mesocirculations, and two dark dots represent the centers of the cores. According to mesocyclone statistics (Burgess, 1976), the average core radius of mesocyclones is 2.5 to 3 km.

When D/R=2 (Figs. 3.4a-c), the edges of the two cores touch each other. The corresponding flow fields (Figs. 3.4j-l) are elliptical within and adjacent to the cores and become circular at great distance from the center. Since the cores are so close to each other, the three Doppler velocity fields have the same overall configuration as a single core circulation (compare with Fig. 3.1b).

As D/R increases to 3, the fact that there are two cores becomes more evident. For D/R=4, separation of the two cores is obvious. The corresponding flow fields (Figs. 3.4m-r) become more elliptical and two circulations appear between the core centers. On the basis of a limited sample (e.g., Wood et al., 1979), D/R in nature probably lies between 2 and 3.

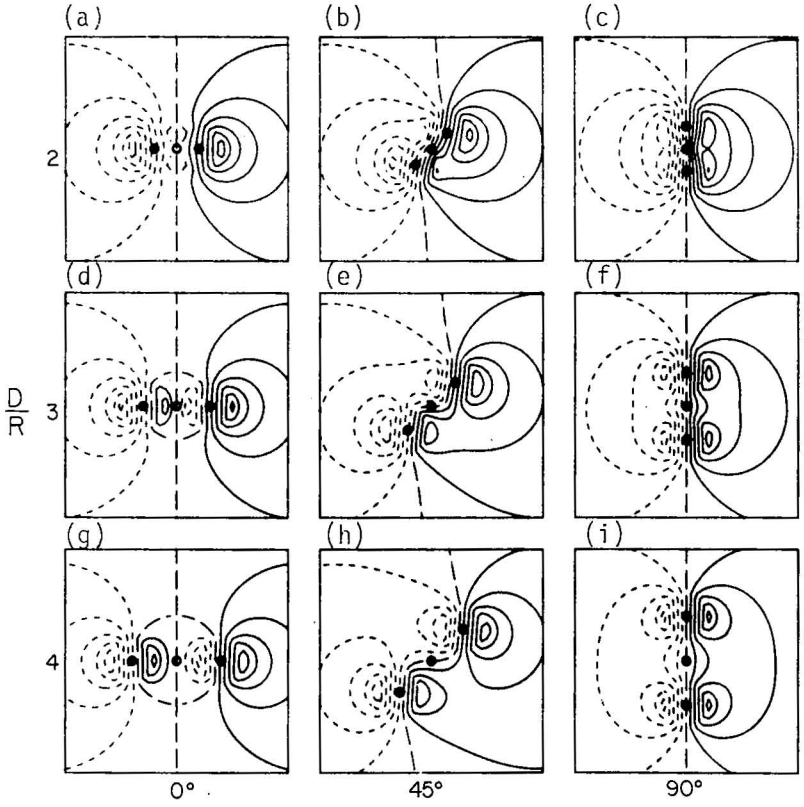

Fig. 3.4a-i Single Doppler velocity patterns for two identical circulations whose centers are separated by various distances (D divided by core radius R) for three different orientations. Radar is south of flow field.

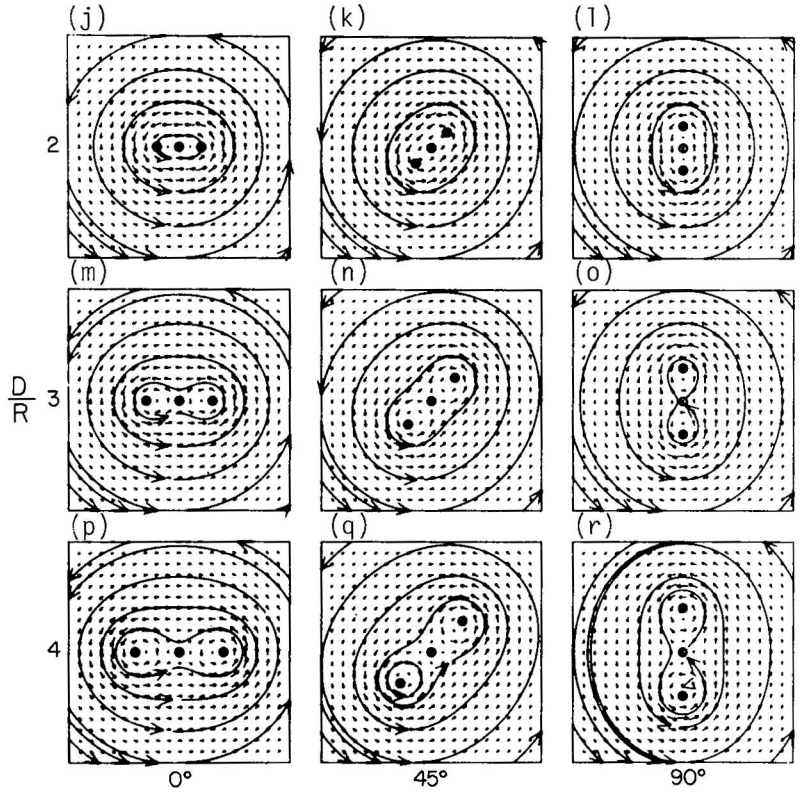

Fig. 3.4j-r Horizontal flow fields corresponding to the single Doppler velocity patterns in Figs. 3.4a-i.

3.5 Cyclonic-anticyclonic circulation centers having identical size and strength

Numerical simulations have revealed mirror-image anticyclonic (left-moving) and cyclonic (right-moving) storms in the presence of uni-directional environmental wind shear with height (e.g., Wilhelmson and Klemp, 1978; Schlesinger, 1978--whose results generally agree with Doppler observations of splitting thunderstorms). This subsection extends the discussion of the previous subsection by investigating the effect of separation distance and rotation of the axis between the mesocyclone and meso-anticyclone centers on the behavior of single Doppler velocity signatures.

Figures 3.5a-i illustrate the simulated single Doppler velocity signatures for the double vortex structure as the mesocyclone and meso-anticyclone centers are rotated by various amounts (0°, 45°, 90°) from the perpendicular position relative to the radar viewing direction. Values of separation distance (D) between these centers are normalized by the core radius (2,4,6). Corresponding airflow fields are shown in Figs. 3.5j-r.

At 0° rotation, the behavior of single Doppler velocity patterns changes as the distance varies from 2 to 4 to 6 (Figs. 3.5a,d,g). In the example of Fig. 3.5a, the Doppler velocity patterns are more densely packed between the meso-anticyclone and mesocyclone centers than they are outside. Since the two vortices rotate in opposite directions, the additive effect of flow toward the radar between the circulation centers accounts for the elongation of the Doppler velocity minima. As the separation distance increases, the elongated pattern splits into two distinguishable closed isodops (representing motion toward radar) on the inner edges of the separating vortices. At the same time, airflow between the centers of the vortex pair increases noticeably (Figs. 3.5j,m,p).

When the line connecting the vortex centers is rotated 45°, the Doppler velocity pattern is a function of vortex separation (Figs. 3.5b,e,h,k,n,q). For D/R=2, the pattern rotates only 20° to 25°. As the vortices move farther apart, the two characteristic vortex signatures become apparent and the overall elongation of central negative region becomes less pronounced.

When the radar viewing direction passes through the two rotation centers, the slightly distorted rotation signatures are evident (Figs. 3.5c,f,i) in the patterns of "four-leaf clover". As the vortices move apart, the only change is that the patterns approach those for pure rotation.

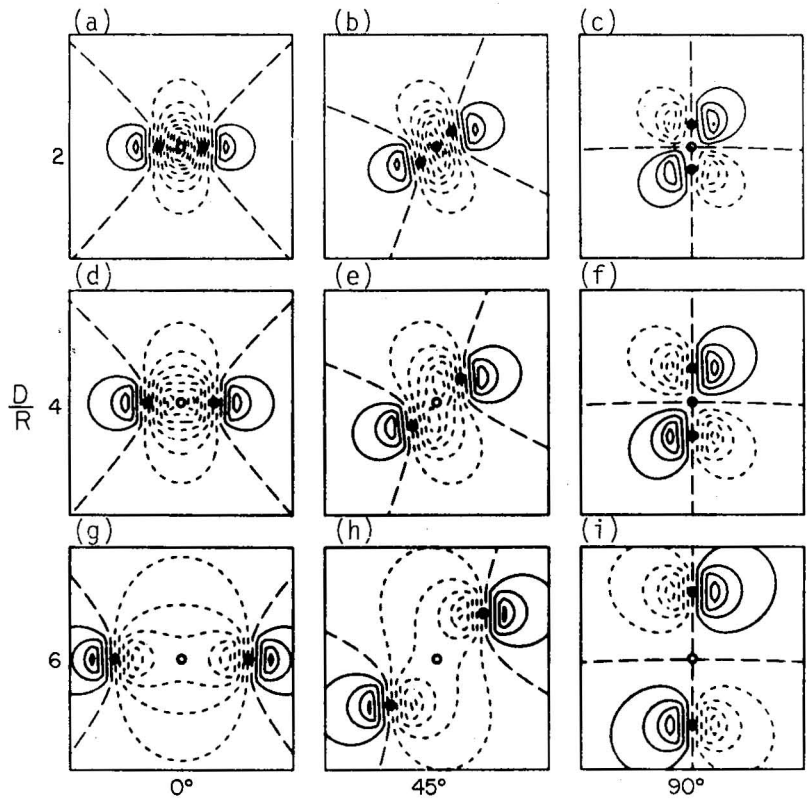

Fig. 3.5a-i Single Doppler velocity patterns for a cyclonic (upper or right)-anticyclonic (lower or left) couplet having the same size and strength. Rotation centers have various separation distances (D divided by core radius R) and orientations. Radar is south of flow field.

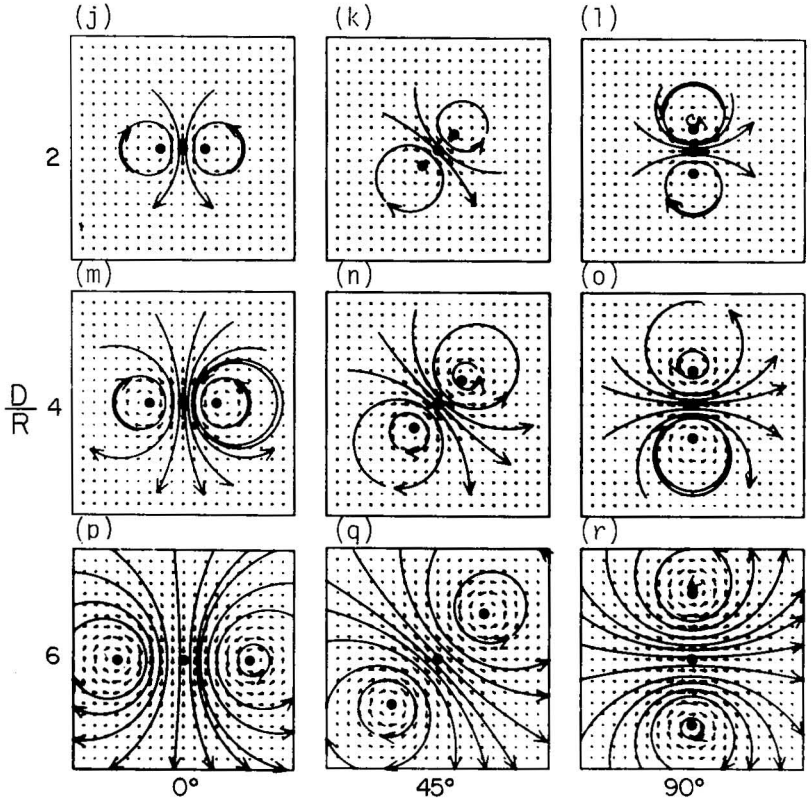

Fig. 3.5j-r Horizontal flow fields corresponding to the single Doppler velocity patterns in Figs. 3.5a-i.

3.6 Two divergence centers having identical size and strength

Single Doppler observations and satellite data have been used to study the structure and evolution of thunderstorm cloud top structures in relation to the occurrence of severe weather (tornadoes, hail and high wind) on the ground. Lemon and Burgess (1980) discuss divergence signatures measured near the top of the Fort Cobb, Oklahoma tornadic storm on 18 June 1973 and the Waurika, Oklahoma tornadic storm on 30 May 1976. Adler and Fenn (1979), using geosynchronous satellite data, estimated divergence magnitudes in the outflow through expansion rates of isotherms in the anvil of tornadic storms. Not much is known about pairs of divergence centers that occur near each other. In this subsection, we investigate what the corresponding single Doppler velocity signatures should be like.

Figures 3.6a-i show the results of simulations of two divergence signatures when orientation and separation distance are varied. The illustrations are selected examples of patterns that may occur near storm summits or in low-level downdraft outflow regions. Figures 3.6j-r illustrate wind flow vectors; superimposed streamlines correspond to those in Figs. 3.6a-i.

In Fig. 3.6a, two pure divergence signatures are oriented perpendicular to the radar beam. An important feature of the divergence signatures is an elongation of the closed isodops. As seen in Fig. 3.6j, the streamlines are diverging from a somewhat elongated source region. An increase in the distance between the centers of two divergence fields results in the formation of distinctive pairs of closed isodops for all orientations. As the divergence centers move apart, the horizontal flow fields (Figs. 3.6j-r) resemble air diverging from a line instead of a point.

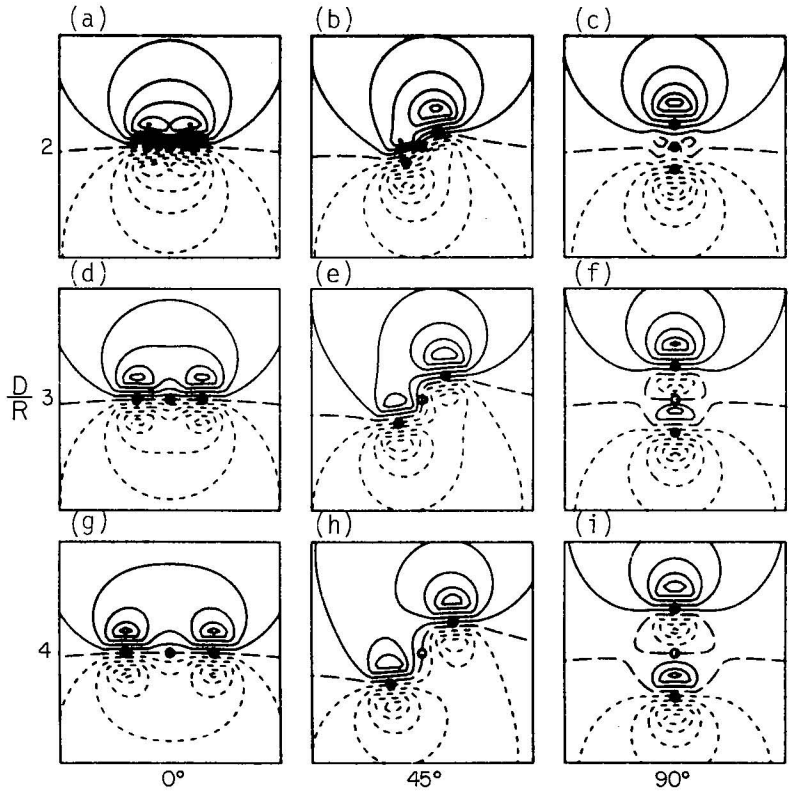

Fig. 3.6a-i Single Doppler velocity patterns for two identical divergence centers separated by various distances (D divided by core radius R) at three different orientations. Radar is south of flow field.

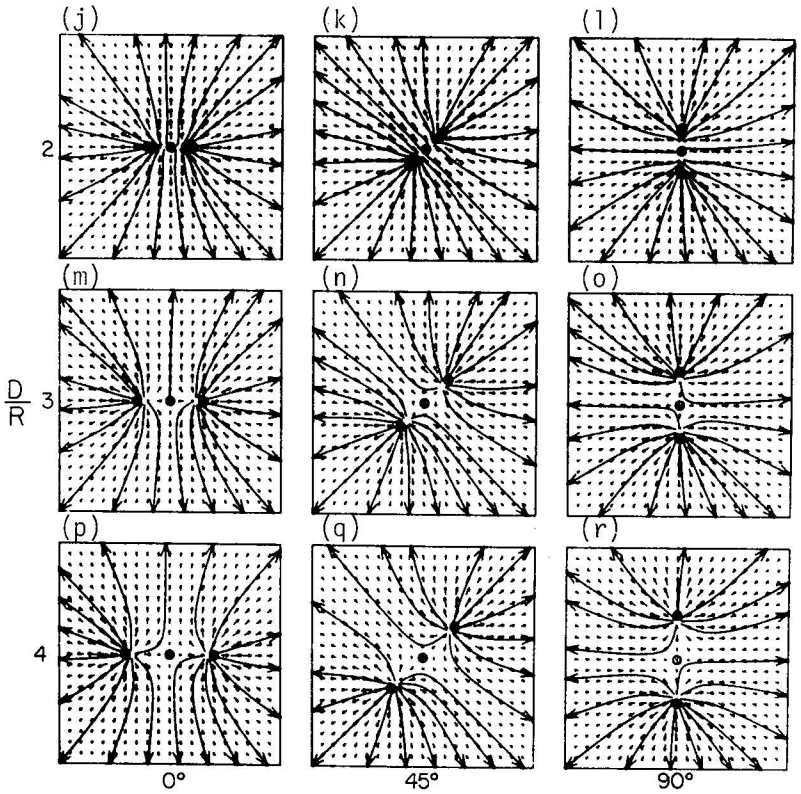

Fig. 3.6j-r Horizontal flow fields corresponding to the single Doppler velocity patterns in Figs. 3.6a-i.

3.7 Convergent cyclonic-divergent anticyclonic pair of vortices having identical size and strength

Near the ground in severe thunderstorms the basic flow features are a strongly convergent cyclone circulation and a weakly anticyclonic divergence area. The convergent mesocyclone is associated with the storm's updraft area, and the anticyclonic divergence region is caused by the storm's primary precipitation downdraft area located downwind of the updraft.

These circulations are simulated here with a pair of vortices that are the same size and have the same strength. Figures 3.7a-i show the simulated single Doppler signatures; corresponding flow patterns (wind vectors and streamlines) are shown in Figs. 3.7j-r. In Fig. 3.7h, the anticyclonically rotating downdraft is represented by the simulated single Doppler velocity pattern in the lower left; the pattern in the upper right represents the cyclonically rotating updraft, which is identical to Fig. 3.2e.

Looking at Fig. 3.7a, we note the closely packed, dashed isodops (motion toward radar) in the inner portion of the downdraft-updraft pair. Since the separation distance between the centers is twice the radii of the pair, the oppositely rotating circulations add to produce the elongated region of negative Doppler velocities. The same interpretation holds for the elongated region of positive velocities in Fig. 3.7c when the circulation angle is 90°

At angles of 0° and 90° the increasing separation distance causes the single Doppler velocity configurations to change considerably. The elongated pattern of Doppler velocity minima (maxima) splits into distinct closed isodops of velocity minima (maxima). They are illustrated in Figs. 3.7a,d,g and Figs. 3.7c,f,i. Corresponding streamline patterns are shown in Figs. 3.7j,m,p and Figs. 3.7 l,o,r.

At 45°, the "four-leaf clover" pattern divides into distinctive convergent cyclonic and divergent anticyclonic signatures as the separation distance increases (Figs. 3.7b,e,h). These patterns are somewhat similar to those of Figs. 3.5c,f,i.

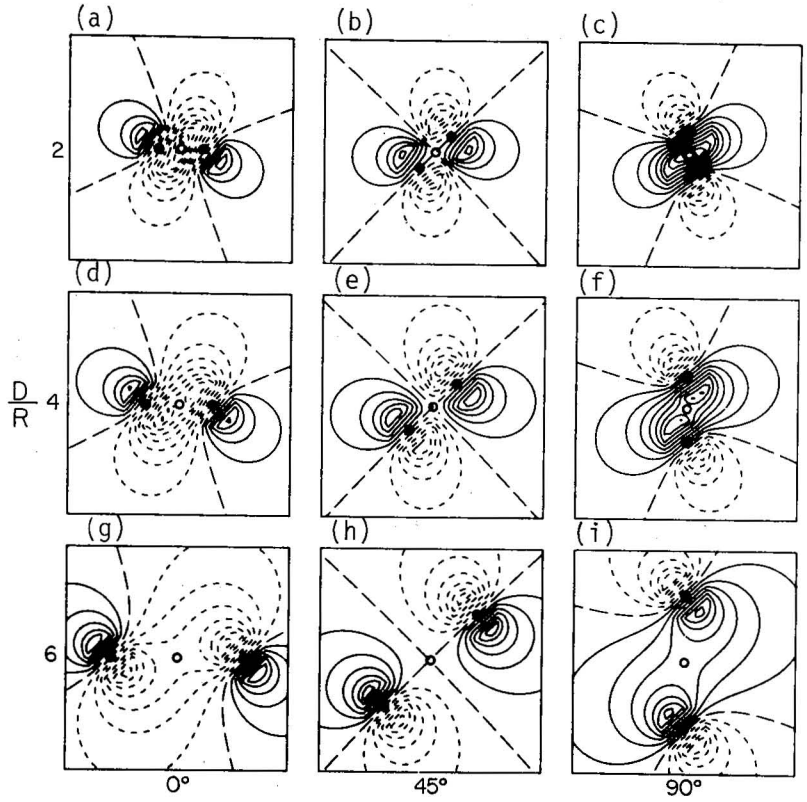

Fig. 3.7a-i Single Doppler velocity patterns for a convergent cyclonic (upper or right)-divergent anti-cyclonic (lower or left) pair of vortices having centers separated by various distances (D divided by core radius R) at various orientations. Radar is south of flow field.

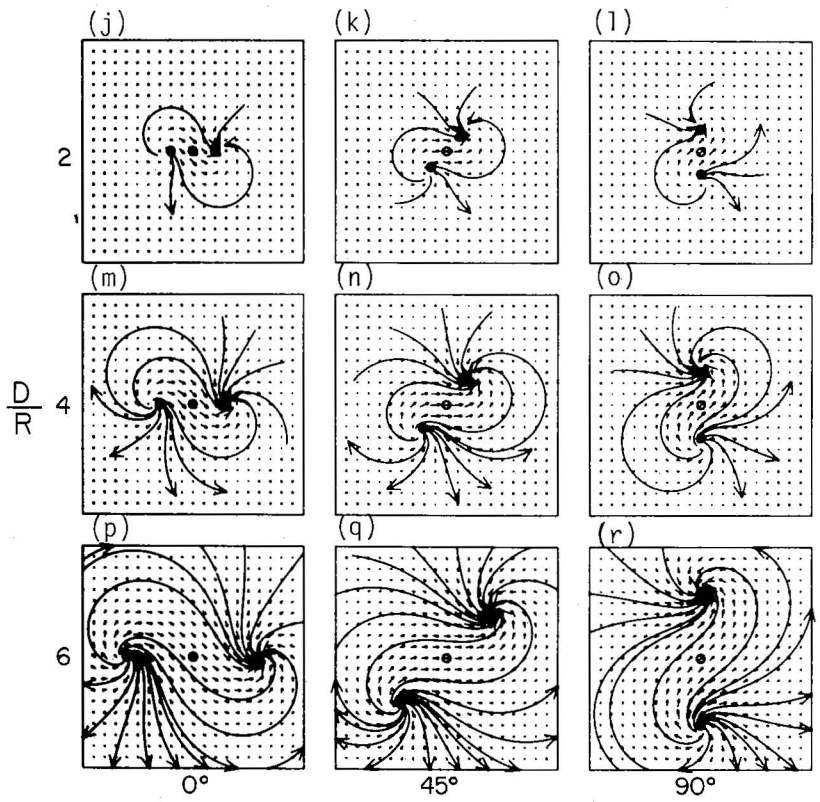

Fig. 3.7 j-r Horizontal flow fields corresponding to the single Doppler velocity patterns in Figs. 3.7a-i.

3.8 Nondivergent mesocirculation with embedded tornadic vortex signature

Burgess et al. (1975) and Brown et al. (1978) discussed important characteristics of the tornadic vortex signature (TVS). A TVS is a Doppler velocity signature of large shear--coincident with tornado location--characterized by velocity maxima of opposite signs occurring one beamwidth apart in an azimuthal direction; for the signature to be valid, the shear region must exhibit time and height continuity. Unfortunately, not all tornadoes produce identifiable signatures since TVS detection is a function of tornado size and strength as well as radar sampling volume and spatial density. In the case of the Union City, Oklahoma right-moving tornadic storm on 24 May 1973, the TVS originated at mid-level within a parent circulation. The TVS descended to the ground and extended up to at least 10 km, as its relative position migrated to the parent circulation center. The parent mesocyclone shrank before tornado touchdown. Minimum core diameter and maximum shear were reached at the time of largest visible tornado size. Finally, the TVS dissipated at all heights when the tornado dissipated.

The relationship between the mesocyclone core flow structure and TVS is poorly understood. Two possibilities are considered by Lemon et al. (1978); the tornado could act as the displaced (relative to velocity maxima) circulation center, or the closed tornadic circulation might have been embedded within the closed core circulation. Since the TVS did not rotate about the core center, the first possibility tends to be supported. However, the TVS initially may have developed as a second circulation center, but later strengthened and dominated the flow to the point that it became the mesocyclone center. In view of these possibilities, the core circulation relationship to TVS may be investigated further by using computer simulation. It is found that simple Doppler velocity patterns can be adequately simulated.

Combinations of Doppler velocity signatures are presented in Figs. 3.8a-aa. Closely spaced closed isodops of opposite signs represent the tornadic vortex signature (large shear in an azimuthal direction). The larger Doppler velocity signature--representing the parent nondivergent mesocyclone--is assumed to remain invariant in all portions of Fig. 3.8. The normalized separation distance (D/R) between the mesocyclone center and the TVS center is shown varying from 0 to 1/2 to 1. When the distance is zero, the TVS coincides with the mesocyclone center. For D/R equaling 1/2, the TVS is contained within the parent circulation core, halfway from the center to core radius. When the distance is one, the TVS is at the parent circulation's core radius where the peak tangential velocity occurs.

The peak tangential velocity for the TVS is varied from 1/2 to 1 to 2 times the mesocyclone's peak tangential velocity. When the ratio is 1/2, the presence of the TVS has minor impact on the mesocyclone signature. However, when the ratio is 2 or more, the TVS is the dominant feature in the Doppler velocity pattern. When the TVS and mesocyclone centers are not at the same azimuth (Figs. 3.8j-aa), the zero line moves toward the TVS center as the relative strength of the TVS increases.

In the three sets of Doppler velocity signatures (Figs. 3.8a-i, j-r and s-aa), the orientation of the centers varies from 0° to 45° to 90° in a clockwise manner relative to the radar viewing direction. In Figs. 3.8a, j and s (upper left corner), the presence of a weak TVS has secondary influence on the Doppler velocity pattern, regardless of the orientation between centers. However, when the TVS is strong (e.g., Figs. 3.8c,l,u), the Doppler velocity pattern changes with TVS position relative to the mesocyclone center.

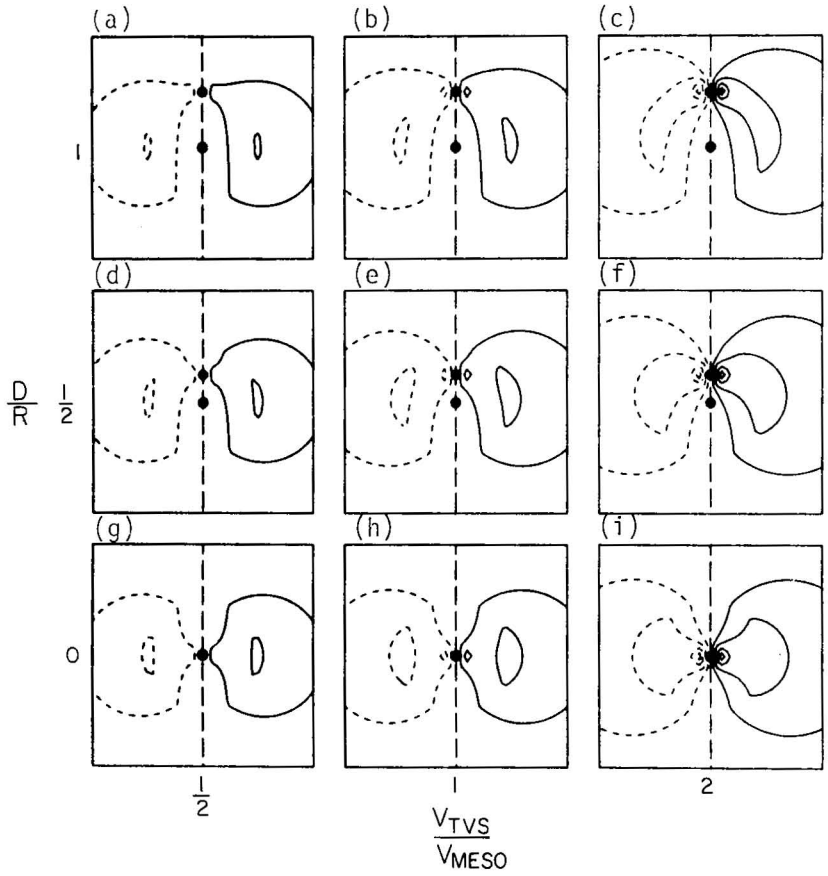

Fig. 3.8a-i Single Doppler velocity patterns for combinations of tornadic vortex and mesocyclone signatures having varying strengths (V_{TVS} relative to mesocyclone peak velocity V_{MESO}) and various separation distances (D relative to mesocyclone core radius R). Mesocyclone core radius is five times that of the TVS. Radar is south of flow field.

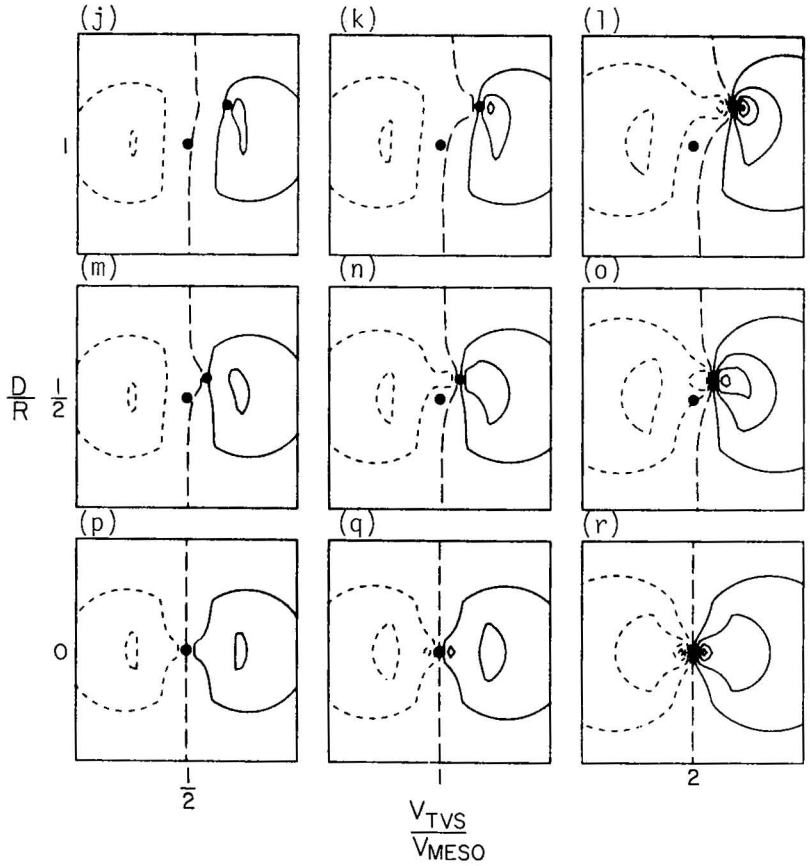

Fig. 3.8j-r Single Doppler velocity patterns as in Figs. 3.8a-i, except that the tornadic vortex signatures are oriented at a 45° angle (relative to the radar viewing direction) from the mesocyclone center. Radar is south of flow field.

The horizontal flow fields corresponding to the third set (Figs.3.8s-aa) are shown in Figs. 3.8bb-jj. Note that the overall flow patterns are similar when the two flow features are concentric (D/R=0). As the two centers move apart, the flow becomes increasingly elliptical; the circulation center moves from near the mesocyclone center toward the TVS center as the TVS becomes stronger.

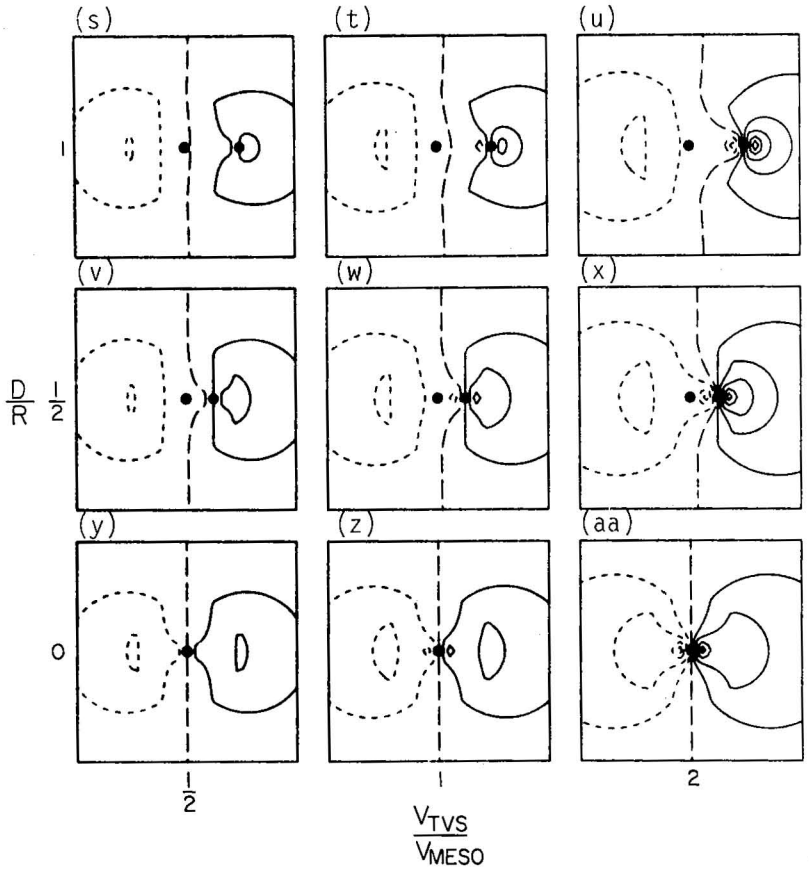

Fig. 3.8s-aa Single Doppler velocity patterns as in Figs. 3.8a-i and j-r, except that the tornadic vortex signatures are oriented at a 90° angle (relative to the radar viewing direction) from the mesocyclone center. Radar is south of flow field.

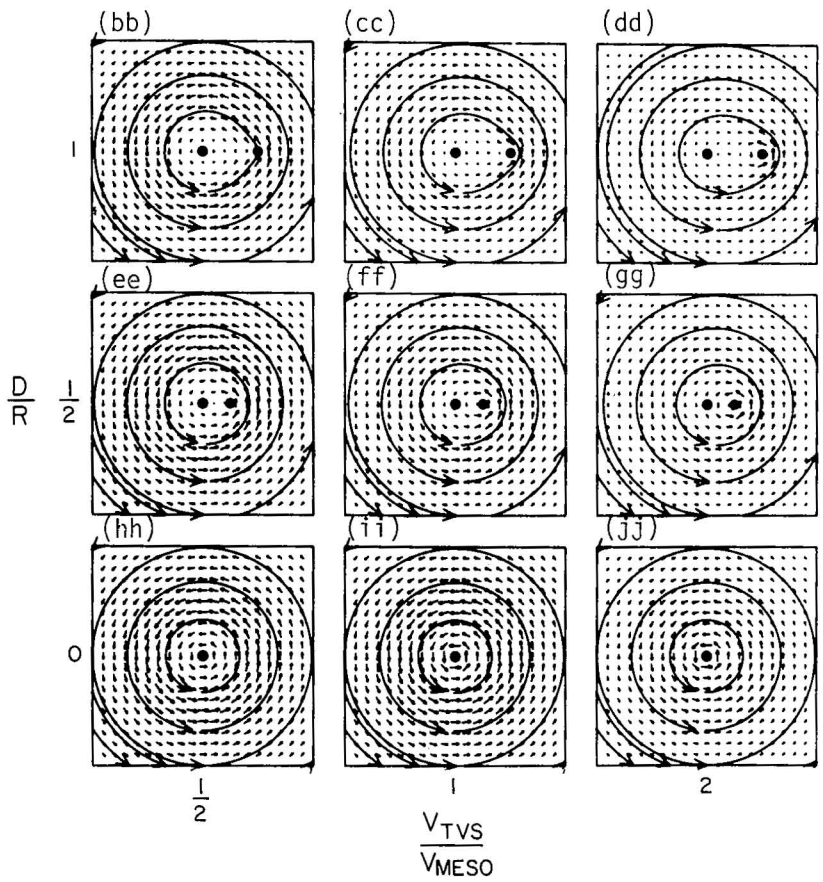

Fig. 3.8bb-jj Horizontal flow fields corresponding to the single Doppler velocity patterns in Figs. 3.8s-aa.

3.9 Convergent mesocirculation with embedded tornadic vortex signature

The previous subsection deals with a tornadic vortex signature (TVS) within a nondivergent mesoscale circulation--as would be found at midlevels within a tornadic storm. Here we discuss a TVS within a convergent mesocyclone, as would be found at low levels during the mature stage of a mesocyclone.

The convergent mesocyclone is simulated by adding pure convergence to pure rotation, both having the same core radius and peak velocity--as illustrated in Figs. 3.2e and i. A nondivergent TVS is added to the right of the mesocyclone center, relative to the radar viewing direction, as in Figs. 3.8s-jj. TVS peak velocity (V_{TVS}) varies from 1/2 to 2 times that of the convergent mesocyclone (V_{CM}); TVS position varies from the center to the edge of the mesocyclone's core region.

When V_{TVS} is one-half V_{CM}, the presence of the TVS has a minor impact on the overall single Doppler velocity pattern (Figs. 3.9a,d,g). However, the TVS--with its pronounced Doppler velocity shear--becomes the prominent feature when the TVS peak velocity is greater than or equal to the mesocyclone peak velocity. Note that the diagonal zero Doppler velocity line becomes parallel to the radar viewing direction as it passes through the nondivergent TVS.

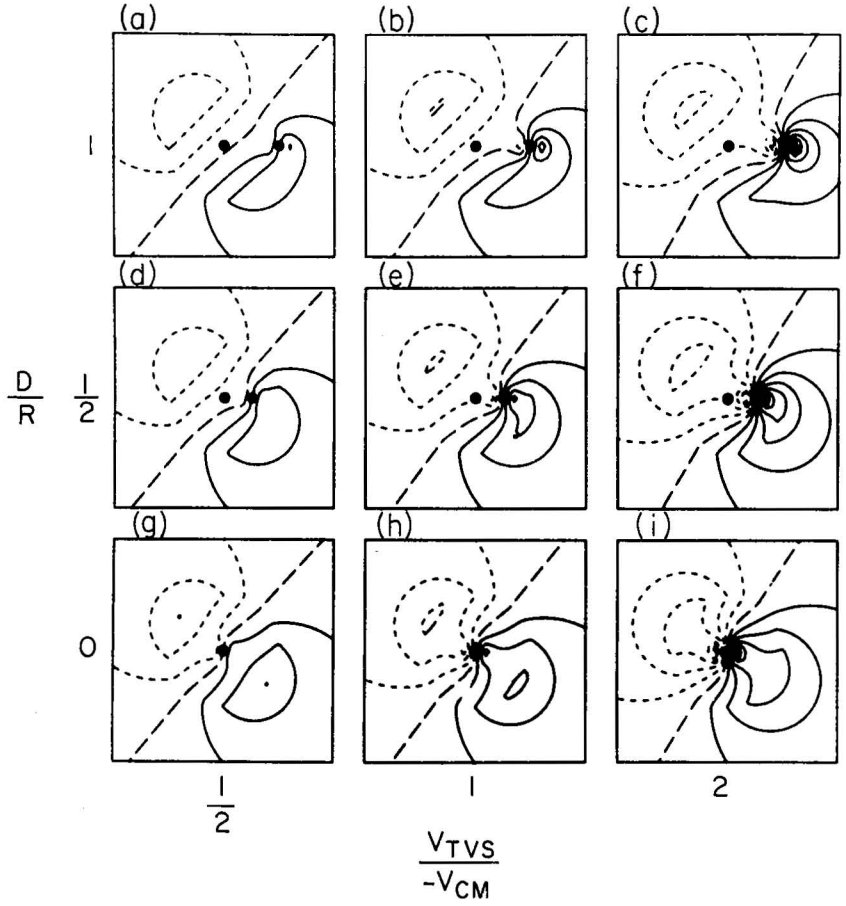

Fig. 3.9a-i Single Doppler velocity patterns for combinations of tornadic vortex and convergent mesocyclone signatures having varying strengths (V_{TVS} relative to mesocyclone peak velocity V_{CM}) and various separation distances (D relative to mesocyclone core radius R). Core radius of convergent mesocyclone is five times that of the TVS. Radar is south of flow field.

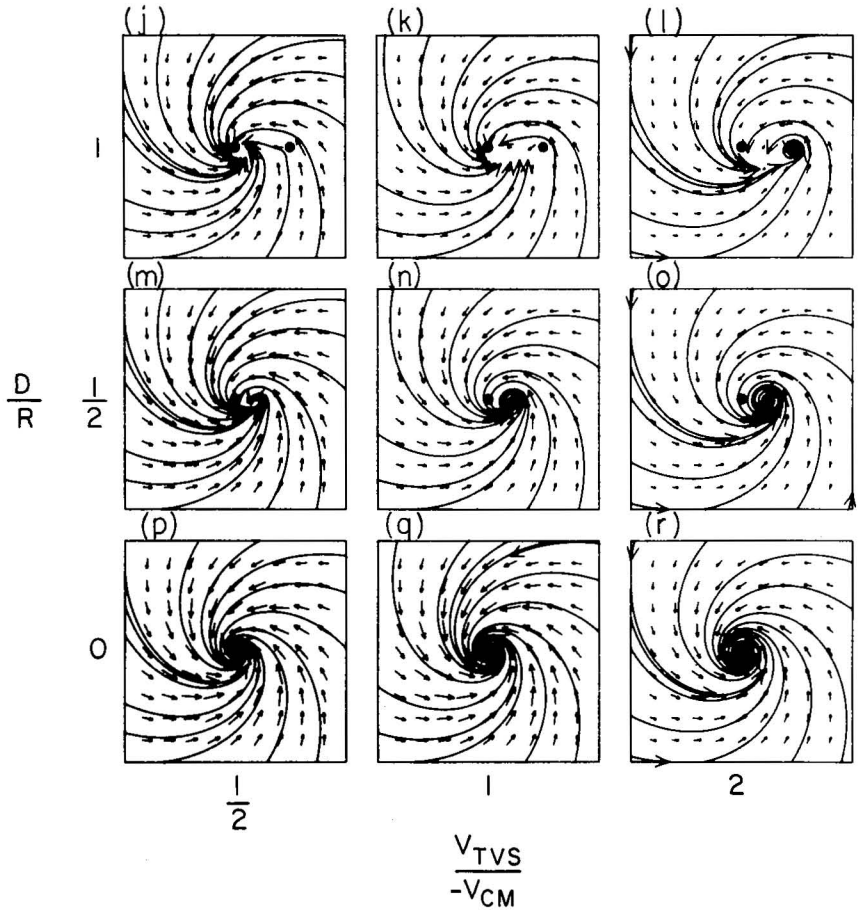

Fig. 3.9j-r Horizontal flow fields corresponding to the single Doppler velocity patterns in Figs. 3.9a-i.

3.10 Wake vortices behind an obstacle

Fluid dynamics experiments in the laboratory show that wake vortices form immediately downstream of a solid obstacle (e.g., Prandtl and Tietjens, 1934). In the atmosphere, similar flows have been found downstream of thunderstorm updrafts as revealed by aircraft (e.g., Fujita and Grandoso, 1968; Fankhauser, 1971) and Doppler radar measurements (e.g., Brown and Crawford, 1972; Toutenhoofd and Klemp, 1983).

In this subsection, we use a simple model to simulate the main features of vortices behind an obstacle. The model consists of a cyclonic-anticyclonic vortex pair and uniform environmental flow. The vortices have the same core radius and are located 2R apart. The environmental wind is oriented perpendicular to a line between the vortex centers and is equal in strength to twice the magnitude of the anticyclonic peak tangential velocity. As part of this investigation, orientation of the obstacle flow is varied and the strength of the cyclonic vortex (V_{t1}) is varied relative to the anticyclonic vortex (V_{t2}).

In Figs. 3.10a,d,g, the vortices have equal strength (opposite sign). The cyclonic vortex is on the right side of Fig. 3.10a and the anticyclonic vortex is on the left; the environmental wind is blowing toward the top of the page (away from the radar) so it exactly cancels the combined vortex flow midway between the vortices. When the Doppler radar is pointing in the direction of environmental wind flow (Fig. 3.10a), the Doppler velocity pattern is symmetric with the elongated pattern of minimum flow between the vortex centers and with maxima on the outer edges of the vortex cores.

When the flow field is rotated 45° relative to the radar viewing direction (Fig. 3.10d), the single Doppler velocity pattern rotates only about half that amount. Therefore, the Doppler velocity pattern for wake flow does not change much if the radar viewing direction is within 45° of the environmental wind. However, when the environmental wind is normal to the viewing direction--so that none of it is measured by the Doppler radar--the more classical wake flow breaks down into the "four-leaf clover" pattern that we have seen before when viewing a pair of vortices.

The center (Figs. 3.10b,e,h) and right columns (Figs. 3.10c,f,i) show the patterns when the cyclonic vortex is 2 and 3 times stronger than the anticyclonic vortex. As the mesocyclone becomes stronger, identification of its anticyclonic member becomes increasingly difficult. The corresponding horizontal flow fields (Figs. 3.10 j-r) are similar to those seen in the laboratory for stationary and rotating solid cylinders (e.g., Prandtl and Tietjens, 1934).

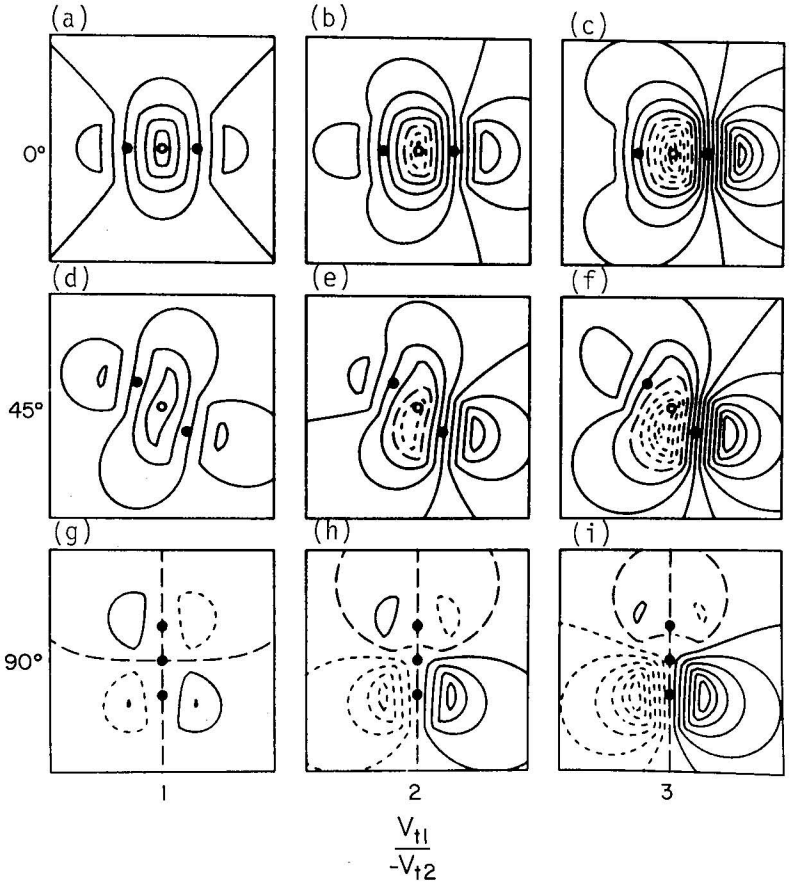

Fig. 3.10a-i Single Doppler velocity patterns for wake vortices behind an obstacle. Orientations and relative strengths of the counter-rotating centers (dark dots) are varied. Radar is south of flow field.

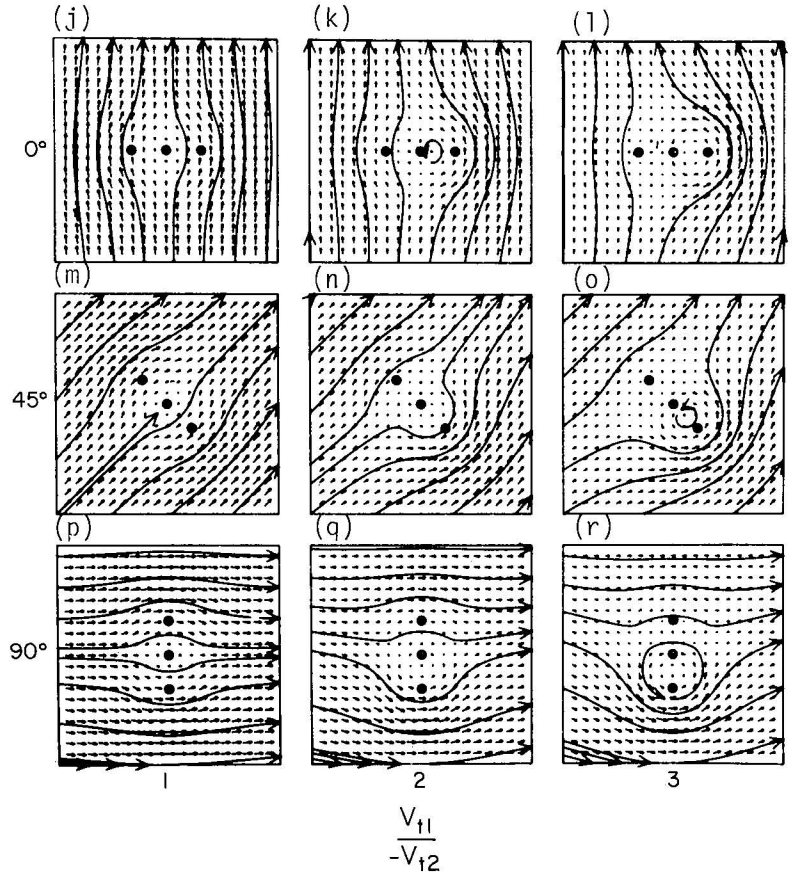

Fig. 3.10j-r Horizontal flow fields corresponding to the single Doppler velocity patterns in Figs. 3.10a-i.

3.11 Summary

In this section we have discussed a variety of single Doppler velocity signatures that can be found in severe thunderstorms. All of these signatures are composed of various combinations of three simple flow fields: uniform flow, divergence/convergence and rotation. Rankine combined velocity profiles were used to produce the divergence and rotation fields.

Samples of the single Doppler velocity patterns are reproduced here. They are presented in groups that should help to make "order out of the chaos" that the reader may have experienced while trying to assimilate the information in Figs. 3.2-3.10. When interpreting Fig. 3.11, the reader should remember that the Doppler radar is assumed to be positioned to the south (toward bottom of page), solid contours represent flow away from the radar (positive), short dashed contours represent flow toward the radar (negative) and long dashed lines represent zero Doppler velocity values. Single Doppler velocity patterns are on the left and corresponding horizontal flow fields are on the right.

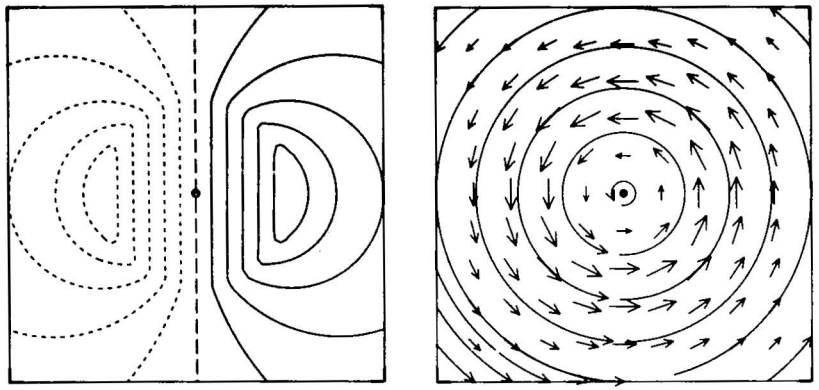

Fig. 3.11a Pure cyclonic rotation (vortex). The flow would be reversed for anticyclonic rotation.

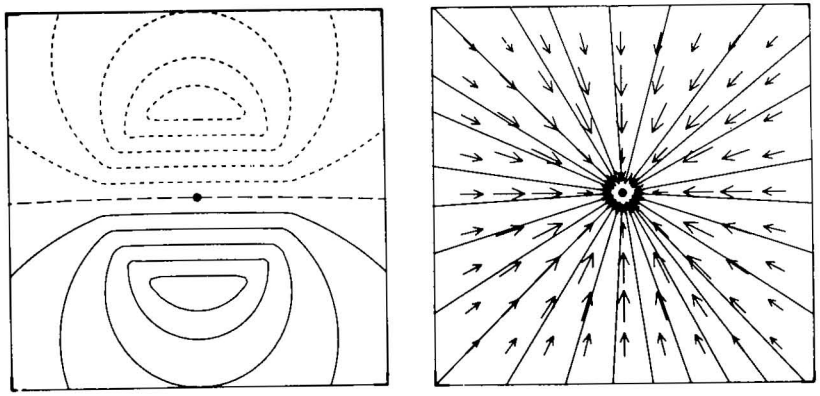

Fig. 3.11b Pure convergent flow. The direction of the flow would be reversed for divergent flow.

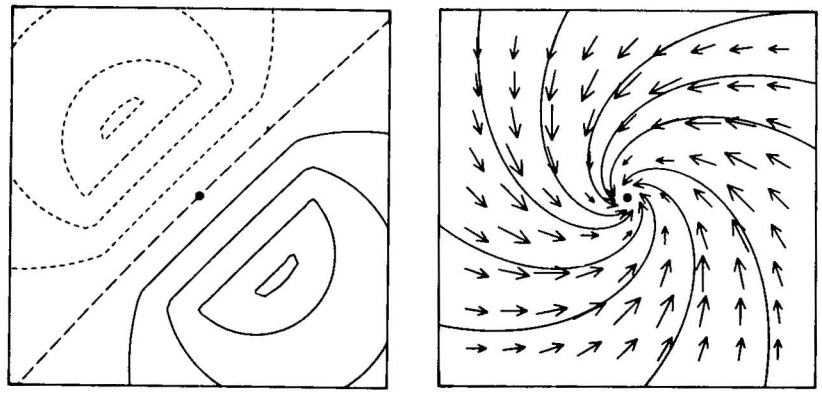

Fig. 3.11c Combination of cyclonic rotation (Fig. 3.11a) and convergent flow (Fig. 3.11b) where both features have same core radius and same peak velocity.

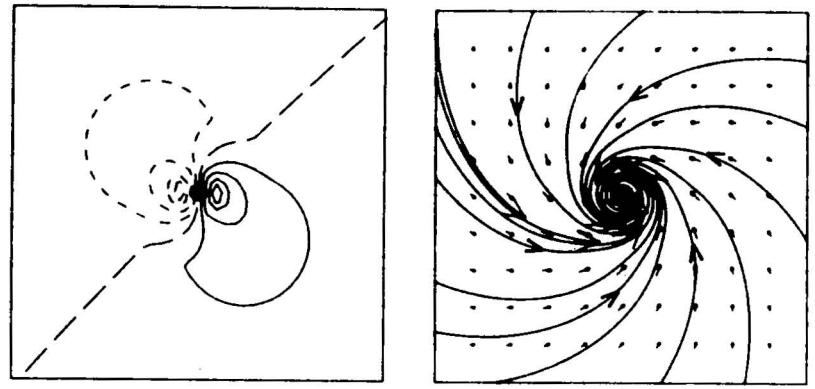

Fig. 3.11d Combination of small strong rotation and large weak convergence.

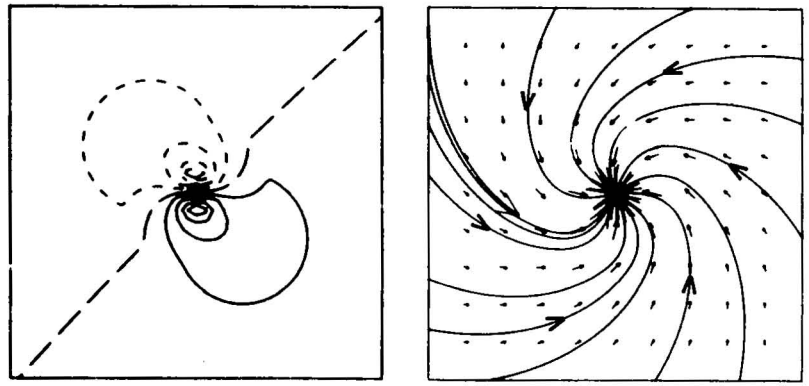

Fig. 3.11e Combination of large weak rotation and small strong convergence.

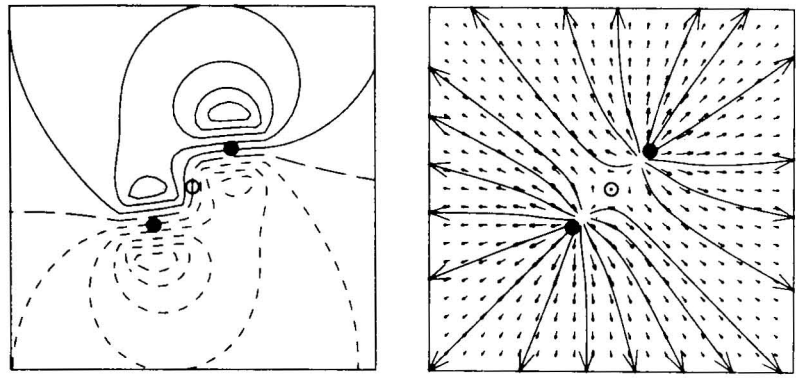

Fig. 3.11f Two divergence regions having same core radii and same peak radial velocities. Divergence centers are separated by three core radii and are oriented at a 45° angle to the Doppler radar viewing direction.

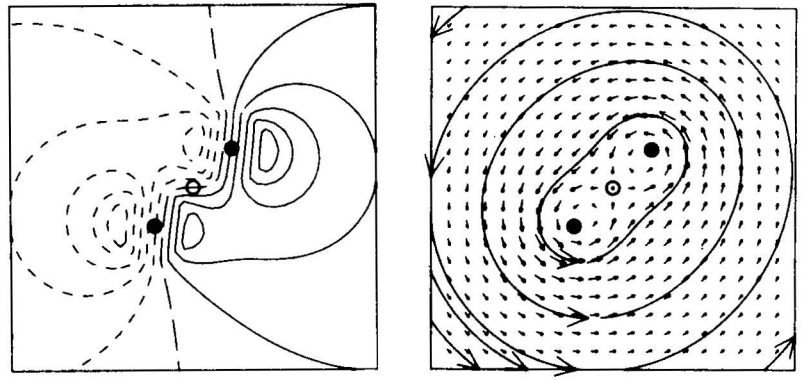

Fig. 3.11g Two cyclonic vortices having same core radii and same peak tangential velocities. Vortex centers are separated by three core radii and are oriented at a 45° angle to the Doppler radar viewing direction.

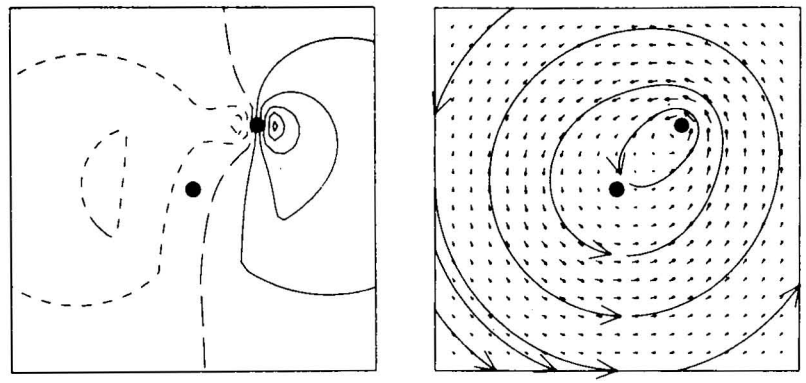

Fig. 3.11h Combination of a small strong vortex (tornadic vortex signature) and a large weaker vortex--representing a tornadic vortex signature at the edge of a mesocyclone core region. Relative to the radar viewing direction, the TVS is at a 45° angle from the mesocyclone center.

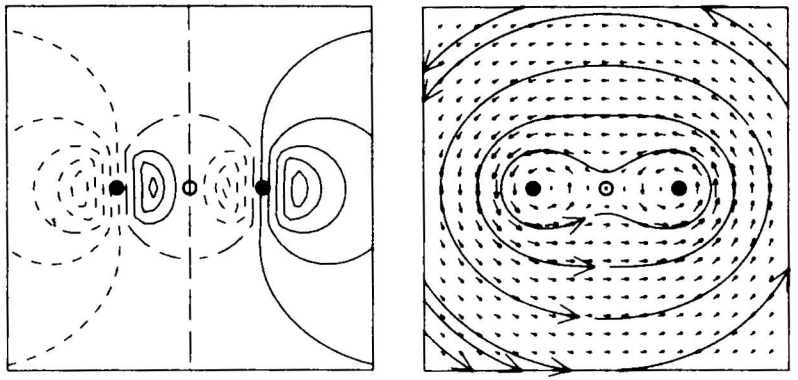

Fig. 3.11i Two cyclonic vortices having same core radii and same peak tangential velocities. Vortex centers are separated by four core radii and are oriented normal to the Doppler radar viewing direction.

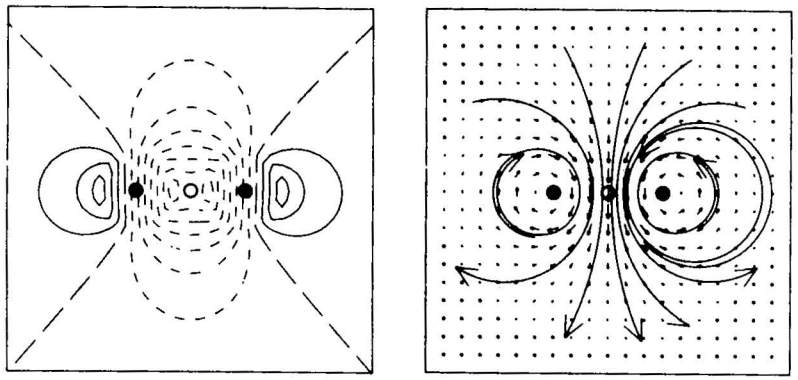

Fig. 3.11j Combination of a cyclonic (right) and anticyclonic (left) vortex having same core radii and same magnitudes of peak tangential velocities. Vortex centers are separated by four core radii and are oriented normal to the Doppler radar viewing direction.

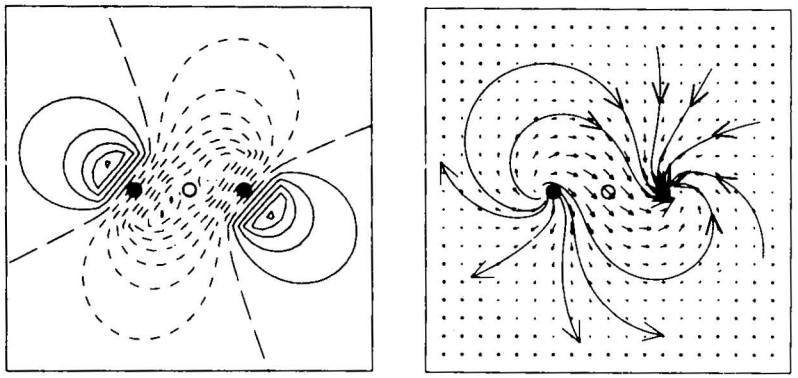

Fig. 3.11k Combination of a convergent, cyclonic vortex (right) and a divergent anticyclonic vortex (left) having same core radii and same magnitudes of peak velocities. Vortex centers are separated by four core radii and are oriented normal to the Doppler radar viewing direction.

Fig. 3.11 l Wake flow represented by a combination of environmental flow (equal to twice the magnitude of the peak tangential velocity) and a cyclonic (right) and anticyclonic (left) vortex having the same core radii and same magnitudes of peak tangential velocity. Vortex centers are separated by two core radii and are oriented at a 45° angle to the Doppler radar viewing direction.

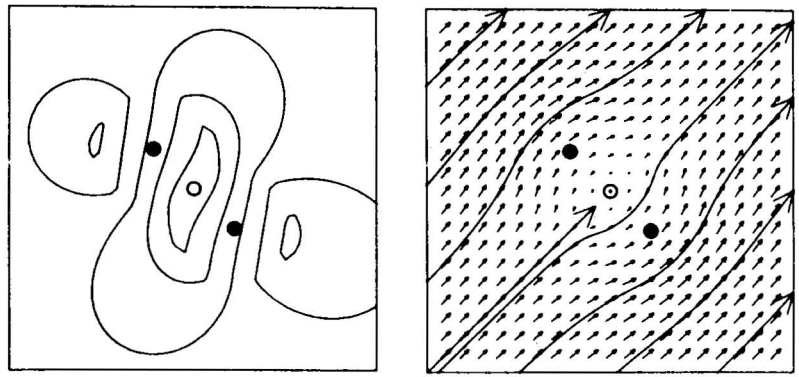

Fig. 3.11m Wake flow represented by a combination of environmental flow (equal to twice the magnitude of the anticyclone peak tangential velocity) and a cyclonic (right) and anticyclonic (left) vortex. The vortices have the same core radii but the magnitude of the peak tangential velocity of the cyclonic member is twice that of the anticyclonic vortex. Vortex centers are separated by two core radii and are oriented at a 45° angle to the Doppler radar viewing direction.

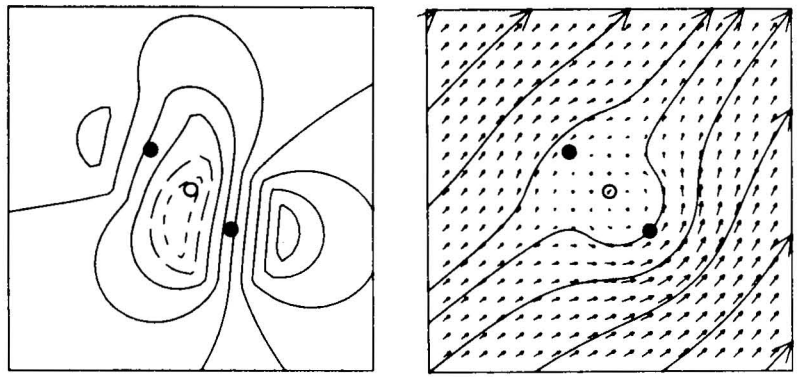

Fig. 3.11n Wake flow represented by a combination of environmental flow (equal to twice the magnitude of the anticyclone peak tangential velocity) and a cyclonic (right) and anticyclonic (left) vortex. The vortices have the same core radii but the magnitude of the peak tangential velocity of the cyclonic member is three times that of the anticyclonic vortex. Vortex centers are separated by two core radii and are oriented at a 45° angle to the Doppler radar viewing direction.

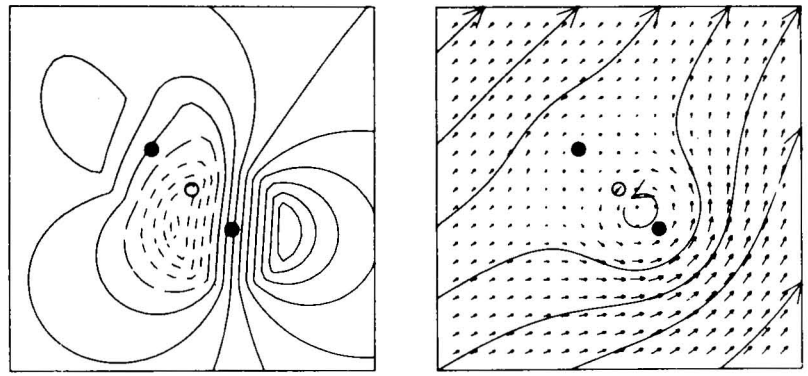

4. COMPARISONS OF SIMULATED DOPPLER VELOCITY FIELDS WITH OBSERVATIONS

Fascinated by the apparent simplicity of thunderstorm flow patterns, Brown and Crawford (1972) used a simple obstacle flow model to help interpret the first single Doppler velocity case study using an NSSL 10 cm Doppler radar. Continued use of simple models for rotation and divergence/convergence has aided in the interpretation and quantification of single Doppler mesocyclone and tornadic vortex signatures in thunderstorms (e.g., Brown et al., 1973; Burgess, 1976; Brown et al., 1978; Lemon et al., 1978; Wood et al., 1979; Burgess et al., 1982; Brown and Wood, 1983).

In this section, we use various combinations of the rotation, divergence/convergence and uniform flow models to simulate actual single Doppler velocity observations in clear air and within thunderstorms. As might be expected, the simulations do a good job in reproducing the basic features of the Doppler velocity fields, but they fail to reproduce smaller scale fluctuations.

4.1 The Ekman wind profile

The role of surface friction is related to the structure of the boundary layer. The fundamental character of the friction region, known as the Ekman layer, may be identified on the radar display. The Ekman layer equations derived by Pedlosky (1979) are given by

$$u = U[1 - \exp(-z/\delta_E)\cos(z/\delta_E)]$$
$$v = U \exp(-z/\delta_E)\sin(z/\delta_E) \quad , \tag{26}$$

where U is a horizontally uniform geostrophic flow above the Ekman layer, z the height, and δ_E the Ekman layer thickness. Velocities u and v approach the geostrophic velocity as z approaches infinity. Figure 4.1a displays the vertical profiles of the velocity components u and v; the hodograph of the Ekman spiral solution is shown in Fig. 4.1b. In the wind direction and speed boxes, the vertical profiles describe the variation of wind direction and speed in and above the Ekman layer and are given by

$$spd(h) = S[1-\exp(-2\pi h^*)\cos(2\pi h^*)] \quad 0 \le h \le H$$
$$dir(h) = 270°-\arctan\left[\frac{\exp(-2\pi h^*)\sin(2\pi h^*)}{1-\exp(-2\pi h^*)\cos(2\pi h^*)}\right] \quad , \tag{27}$$

where $h^* \equiv h/H$, for convenience. As h^* approaches unity, spd(h) approaches S and dir(h) approaches 270°. A characteristic feature of the Ekman layer is the gradual turning of the wind direction as $h^* \to 1$. The uniform flow U is assumed to blow from the west (270°). The layer, producing the radar display shown in Fig. 4.1d, features two wind maxima at midlevels which would be detected by the radar, one upwind and one downwind, as indicated by the two circled x's. Hatched shading denotes the excess of the maximum wind speed corresponding to the "nose" shape in the vertical profile of the wind speed in the wind speed box. Note that layer thickness δ_E is indicated by horizontal dashed lines in the wind direction and speed boxes and by shading in the radar display. In Fig. 4.1c, layer thickness is

$$\frac{Z}{\delta_E} = 1 = 2\pi h^*$$

or

$$h = 0.16H \quad .$$

Fig. 4.1 Ekman wind profile. (a) Vertical distribution of normalized u and v wind components; δ_E is Ekman layer thickness. (b) Hodograph of Ekman profile, where normalized height above ground is plotted along hodograph curve. (c) Wind speed and direction as a function of normalized height. (d) Single Doppler velocity pattern through the Ekman profile; Ekman layer thickness is stippled and "excess" wind speed is indicated by hatching.

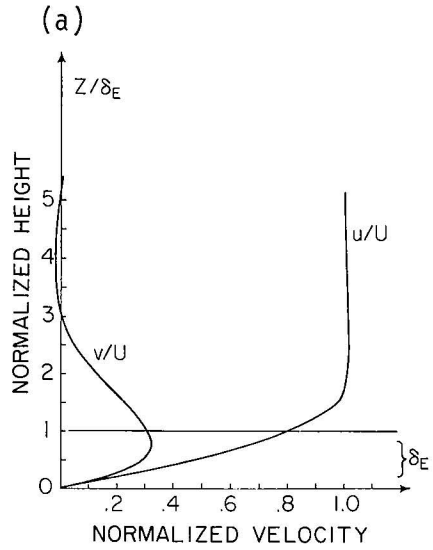
(a)
Z/δE
NORMALIZED HEIGHT
5
4
3
2
1
0
u/U
v/U
δE
.2
.4
.6
.8
1.0
NORMALIZED VELOCITY

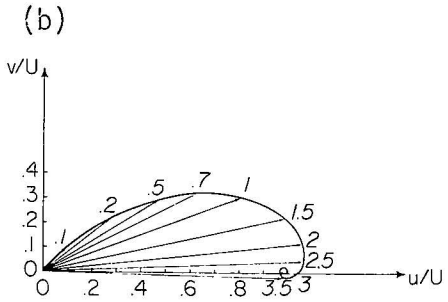
(b)
v/U
.4
.3
.2
.1
0
.1
.2
.5
.7
1
1.5
2
2.5
3
3.5
u/U
0
.2
.4
.6
.8

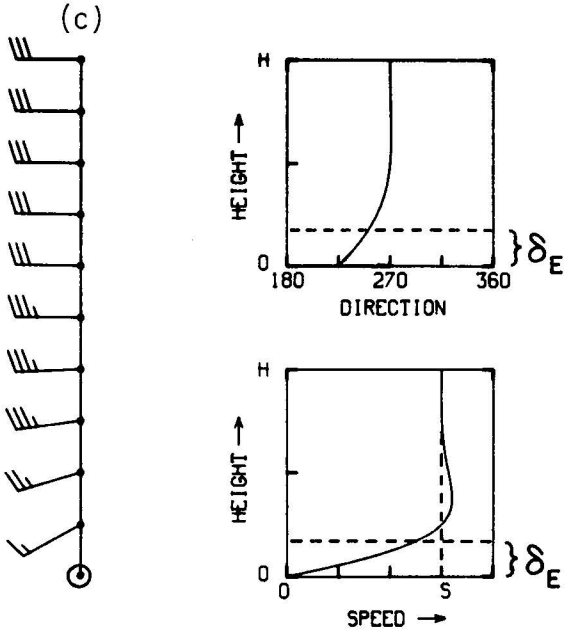
(c)
H
HEIGHT
0
180
270
360
DIRECTION
δE
H
HEIGHT
0
0
S
SPEED
δE

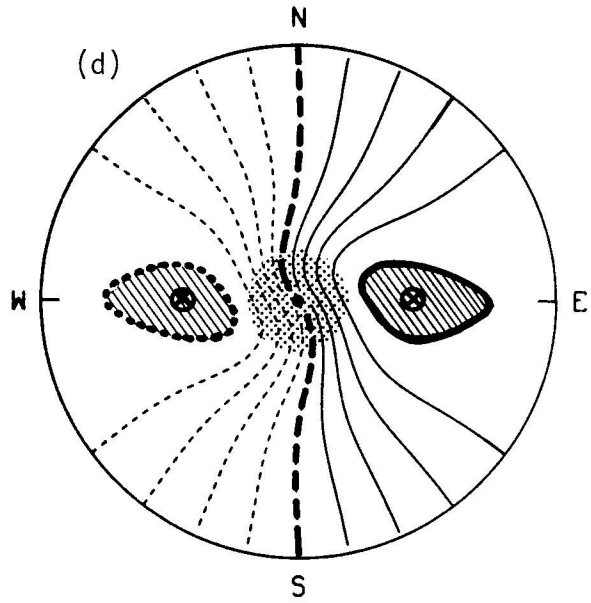
(d)
N
W
E
S

4.2 Stratiform precipitation on 7 February 1978

Baynton et al. (1977) and Wilson et al. (1980) have described how their color displays may be used to interpret data obtained from large-scale precipitation systems. Fig. 4.2a is adapted from Wilson's Fig. 3b, wherein color displays of single Doppler radial velocity patterns aid in the real-time interpretation of the wintertime stratiform precipitation. The data were collected at 0905 PST on 7 February 1978 near Sacramento, California. Closed contours representing upper-level and low-level jets are evident. The upper velocity maximum core slopes upward and toward the east-northeast, appearing at a greater slant range downwind than upwind; this is because the terrain slopes upward toward the Sierras to the east. The south-southeast direction of the low-level jet is, at least in part, the result of channeled winds parallel to the Sierra Nevada under stably stratified conditions, according to Wilson et al. (1980).

Another significant feature in Fig. 4.2a is an S-shaped zero Doppler velocity band as the mean wind veers with height from the lowest level to near the edge of the radar display. This band indicates strong warm advection through this layer. Near the edge of the display, winds backing with height indicate that cold air is being advected above the layer of warm air.

Fig. 4.2c shows the simulation of Fig. 4.2a using a mean vertical profile of horizontal winds (Fig. 4.2b). A least-squares fit to the wind profile results in the following expressions for wind speed and direction:

$$\mathrm{spd}(h) = S\left[0.25 + 12.37\left(\frac{h}{H}\right) - 96.95\left(\frac{h}{H}\right)^2 + 328.43\left(\frac{h}{H}\right)^3 - 529.52\left(\frac{h}{H}\right)^4 + 403.97\left(\frac{h}{H}\right)^5 - 117.71\left(\frac{h}{H}\right)^6\right]$$

$$0 \le h \le H \qquad (28)$$

$$\mathrm{dir}(h) = 149.6^\circ\left[1 - 2.4\left(\frac{h}{H}\right) + 36.4\left(\frac{h}{H}\right)^2 - 118.1\left(\frac{h}{H}\right)^3 + 170.6\left(\frac{h}{H}\right)^4 - 116.8\left(\frac{h}{H}\right)^5 + 30.9\left(\frac{h}{H}\right)^6\right]$$

where S is the maximum wind speed of 41 m s^{-1} and H = 6.7 km.

There is a striking similarity between the measured and simulated patterns in Figs. 4.2a and c. Some of the differences are due to the simplifying assumptions and to the lack of taking precipitation vertical velocities into account.

Fig. 4.2a Elevated Doppler velocity pattern measured at 0905 PST on 7 February 1978 near Sacramento, Calif. Stippled area is zero Doppler velocity band. Velocity extremes are measured at circled x's. After Wilson et al. (1980).

Fig. 4.2b Modeled wind speed and direction profiles based on Doppler derived winds (Wilson et al., 1980).

Fig. 4.2c Simulated Doppler velocity pattern based on Fig. 4.2b. Heavy dashed line is zero velocity contour. Solid contours are velocities away from radar, dashed contours are velocities toward radar. Velocity extremes are measured at circled x's.

(a)

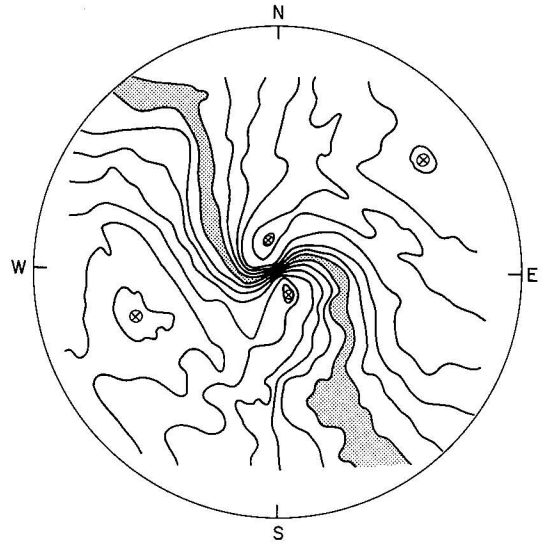

(b)

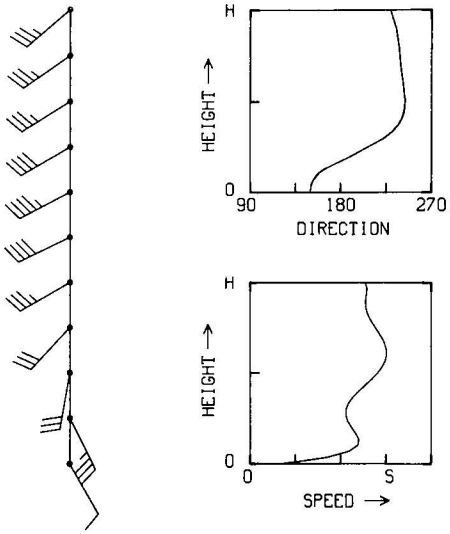

(c)

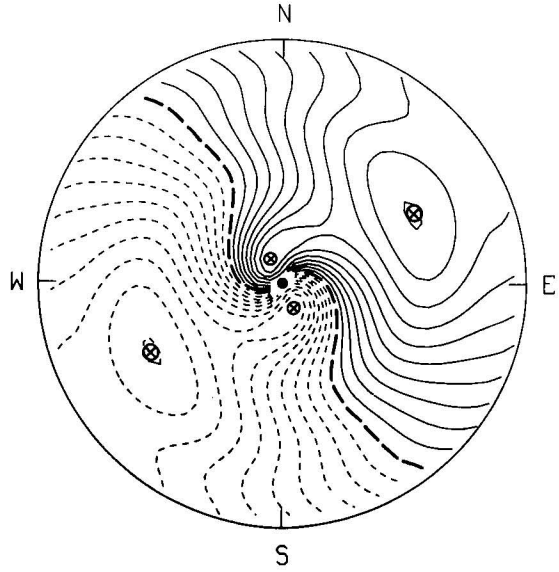

4.3 Divergence at the top of the Waurika, Oklahoma storm of 30 May 1976

On 30 May 1976 the Waurika, Oklahoma tornadic thunderstorm was observed with Doppler radar (Lemon and Burgess, 1980). The storm intensified, becoming a supercell by 1555 as indicated by Doppler radar data and began to split into left- and right-moving thunderstorms. The right-moving supercell storm produced large hail during its mature stage, and became tornadic during its collapsing phase. Storm motion during the severe stage was from 090° at 2.5 m s^{-1} in contrast to the mean environmental wind from 250° at 15 m s^{-1}.

At 1616 CST a strong divergent outflow near storm top was observed in the single Doppler divergence signature (Fig. 4.3a). The Norman Doppler radar is 145 km north of the signature center. The average of the Doppler velocity maxima (located near the closest and furthest edges of the radar echo) is 77 m s^{-1}. If one assumes that the peak values should be ±77 m s^{-1}, the measurements suggest that a Doppler velocity component of -11 m s^{-1}--representing the component of storm motion and environmental winds at the data level--has been added to the pure divergence signature. In addition, the divergence signature contains a small amount of anticyclonic rotation.

In order to produce a simulation of single Doppler divergence signature analogous to Fig. 4.3a, core diameter, representative peak Doppler velocity value, pattern rotation and mean environmental wind are determined. The mean peak value can be computed from the expression

$$\overline{V}_d = \frac{V_d(+) - V_d(-)}{2} \qquad (29)$$

where $V_d(+)$ is the more positive (less negative) peak value and $V_d(-)$ is the more negative (less positive) peak value. In this case, $V_d(+)$=66 m s^{-1} and $V_d(-)$=-88 m s^{-1} so that $\overline{V}_d$=77 m s^{-1}. The core diameter measured between the peak Doppler velocity values is 22 km. The radial and rotational (tangential) components of $\overline{V}_d$ can be determined by

$$V_r = \overline{V}_d \sin\theta \qquad (30)$$

$$V_t = \overline{V}_d \cos\theta \qquad (31)$$

where θ represents the amount of pattern rotation from the pure mesocyclone position shown in Fig. 3.1b; counterclockwise rotation is positive. Cyclonic circulation is a maximum when θ=0°; anticyclonic circulation reaches a peak when θ=180°; divergence reaches a maximum when θ=90°; convergence is a peak value when θ=270°. According to Fig. 4.3a, the amount of pattern rotation is 100° so that V_r=75.8 m s^{-1} and V_t=-13.4 m s^{-1}.

The parameters, including the mean environmental wind of 250° at 15 m s^{-1}, are shown in Fig. 4.3b. The resulting single Doppler divergence signature is shown in Fig. 4.3c. There is a striking overall resemblance between Figs. 4.3a and c. Differences between these figures may be attributed to some uncertainties in interpretation of Fig. 4.3a, possibly including some addition of particle fall velocities or vertical motion at large elevation angles in the single Doppler velocity data.

Fig. 4.3a Single Doppler divergence signature near the top of the Waurika, Okla. tornadic storm on 30 May 1976. The center of the divergence signature is 145 km at azimuth 190° from the Doppler radar at Norman, Okla.; however, the signature has been rotated so the radar will be beyond the bottom of the figure. Measured Doppler velocities (m s^{-1}) are positive for flow away from radar, negative for flow toward radar. After Lemon and Burgess (1980).

Fig. 4.3b Rotation (MESO), divergence (DIV) and uniform flow (ENV) parameters used to simulate the single Doppler velocity measurements in Fig. 4.3a.

Fig. 4.3c Simulation of single Doppler divergence signature as in Fig. 4.3a. Positive (negative) values of single Doppler velocities (m s^{-1}) are represented by solid (short dashed) contours. Zero Doppler velocity has a long dashed contour. Dark dot is the center of the divergence signature, taken to be coincident with the grid center.

(a)

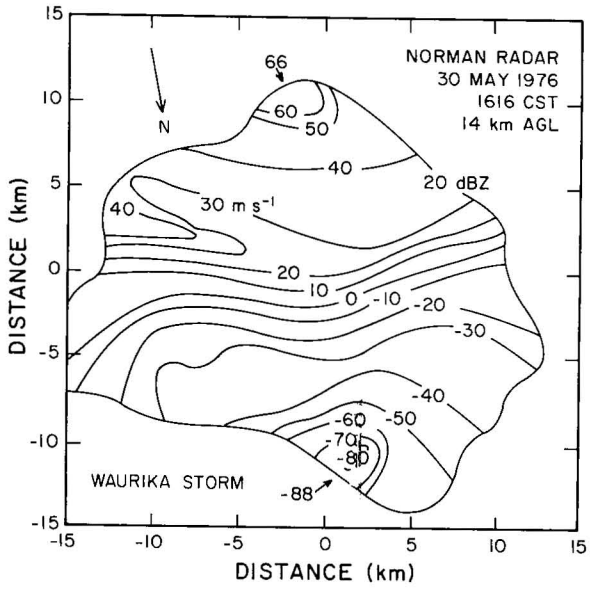

(b)

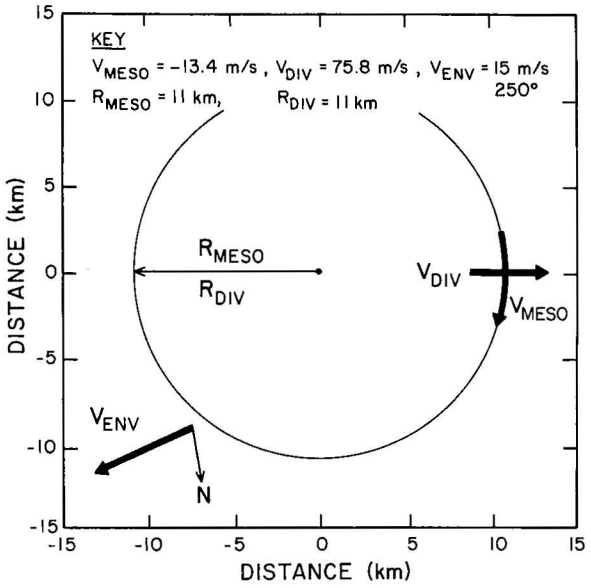

(c)

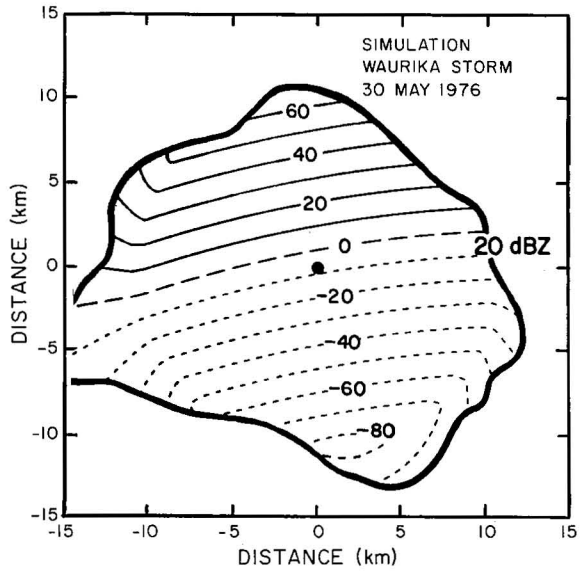

4.4 Mesocyclone and TVS in the Binger, Oklahoma storm of 22 May 1981

During the afternoon of 22 May 1981, a supercell storm produced five sequential tornadoes in central Oklahoma (see Lemon et al., 1982). The first echo of the storm was observed northeast of Childress, Texas, near the Oklahoma border around 1500 CST. After moving northeastward into west-central Oklahoma, the echo grew in intensity and became severe, producing 6.4 cm hail by 1720. The first of the five tornadoes touched down at about 1725 and the last one dissipated about 1935.

The largest and most violent of these tornadoes was the Binger, Oklahoma tornado. Because of its large size at a range of 60 to 80 km from the Norman Doppler radar, its tornadic vortex signature (TVS) was unusually strong. At 1909 (Fig. 4.4a), the TVS core diameter was about 1 km (one beamwidth) and the signature's velocity difference was 115 m s^{-1}; Doppler measurements typically overestimate tornado diameter and underestimate peak tornado rotational velocities (Brown et al., 1978).

The separate 20 m s^{-1} contour to the right of the TVS in Fig. 4.4a is interpreted to be the right side of the parent mesocyclone signature. Mesocyclone center is estimated to be 1 km to the right of the TVS center (Fig. 4.4b). The simulated Doppler velocity pattern (Fig. 4.4c) based on the parameters in Fig. 4.4b bears a very good overall approximation to the actual data--indicating that the model in Fig. 4.4b is realistic.

Fig. 4.4a Single Doppler velocity signature for the Binger, Okla. tornadic storm on 22 May 1981. The center of the mesocyclone signature is 70.8 km at azimuth 284.4° from the Norman Doppler radar; however, the signature has been rotated so the radar will be beyond the bottom of the figure. Measured Doppler velocities (m s^{-1}) are positive for flow away from radar, negative for flow toward radar. After Lemon et al. (1982).

Fig. 4.4b Mesocyclone and TVS parameters for simulating the single Doppler velocity measurements in Fig. 4.4a.

Fig. 4.4c Simulation of single Doppler TVS-mesocyclone signature as in Fig. 4.4a. Positive (negative) values of single Doppler velocities (m s^{-1}) are represented by solid (short dashed) contours. Contour increment of 10 m s^{-1} begins at zero Doppler velocity (long dashed contour). Dark dots indicate the centers of the mesocyclone signature and TVS.

(a)

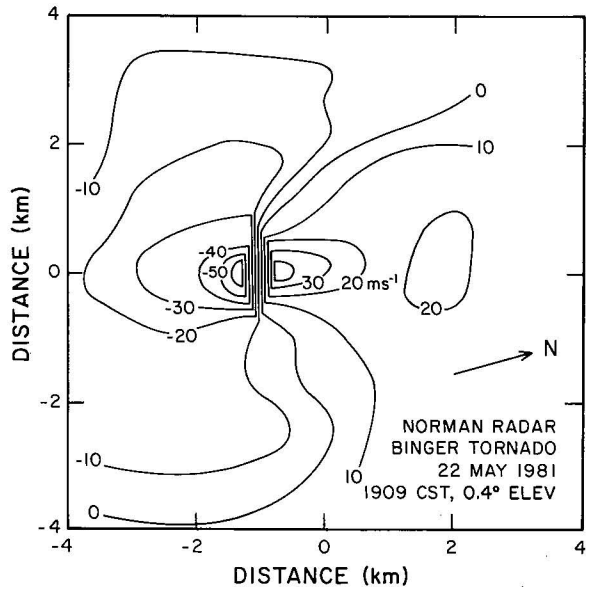

(b)

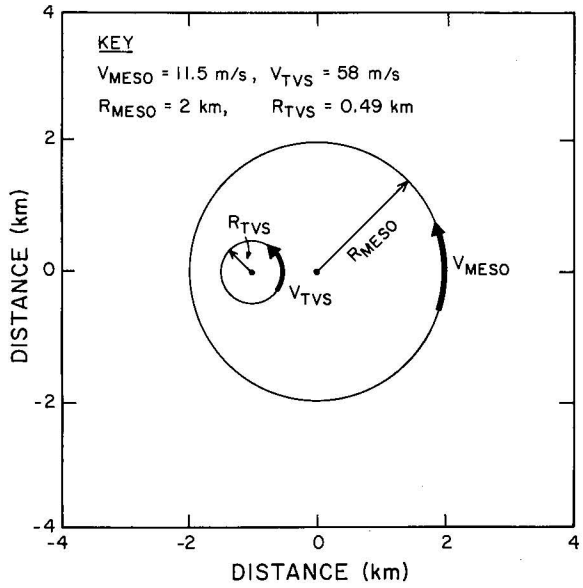

(c)

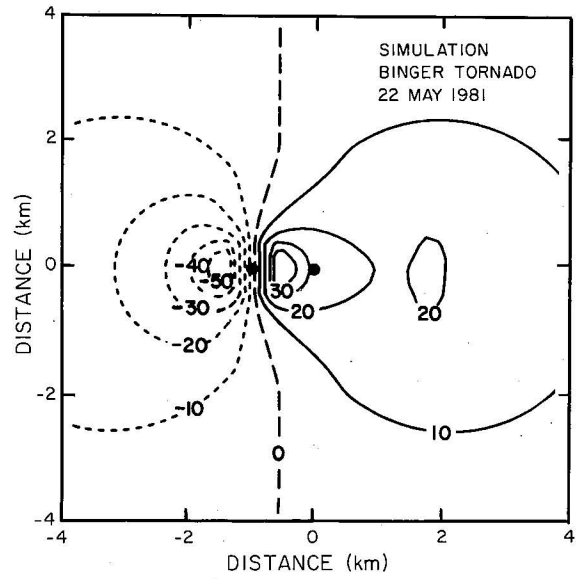

4.5 Convergent mesocyclone and TVS in the Fort Cobb, Oklahoma storm of 20 May 1977

During the afternoon and evening hours of 20 May 1977, sixteen tornadic storms occurred in western and central Oklahoma (Ray et al., 1981). The storm that produced the Fort Cobb tornado has been selected for comparison with a single Doppler velocity simulation. At 1643 CST, Fig. 4.5a (which is the same as Fig. 11a in Ray et al.) shows the single Doppler radial velocity components measured by the National Center for Atmospheric Research's (NCAR) CP-4 radar located at Hinton, Oklahoma. The center of the mesoscale circulation is 38.5 km at azimuth 192.8°, south-southwest of the CP-4 radar; note that Fig. 4.5a has been rotated so the radar will be beyond the bottom of the figure. At this time, the tornado was on the ground, as indicated by the stippled damage path in the figure. Figure 4.5a is interesting because the mesoscale circulation in which the tornado is embedded is strongly convergent at low levels. Although the exact position of the tornado at this time cannot be determined, it appears that the tornado is located roughly 0.9 km to the south of the parent circulation, as indicated by strong azimuthal gradients of single Doppler radial velocities across the tornado damage path.

Parameters used to simulate the single Doppler velocity measurements are displayed in Fig. 4.5b. The core radii of the parent mesocyclone's rotational and convergent components are assumed to be the same. It should be remembered that the TVS parameters are for the Doppler velocity signature of the tornado and do not represent the tornado itself (which is not directly measured because it is smaller than the radar beamwidth). The simulation (Fig. 4.5c) bears an overall resemblance to the actual data. We do not expect fine-scale features to be reproduced.

Fig. 4.5a Single Doppler signature for Fort Cobb tornado and parent mesocyclone on 20 May 1977. NCAR's CP-4 radar is located beyond bottom of figure. The center of the grid is also the mesocyclone center. Measured Doppler velocities (m s^{-1}) are positive for flow away from the radar, negative for flow toward the radar. After Ray et al. (1981).

Fig. 4.5b Parameters used to simulate the single Doppler velocity data in Fig. 4.5a.

Fig. 4.5c Simulation of parent circulation in which the TVS is embedded as in Fig. 4.5a. Solid (short dashed) contours represent positive (negative) values of single Doppler velocities (m s^{-1}). Contour increment of 5 m s^{-1} starts at the zero Doppler velocity (long dashed) contour. Dark dots refer to TVS and mesocyclone centers.

(a)

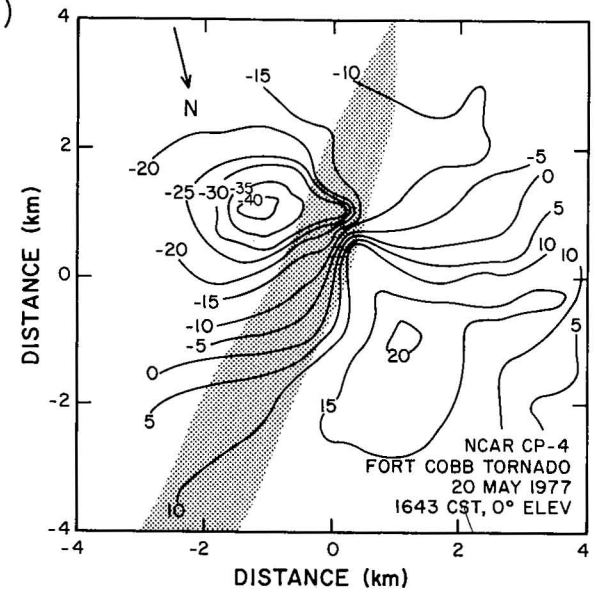

(b)

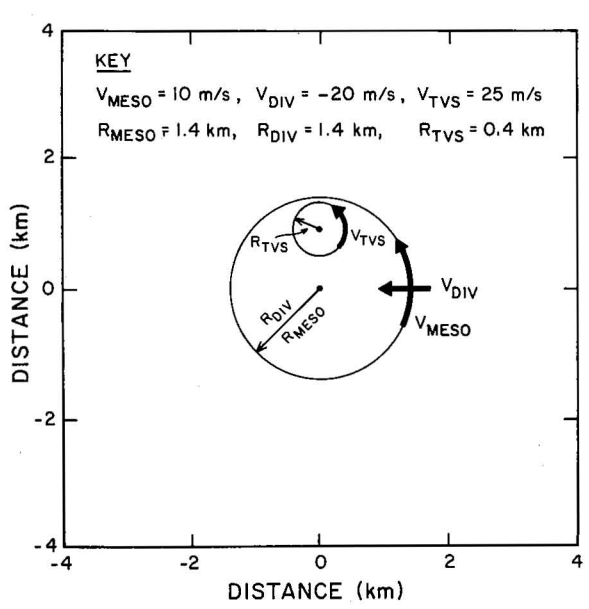

(c)

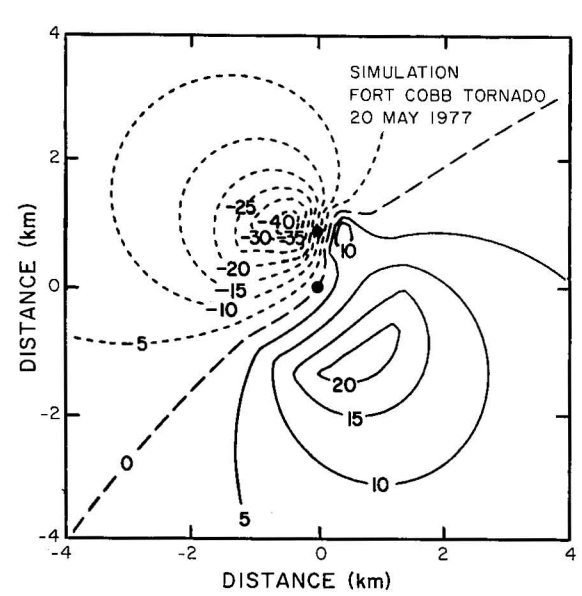

4.6 Wake vortices in the Agawam, Oklahoma storm of 6 June 1979

In the early afternoon on 6 June 1979, two adjacent small radar echoes appeared about 120 km southwest of the Norman Doppler radar. They separated as they moved northeastward and the right-most echo (looking in direction of storm motion) started curving toward the right after 1400 CST. As the right-moving Agawam hailstorm moved toward the radar, the signatures of wake vortices were very evident. The major updraft area along the storm's upwind edge evidently acted as the obstacle for the environmental flow.

Figure 4.6a shows the single Doppler velocity field at 1546 CST at a height of 4.5 km. All flow is toward the radar (at bottom of page) and the environmental wind at this level is 19 m s^{-1} toward the radar; Doppler velocities stronger than 16 m s^{-1} (toward radar) are stippled. Note that velocities greater than the environmental wind are in the outer portions of the echo, and a pronounced region of weak velocities is in the inner portion. A strong cyclonic vortex--qualifying as a mesocyclone--is evident in the upper left part of the echo.

Parameters used to simulate the wake flow region are shown in Fig. 4.6b. Four vortices and the observed environmental wind are used in the simulation. We found that, with a simulation this complex, we did not have the flexibility to reproduce each of the four vortices accurately. Apparently the difficulty was caused by adding a uniform environmental wind to the entire field.

The resulting Doppler velocity simulation is presented in Fig. 4.6c. Again, velocities toward the radar in excess of 16 m s^{-1} are stippled. In spite of the simulation difficulties, the overall pattern has been reproduced--as in all the other simulations.

Fig. 4.6a Doppler velocity measurements in the Agawam, Oklahoma hailstorm of 6 June 1979. All Doppler velocities are toward the radar, located 39 km below the grid center; contour interval is 4 m s^{-1}. Doppler velocities (toward radar) in excess of 16 m s^{-1} are stippled; the environmental wind is 19 m s^{-1}.

Fig. 4.6b Parameters for the four vortices and uniform environmental wind that were used to simulate Fig. 4.6a.

Fig. 4.6c Simulation of two pairs of wake vortices. Doppler velocities (toward radar) in excess of 16 m s^{-1} are stippled; contour interval is 4 m s^{-1}. Dark dots indicate vortex centers. Small open circle indicates grid center.

(a)

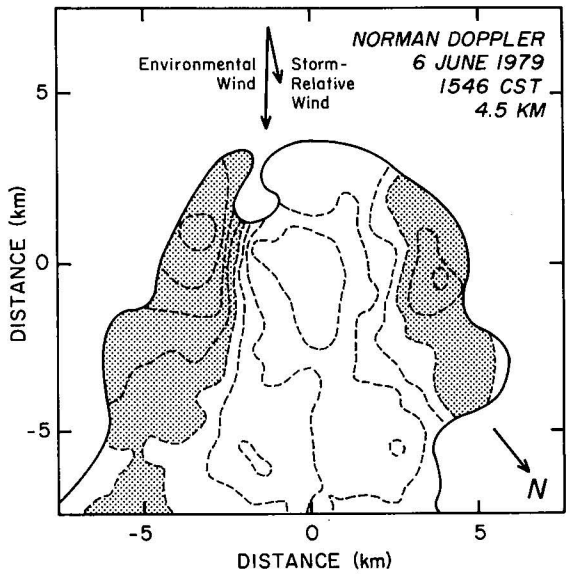

(b)

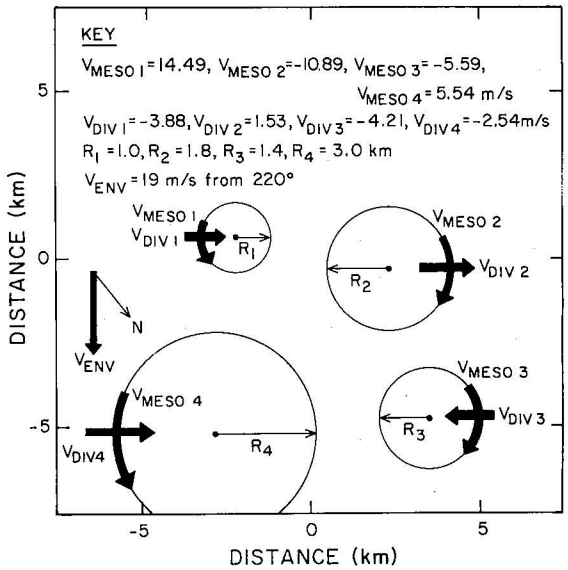

(c)

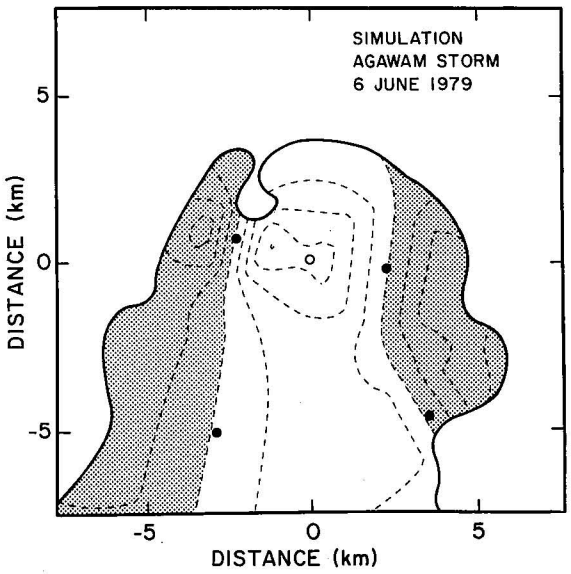

ACKNOWLEDGMENTS

Knowing that we have been using simulated Doppler velocities signatures for a number of years to interpret single Doppler radar measurements in severe storms, Dr. Peter Ray proposed that the simulations be organized into an atlas that could be used for training purposes. We liked the idea, so this atlas came into being. For completeness, we expanded it to include measurements in clear air that permit construction of a vertical profile of the environmental wind.

We appreciate the assistance of Michael Anderson and Louis Wicker in running the computer programs that produced the simulated flow fields. Joan Kimpel expertly drafted those figures that were not produced by computer. Photographic reduction of figures was efficiently performed by Robert Goldsmith. Sandra McPherson is to be commended for her perseverance in handling the various drafts of the manuscript.

This atlas was partially supported by NEXRAD Contract NA-82-SAC-00761 to the University of Oklahoma.

REFERENCES

Adler, R. F., and D. D. Fenn, 1979: Thunderstorm intensity as determined from satellite data. J. Appl. Meteor., 18, 502-517.

Armijo, L., 1969: A theory for the determination of wind and precipitation velocities with Doppler radar. J. Atmos. Sci., 26, 570-573.

Baynton, H. W., R. J. Serafin, C. L. Frush, G. R. Gray, P. V. Hobbs, R. A. Houze, Jr., and J. D. Locatelli, 1977: Real-time wind measurement in extratropical cyclones by means of Doppler radar. J. Appl. Meteor., 16, 1022-1028.

Bonewitz, J. D., 1981: The NEXRAD program--An overview. Preprints, 20th Conf. on Radar Meteor. (Boston), Boston, Amer. Meteor. Soc., 757-761.

Brown, R. A., and K. C. Crawford, 1972: Doppler radar evidence of severe storm high-reflectivity cores acting as obstacles to airflow. Preprints, 15th Radar Meteor. Conf. (Champaign-Urbana), Boston, Amer. Meteor. Soc., 16-21.

Brown, R. A., and V. T. Wood, 1983: Improved severe storm warnings using Doppler radar. Nat. Weather Digest, 8, in press.

Brown, R. A., D. W. Burgess and K. C. Crawford, 1973: Twin tornado cyclones within a severe thunderstorm: Single Doppler radar observations. Weatherwise, 26, 63-69,71.

Brown, R. A., L. R. Lemon and D. W. Burgess, 1978: Tornado detection by pulsed Doppler radar. Mon. Wea. Rev., 106, 29-38.

Burgess, D. W., 1976: Single Doppler radar vortex recognition: Part 1, Mesocyclone signatures. Preprints, 17th Conf. on Radar Meteor. (Seattle), Boston, Amer. Meteor. Soc., 97-103.

Burgess, D. W., L. R. Lemon and R. A. Brown, 1975: Tornado characteristics revealed by Doppler radar. Geophys. Res. Letters, 2, 183-184.

Burgess, D. W., V. T. Wood and R. A. Brown, 1982: Mesocyclone evolution statistics. Preprints, 12th Conf. on Severe Local Storms (San Antonio), Boston, Amer. Meteor. Soc., 422-424.

Donaldson, R. J., Jr., 1967: Horizontal wind measurement by Doppler radar in a severe squall line. Preprints, 5th Conf. on Severe Local Storms (St. Louis), Boston, Amer. Meteor. Soc., 89-98.

Fankhauser, J. C., 1971: Thunderstorm-environment interactions determined from aircraft and radar observations. Mon. Wea. Rev., 99, 171-192.

Fujita, T., and H. Grandoso, 1968: Split of a thunderstorm into anticyclonic and cyclonic storms and their motion as determined from numerical model experiments. J. Atmos. Sci., 25, 416-439.

Johannessen, K., and E. Kessler, 1976: Program to develop Doppler radar for use in the National Weather Service. Preprints, 17th Conf. on Radar Meteor. (Seattle), Boston, Amer. Meteor. Soc., 560-561.

Kraus, M. J., and R. J. Donaldson, Jr.,1976: Interpolation of PPI velocity displays in widespread storms. Preprints, 17th Conf. on Radar Meteor. (Seattle), Boston, Amer. Meteor. Soc., 239-243.

Lemon, L. R., and D. W. Burgess, 1980: Magnitude and implications of high speed outflow at severe storm summits. Preprints, 19th Conf. on Radar Meteor. (Miami), Boston, Amer. Meteor. Soc., 364-368.

Lemon, L. R., D. W. Burgess and R. A. Brown, 1978: Tornadic storm airflow and morphology derived from single-Doppler radar measurements. Mon. Wea. Rev., 106, 48-61.

Lemon, L. R., D. W. Burgess and L. D. Hennington, 1982: A tornado extending to extreme heights as revealed by Doppler radar. Preprints, 12th Conf. on Severe Local Storms (San Antonio), Boston, Amer. Meteor. Soc., 430-432.

Lemon, L. R., R. J. Donaldson, Jr., D. W. Burgess and R. A. Brown, 1977: Doppler radar application to severe thunderstorm study and potential real-time warning. Bull. Amer. Meteor. Soc., 58, 1187-1193.

Lhermitte, R. M., and D. Atlas, 1961: Precipitation motion by pulse Doppler radar. Preprints, 9th Weather Radar Conf. (Kansas City), Boston, Amer. Meteor. Soc., 218-223.

Peace, R. L., Jr., R. A. Brown and H. G. Camnitz, 1969: Horizontal motion field observations with a single pulse Doppler radar. J. Atmos. Sci., 26, 1096-1103.

Pedlosky, J., 1979: Geophysical Fluid Dynamics. New York, Springer-Verlag, 624 pp.

Prandtl, L., and O. G. Tietjens, 1934: Applied Hydro- and Aeromechanics. 1957 reprint, New York, Dover Publications, Inc., 311 pp.

Rabin, R. M., and R. J. Doviak, 1982: Prestorm observations in the clear air boundary layer with a Doppler radar. Preprints, 12th Conf. on Severe Local Storms (San Antonio), Boston, Amer. Meteor. Soc., 425-429.

Rankine, W. J. M., 1901: A Manual of Applied Mechanics, 16th edition. London, Charles Griff and Company, 574-578.

Ray, P. S., and K. Colbert, Editors, 1982: Proceedings of the NEXRAD Doppler Radar Symposium/ Workshop. Norman, Cooperative Institute for Mesoscale Meteorological Studies, 235 pp.

Ray, P. S., B. C. Johnson, K. W. Johnson, J. S. Bradberry, J. J. Stephens, K. K. Wagner, R. B. Wilhelmson and J. B. Klemp, 1981: The morphology of several tornadic storms on 20 May 1977. J. Atmos. Sci., 38, 1643-1663.

Schlesinger, R. E., 1978: A three-dimensional numerical model of an isolated thunderstorm: Part I. Comparative experiments for variable ambient wind shear. J. Atmos. Sci., 35, 690-713.

Staff, NSSL, AFGL, NWS and AWS, 1979: Final Report on the Joint Doppler Operational Project (JDOP), 1976-1978. NOAA Tech. Memo. ERL NSSL-86, Norman, Nat. Severe Storms Lab., 84 pp.

Toutenhoofd, V., and J. B. Klemp, 1983: An isolated cumulonimbus observed in northeastern Colorado: Comparison of field observations with results of a three-dimensional simulation. Mon. Wea. Rev., 111, 468-478.

Wilhelmson, R. B., and J. B. Klemp, 1978: A numerical study of storm splitting that leads to long-lived storms. J. Atmos. Sci., 35, 1974-1986.

Wilson, J., R. Carbone, H. Baynton and R. Serafin, 1980: Operational application of meteorological Doppler radar. Bull. Amer. Meteor. Soc., 61, 1154-1168.

Wood, V. T., D. W. Burgess and R. A. Brown, 1979: Single Doppler radar evolution of the Del City, OK tornado cyclone. Preprints, 11th Conf. on Severe Local Storms (Kansas City), Boston, Amer. Meteor. Soc., 545-548.

NATIONAL SEVERE STORMS LABORATORY

The NSSL Technical Memoranda, beginning at No. 28, continue the sequence established by the U.S. Weather Bureau National Severe Storms Project, Kansas City, Missouri. Numbers 1-22 were designated NSSP Reports. Numbers 23-27 were NSSL Reports, and 24-27 appeared as subseries of Weather Bureau Technical Notes. These reports are available from the National Technical Information Service, Operations Division, Springfield, Virginia 22151, a microfiche version for $4.00 or a hard copy, cost dependending upon the number of pages. NTIS numbers are given below in parenthesis.

No. 1 National Severe Storms Project Objectives and Basic Design. Staff, NSSP. March 1961. 16 p. (PB-168207)

No. 2 The Development of Aircraft Investigations of Squall Lines from 1956-1960. Brent B. Goddard. 34 p. (PB-168208)

No. 3 Instability Lines and Their Environments as Shown by Aircraft Soundings and Quasi-Horizontal Traverses. Dansey T. Williams. February 1962. 15 p. (PD-168209)

No. 4 On the Mechanics of the Tornado. J. R. Fulks. February 1962. 33 p. (PD-168210)

No. 5 A Summary of Field Operations and Data Collection by the National Severe Storms Project in Spring 1961. Jean T. Lee. March 1962. 47 p. (PB 165095)

No. 6 Index to the NSSP Surface Network. Tetsuya Fujita. April 1962. 32 p. (PB-168212)

No. 7 The Vertical Structure of Three Dry Lines as Revealed by Aircraft Traverses. E. L. McGuire. April 1962. 10 p. (PB-168213)

No. 8 Radar Observations of a Tornado Thunderstorm in Vertical Section. Ralph J. Donaldson, Jr. April 1962. 21 p. (PB-174859)

No. 9 Dynamics of Severe Convective Storms. Chester W. Newton. July 1962. 44 p. (PB-163319)

No. 10 Some Measured Characteristics of Severe Storms Turbulence. Roy Steiner and Richard H. Rhyne. July 1962. 17 p. (N62-16401)

No. 11 A Report of the Kinematic Properties of Certain Small-Scale Systems. Dansey T. Williams. October 1962. 22 p. (PB-168216)

No. 12 Analysis of the Severe Weather Factor in Automatic Control of Air Route Traffic. W. Boynton Beckwith. December 1962. 67 p. (PB-168217)

No. 13 500-Kc./Sec. Sferics Studies in Severe Storms. Douglas A. Kohl and John E. Miller. April 1963. 36 p. (PB-168218)

No. 14 Field Operations of the National Severe Storms Project in Spring 1962. L. D. Sanders. May 1963. 71 p. (PB-168219)

No. 15 Penetrations of Thunderstorms by an Aircraft Flying at Supersonic Speeds. G. P. Roys. Radar Photographs and Gust Loads in Three Storms of 1961 Rough Rider. Paul W. J. Schumacher. May 1963. 19 p. (PB-168220)

No. 16 Analysis of Selected Aircraft Data from NSSP Operations, 1962. Tetsuya Fujita. May 1963. 29 p. (PB-168221)

No. 17 Analysis Methods for Small-Scale Surface Network Data. Dansey T. Williams. August 1963. 20 p. (PB-168222)

No. 18 The Thunderstorm Wake of May 4, 1961. Dansey T. Williams. August 1963. 233 p. (PB-168223)

No. 19 Measurements by Aircraft of Condensed Water in Great Plains Thunderstorms. George P. Roys and Edwin Kessler. July 1966. 17 p. (PB-173048)

No. 20 Field Operations of the National Severe Storms Project in Spring 1963. J. T. Lee, L. D. Sanders, and D. T. Williams. January 1964. 68 p. (PB-168224)

No. 21 On the Motion and Predictability of Convective Systems as Related to the Upper Winds in a Case of Small Turning of Wind with Height. James C. Fankhauser. January 1964. 36 p. (PB 168225)

No. 22 Movement and Development Patterns of Convective Storms and Forecasting the Probability of Storm Passage at a Given Location. Chester W. Newton and James C. Fankhauser. January 1964. 53 p. (PB-168226)

No. 23 Purposes and Programs of the National Severe Storms Laboratory, Norman, Oklahoma. Edwin Kessler. December 1964. 17 p. (PB-166675)

No. 24 Papers on Weather Radar, Atmospheric Turbulence, Sferics and Data Processing. NSSL Staff. August 1965. 139 p. (AD-621586)

No. 25 A Comparison of Kinematically Computed Precipitation with Observed Convective Rainfall. James C. Fankhauser. September 1965. 28 p. (PB-168445)

No. 26 Probing Air Motion by Doppler Analysis of Radar Clear Air Returns. Roger M. Lhermitte. May 1966. 37 p. (PB-170636)

No. 27 Statistical Properties of Radar Echo Patterns and the Radar Echo Process. Larry Armijo. May 1966. The Role of the Kutta-Joukowski Force in Cloud Systems with Circulation. J. L. Goldman. May 1966. 34 p. (PB-170756)

No. 28 Movement and Predictability of Radar Echoes. James Warren Wilson. November 1966. 30 p. (PB-173972)

No. 29 Notes on Thunderstorm Motions, Heights, and Circulations. T. W. Harrold, W. T. Roach, and Kenneth E. Wilk. November 1966. 51 p. (AD-644899)

No. 30 Turbulence in Clear Air Near Thunderstorms. Anne Burns, Terence W. Harrold, Jack Burnham, and Clifford S. Spavins. December 1966. 20 p. (PB-173992)

No. 31 Study of a Left-Moving Thunderstorm of 23 April 1964. George R. Hammond. April 1967. 75 p. (PB-174681)

No. 32 Thunderstorm Circulations and Turbulence Studies from Aircraft and Radar Data. James C. Fankhauser and J. T. Lee. April 1967. 32 p. (PB-174860)

No. 33 On the Continuity of Water Substance. Edwin Kessler. April 1967. 125 p. (PB-175840)

No. 34 Note on Probing Balloon Motion by Doppler Radar. Robert M. Lhermitte. July 1967. 14 p. (PB-175930)

No. 35 A Theory for the Determination of Wind and Precipitation Velocities with Doppler Radars. Larry Armijo. August 1967. 20 p. (PB-176376)

No. 36 A Preliminary Evaluation of the F-100 Rough Rider Turbulence Measurement System. U. O. Lappe. October 1967. 25 p. (PB-177037)

No. 37 Preliminary Quantitative Analysis of Airborne Weather Radar. Lester P. Merritt. December 1967. 32 p. (PB-177188)

No. 38 On the Source of Thunderstorm Rotation. Stanley L. Barnes. March 1968. 28 p. (PB-178990)

No. 39 Thunderstorm-Environment Interactions Revealed by Chaff Trajectories in the Mid-Troposphere. James C. Fankhauser. June 1968. 14 p. (PB-179659)

No. 40 Objective Detection and Correction of Errors in Radiosonde Data. Rex L. Inman. June 1968. 50 p. (PB-180284)

No. 41 Structure and Movement of the Severe Thunderstorms of 3 April 1964 as Revealed from Radar and Surface Mesonetwork Data Analysis. Jess Charba and Yoshikazu Sasaki. October 1968. 47 p. (PB-183310)

No. 42 A Rainfall Rate Sensor. Brian E. Morgan. November 1968. 10 p. (PB-183979)

No. 43 Detection and Presentation of Severe Thunderstorms by Airborne and Ground-based Radars: A Comparative Study. K. E. Wilk, J. K. Carter, and J. T. Dooley. February 1969. 56 p. (PB-183572)

No. 44 A Study of a Severe Local Storm of 16 April 1967. George Thomas Haglund. May 1969. 54 p. (PB-184970)

No. 45 On the Relationship Between Horizontal Moisture Convergence and Convective Cloud Formation. Horace R. Hudson. March 1970. 29 p. (PB-191720)

No. 46 Severe Thunderstorm Radar Echo Motion and Related Weather Events Hazardous to Aviation Operations. Peter A. Barclay and Kenneth E. Wilk. June 1970. 63 p. (PB-192498)

No. 47 Evaluation of Roughness Lengths at the NSSL-WKY Meteorological Tower. Leslie D. Sanders and Allen H. Weber. August 1970. 24 p. (PB-194587)

No. 48 Behavior of Winds in the Lowest 1500 ft. in Central Oklahoma: June 1966 - May 1967. Kenneth C. Crawford and Horace R. Hudson. August 1970. 57 p. (N71-10615)

No. 49 Tornado Incidence Maps. Arnold Court. August 1970. 76 p. (COM-71-00019)

No. 50 The Meteorologically Instrumented WKY-TV Tower Facility. John K. Carter. September 1970. 18 p. (COM-71-00108)

No. 51 Papers on Operational Objective Analysis Schemes at the National Severe Storms Forecast Center. Rex L. Inman. November 1970. 91 p. (COM-71-00136)

No. 52 The Exploration of Certain Features of Tornado Dynamics Using a Laboratory Model. Neil B. Ward. November 1970. 22 p. (COM-71-00139)

No. 53 Rawinsonde Observation and Processing Techniques at the National Severe Storms Laboratory. Stanley L. Barnes, James H. Henderson and Robert J. Ketchum. April 1971. 245 p. (COM-71-00707)

NO. 54 Model of Precipitation and Vertical Air Currents. Edwin Kessler and William C. Bumgarner. June 1971. 93 p. (COM-71-00911)

No. 55 The NSSL Surface Network and Observations of Hazardous Wind Gusts. Operations Staff. June 1971. 20 p. (COM-71-00910)

No. 56 Pilot Chaff Project at NSSL. Edward A. Jessup. November 1971. 36 p. (COM-72-10106)

No. 57 Numerical Simulation of Convective Vortices. Robert P. Davies-Jones and Glenn T. Vickers. November 1971. 27 p. (COM-72-10269)

No. 58 The Thermal Structure of the Lowest Half Kilometer in Central Oklahoma: December 9, 1966 - May 31, 1967. R. Craig Goff and Horace R. Hudson. July 1972. 53 p. (COM-72-11281)

No. 59 Cloud-to-Ground Lightning Versus Radar Reflectivity in Oklahoma Thunderstorms. Gilbert D. Kinzer. September 1972. 24 p. (COM-73-10050)

No. 60 Simulated Real Time Displays of Doppler Radar Velocity Fields. G. B. Walker and L. D. Hennington. November 1972. 10 p. (COM-73-10515)

No. 61 Gravity Current Model Applied to Analysis of Squall-Line Gust Front. Jess Charba. November 1972. 58 p. (COM-73-10410)

No. 62 Mesoscale Objective Map Analysis Using Weighted Time-Series Observations. Stanley L. Barnes. March 1973. 60 p. (COM-73-10781)

No. 63 Observations of Severe Storms on 26 and 28 April 1971. Charles L. Vlcek. April 1973. 19 p. (COM-73-11200)

No. 64 Meteorological Radar Signal Intensity Estimation. Dale Sirmans and R. J. Doviak. September 1973. 80 p. (COM-73-11923/2AS)

No. 65 Radiosonde Altitude Measurement Using Double Radiotheodolite Techniques. Stephan P. Nelson. September 1973. 20 p. (COM-73-11932/9AS)

No. 66 The Motion and Morphology of the Dryline. Joseph T. Schaefer. September 1973. 81 p. (COM-74-10043)

No. 67 Radar Rainfall Pattern Optimizing Technique. Edward A. Brandes. March 1974. 16 p. (COM-74-10906/AS)

No. 68 The NSSL/WKY-TV Tower Data Collection Program: April-July 1972. R. Craig Goff and W. David Zittel. May 1974. 45 p. (COM-74-11334/AS)

No. 69 Papers on Oklahoma Thunderstorms, April 29-30, 1970. Stanley L. Barnes, Editor. May 1974. 147 p. (COM-74-11474/AS)

No. 70 Life Cycle of Florida Keys' Waterspouts. Joseph H. Golden. June 1974. 147 p. (COM-74-11477/AS)

No. 71 Interaction of Two Convective Scales Within a Severe Thunderstorm: A Case Study. and Thunderstorm Wake Vortex Structure and Aerodynamic Origin. Leslie R. Lemon. June 1974. 43 p. (COM-74-11642/AS)

NO. 72 Updraft Properties Deduced from Rawinsoundings. Robert P. Davies-Jones and James H. Henderson. October 1974. 117 p. (COM-75-10583/AS)

No. 73 Severe Rainstorm at Enid, Oklahoma - October 10, 1973. L. P. Merritt, K. E. Wilk, and M. L. Weible. November 1974. 50 p. (COM-75-10583/AS)

No. 74 Mesonetwork Array: Its Effect on Thunderstorm Flow Resolution. Stanley L. Barnes. October 1974. 16 p. (COM-75-10248/AS)

No. 75 Thunderstorm-Outflow Kinematics and Dynamics. R. Craig Goff. December 1975. 63 p. (PB-250808/AS)

No. 76 An Analysis of Weather Spectra Variance in a Tornadic Storm. Philippe Waldteufel. May 1976. 80 p. (PB-258456/AS)

No. 77 Normalized Indices of Destruction and Deaths by Tornadoes. Edwin Kessler and J. T. Lee. June 1976. 47 p. (PB-260923/AS)

No. 78 Objectives and Accomplishments of the NSSL 1975 Spring Program. K. Wilk, K. Gray, C. Clark, D. Sirmans, J. Dooley, J. Carter, and W. Bumgarner. July 1976. 47 p. (PB-263813/AS)

No. 79 Subsynoptic Scale Dynamics As Revealed By The Use of Filtered Surface Data. Charles A. Doswell III. December 1976. 40 p. (PB-265433/AS)

No. 80 The Union City, Oklahoma Tornado of 24 May 1973. Rodger A. Brown, Editor. December 1976. 235 p. (PB-269443/AS)

No. 81 Mesocyclone Evolution and Tornado Generation Within the Harrah, Oklahoma Storm. Edward A. Brandes. May 1977. 28 p. (PB-271675/AS)

No. 82 The Tornado: An Engineering-Oriented Perspective. Joseph E. Minor, James R. McDonald, and Kishor C. Mehta. December 1977. 196 p. (PB-281860/AS)

No. 83 Spring Program '76. R. Alberty, J. Weaver, D. Sirmans, J. Dooley, and B. Bumgarner. December 1977. 130 p. (PB-280745/AS)

No. 84 Spring Program '77. Peter S. Ray, John Weaver, and NSSL Staff. December 1977. 173 p. (PB-284953/AS)

No. 85 A Dual-Doppler Variational Objective Analysis as Applied to Studies of Convective Storms. Conrad L. Ziegler. November 1978. 116 p. (PB-293581/AS)

No. 86 Final Report on the Joint Doppler Operational Project (JDOP) 1976-78. Prepared by Staff of the National Severe Storms Laboratory, Environmental Research Laboratories; Weather Radar Branch, Air Force Geophysics Laboratory; Equipment Development Laboratory, National Weather Service; and Air Weather Service, United States Air Force. March 1979. 84 p. (PB80-107188/AS)

No. 87 An Analysis of the Clear Air Planetary Boundary Layer Wind Synthesized from NSSL's Dual Doppler-Radar Data. Myron I. Berger and R. J. Doviak. June 1979. 55 p. (PB-300865/AS)

No. 88 The Relationship of the 300-mb Jet Stream to Tornado Occurrence. Carolyn M. Kloth and Robert P. Davies-Jones. July 1980. 62 p. (PB81-118960)

No. 89 A Study of Hail Production in a Supercell Storm Using a Doppler Derived Wind Field and a Numerical Hail Growth Model. Stephan P. Nelson. December 1980. 90 p. (PB81-17822Q)

No. 90 Summary of AEC-ERDA-NRC Supported Research at NSSL 1973-1979. J. T. Lee, Editor. March 1981. 93 p. (PB81-220162)

No. 91 1980 Spring Program Summary. R. J. Doviak, Editor. April 1981. 128 p. (PB81-234940)

No. 92 Multiple Doppler Radar Analysis of Severe Thunderstorms: Designing a General Analysis System. R. A. Brown, C. R. Safford, S. P. Nelson, D. W. Burgess, W. C. Bumgarner, M. L. Weible, and L. C. Fortner. June 1981. 18 p. (PB82-114117)

No. 93 1981 Spring Program Summary. William L. Taylor, Editor. March 1982. 97 p. (PB82-244757)

No. 94 Multiple Doppler Radar Derived Vertical Velocities in Thunderstorms: Part I - Error Analysis and Solution Techniques, Part II - Maximizing Areal Extent of Vertical Velocities. Stephan P. Nelson and Rodger A. Brown. October 1982. 21 p. (PB83-152-553)

☆ U.S. GOVERNMENT PRINTING OFFICE: 1984—776-001/4108 REGION NO. 8